

Design of a Piezoelectric Tool for Active Control of Cutting Forces in Machining


by

Nikolay Tzonev

B.Eng., University of Victoria, 1997

A Thesis Submitted in Partial Fulfillment of the
Requirements for the Degree of
Master of Applied Science
in the
Department of Mechanical Engineering


We accept this thesis as conforming
to the required standard




Dr. Y. Stepanenko, Supervisor (Dept. of Mechanical Engineering)



Dr. S. Dost, Co-supervisor (Dept. of Mechanical Engineering)



Dr. H. King, Departmental Member (Dept. of Mechanical Engineering)



Dr. D. Shpak, Outside Member (Dept. of Electrical and Computer Engineering)



Dr. G. May, External Examiner (George A. May and Associates Ltd.)

© Nikolay Tzonev, 2002

University of Victoria

All rights reserved. This thesis may not be reproduced in whole or in part,
by photocopy or other means, without the permission of the author.

Supervisors: Dr. Yury Stepanenko and Dr. Sadik Dost

Abstract

The work presented in this thesis describes the design, implementation, and testing of a novel 1-DOF piezoelectric-actuated device that is intended to operate as a platform for future realization of various chatter suppression control strategies. The common practice of introducing viscoelastic treatments to dynamically unstable systems is not suitable for applications such as chatter suppression where the cause of the vibrations cannot be properly predicted and simulated. In these cases, active vibration cancellation and prevention technology can sense, isolate, and damp vibrations or noise.

The new device employs a piezoelectric translator acting upon a drum. The design allows for two modes of operation that are functionally separated by a preset internal preload. The first mode of operation is passive and, for as long as the system sensors register contact and the cutting forces remain steady, no active control is attempted. When the original preload is overcome by the presence of a large external cutting force, the device reacts in a way that counter-acts and stabilizes the external disturbance. The system was found suitable for dynamic control applications within a [0,700] Hz bandwidth. Dynamic tests of the device indicated satisfactory output force characteristics with rapid force degradation outside the upper bandwidth boundary. The assembly was tested with a ShopTask Shopmaster 2000 combination mill/lathe.


This work confirms the feasibility of using piezoelectric sensors and actuators for designing machine-chatter suppression devices that can operate within practical frequency bandwidths. The innovative approach of installing the piezoelectric actuator in series with the active element, rather than the traditional shunted configuration,

proved to be capable of delivering the desired dynamic characteristics necessary for implementing future chatter suppressing control strategies.


Examiners:




Dr. Y. Stepanenko, Supervisor (Depart. of Mechanical Engineering)




Dr. S. Dost, Co-supervisor (Depart. of Mechanical Engineering)



Dr. H. King, Departmental Member (Depart. of Mechanical Engineering)



Dr. D. Shpak, Outside Member (Depart. of Electrical and Computer Engineering)



Dr. G. May, External Examiner

Table of Contents

Abstract	ii
Table of Contents	iv
List of Tables	viii
List of Figures	ix
List of Symbols	xiii
Acknowledgements	xvi
Dedication	xvii
1 Introduction.....	1
1.1 Problem Statement.....	1
1.2 Thesis Outline.....	3
2 Piezoelectricity and Piezoceramics.....	5
2.0 History of Piezoelectric Ceramics.....	5
2.1 Piezoelectricity.....	7
2.1.1 Ferroelectric Ceramics.....	7
2.1.2 Poling.....	8
2.1.3 Hysteresis Effects.....	9
2.2 Piezoelectric Effects.....	11
2.2.1 The Direct Piezoelectric Effect.....	11
2.2.2 The Indirect Piezoelectric Effect.....	12
2.3 Fundamental Equations of Piezoelectricity.....	13
2.3.1 Balance Laws.....	13

2.3.2 Constitutive Equations	18
2.3.2.1 Piezoceramics as Elastic Dielectrics	19
2.3.2.2 Linear Equations	23
3 Applications of Piezoceramics as Actuators and Sensors	25
3.0 General Applications of Piezoceramics	25
3.1 Piezosensing Devices.....	27
3.1.1 Ceramic Configuration in Piezoelectric Sensors	29
3.1.2 Operation and Types of Piezotransducers.....	30
3.1.2.1 Charge Mode System.....	32
3.1.2.2 Low Impedance Voltage Mode (LIVM).....	36
3.1.2.3 LIVM Force Transducers.....	40
3.1.2.3.1 Sensor Discharge Time Constant.....	42
3.1.2.3.2 Frequency Response and Natural Frequency.....	44
3.2 Piezoactuators	46
3.2.1 Types of Piezoactuators	47
3.2.1.1 Stack Piezoactuators	48
3.2.1.2 Ring Piezoactuators	50
3.2.1.3 Bending Piezoactuators.....	51
3.2.1.4 Tube Piezoactuators	51
3.2.2 Parameters of Piezoelectric Actuators	52
3.2.2.1 Actuator Stroke	52
3.2.2.2 Force Generation.....	54
3.2.2.3 Stiffness.....	55

3.2.2.4 Resolution and Accuracy	56
3.2.3 Practical Considerations.....	59
3.2.3.1 Actuator Breakage	59
3.2.3.2 Lead Attachment.....	60
3.2.3.3 Mounting Guidelines	60
4 Design of a Platform for Experimental Study of	
Active Vibration Control in Machining.....	61
4.0 Introduction.....	61
4.1 Background.....	62
4.1.1 Active Control of Mechanical Vibrations in Machining	63
4.1.1.1 Boring Bar Application for Turning	67
4.1.1.2 Vibration Control for Active Bending of Structures.....	70
4.1.1.3 Generic Active Vibration Cancellation Mount	72
4.1.2 Vibration Phenomena in Machining	74
4.1.2.1 Mechanics of Metal Cutting.....	75
4.1.2.2 Fundamentals of Structural Vibrations in Machining.....	78
4.1.2.3 Chatter Vibrations in Cutting.....	79
4.2 Platform Design	83
4.2.1 Conceptual Proposal	84
4.2.2 Requirements identification.....	86
4.2.3 System design	87
4.2.4 System integration	89
4.2.4.1 Force Sensors	89

4.2.4.2 Piezoelectric Actuator.....	90
4.2.4.3 Enclosure and Support Components.....	91
4.2.4.4 Drum	93
4.2.4.4.1 FEA Model.....	94
4.2.4.4.2 Constraints	97
4.2.4.4.3 Loads.....	98
4.2.4.4.5 Results.....	100
4.2.4.5 Control Electronics	104
4.2.5 Testing.....	106
4.2.5.1 Tool Holder Dynamic Characteristics	107
4.2.5.2 Machine Testing.....	111
4.2.6 Improvements and Fine-tuning	114
5 Conclusions and Recommendations for Future Development.....	117
References.....	120
Appendix A Technical Drawings of the Chatter Suppression Device.....	123

List of Tables

Table 2.1: Symbols used in the balance equations.....	18
Table 2.2: Symbols used in the derivations	22
Table 2.3: Corrections for the linear constants	23
Table 3.1: Modern applications of piezoceramic materials	26
Table 4.1: Displacement results	100
Table 4.2: Contact line force results	101

List of Figures

Figure 2.1: Structure of BaTiO ₃ at temperatures above and below its Curie temperature	8
Figure 2.2: Poling of ceramics	9
Figure 2.3: Strain vs. applied electrical field hysteresis for PZT	10
Figure 2.4: Schematic illustration of the piezoelectric effects.....	12
Figure 3.1: Material configurations used in piezotransducer design	29
Figure 3.2: Piezoceramic transducer applications	30
Figure 3.3: Charge mode transducer system.....	33
Figure 3.4: Charge mode amplifier.....	33
Figure 3.5: LIVM transducer system.....	37
Figure 3.6: LIVM schematic diagram.....	37
Figure 3.7: LIVM force piezosensor.....	41
Figure 3.8: Simplified TC circuit schematics and Voltage vs. Time output diagram	42
Figure 3.9: Frequency response of a LIVM sensor	44
Figure 3.10: Piezoelectric stack	48
Figure 3.11: Stacked actuator	49
Figure 3.12: Stacked actuator with mechanical amplifier	50
Figure 3.13: Tube actuators	51
Figure 3.14: A and B stroke of piezoactuators	53
Figure 4.1: 1-DOF system with shunted piezoelectric actuator.....	64

Figure 4.2: Active vibration control conceptual diagram	65
Figure 4.3: Basic actuation approaches	66
Figure 4.4: Actively controlled boring bar system	68
Figure 4.5: Surface finish comparison of surfaces produced with and without the boring bar active control	69
Figure 4.6: Sample transfer function with effect of flexible body control	71
Figure 4.7: Generic active vibration cancellation mount modes of operation.....	72
Figure 4.8: Cutaway view of the active vibration cancellation mount	73
Figure 4.9: Deformation zones in orthogonal cutting.....	76
Figure 4.10: Cutting force diagram.....	77
Figure 4.11: Regenerative wave generation	80
Figure 4.12: Chatter dynamics block diagram.....	81
Figure 4.13: Piezoelectric device for control of chatter forces	83
Figure 4.14: Basic principle of operation of the new tool holder	85
Figure 4.15: Chatter suppression tool holder.....	86
Figure 4.16: Chatter suppression tool system design	88
Figure 4.17: Chatter suppression tool components.....	91
Figure 4.18: FEA model	95
Figure 4.19: Line representation with keypoints	95
Figure 4.20: Meshed FEA volume.....	96
Figure 4.21: Contact elements	97
Figure 4.22: Model constraints	98
Figure 4.23: Pressure loads.....	100

Figure 4.24: Half-drum reaction force distribution	103
Figure 4.25: Control electronics block diagram	104
Figure 4.26: Final tool assembly.....	107
Figure 4.27: Resonance frequency characteristics (750N preload)	108
Figure 4.28: Resonance frequency characteristics (1000N preload)	108
Figure 4.29: Tool-sensor dynamic response (750N preload)	109
Figure 4.30: Tool-sensor and actuator-sensor dynamic force response (750N preload).....	110
Figure 4.31: Force transmission ratio	111
Figure 4.32: ShopTask Shopmaster 2000	112
Figure 4.33: Tool installation.....	112
Figure 4.34: Experimental workpiece.....	113
Figure 4.35: Experimental tool	115
A1: Box Bottom.....	124
A2: Box Back	125
A3: Box Front.....	126
A4: Box Side.....	127
A5: Box Top	128
A6: Drum.....	129
A7: Drum Support - Back.....	130
A8: Drum Support - Bottom	131
A9: Drum Support - Spring	132

A10: Locator.....	133
A11: Riser.....	134
A12: Spring.....	135
A13: Spring Mount.....	136
A14: Tool Connector - Top.....	137
A15: Tool Connector - Bottom.....	138

List of Symbols

\mathfrak{J}	Current vector
η	Entropy density
ψ	Free energy
λ	Scalar, time invariant constants
μ	Scalar, time invariant constants
ρ	Mass density
θ	Temperature
\mathbf{v}	Velocity vector
V	Body volume
β_{mki}^e	Electro-optical Coefficients
$\beta_{mki}^e \mathbf{D}_k$	Dielectric Impermittivness
χ_{ij}	Symmetric second order terms
δ_{ij}	Symmetric second order terms
ϵ_{ijmk}	Electrostriction Coefficient
$\epsilon_{ijmk} \mathbf{D}_k$	Piezoelectric Constant
τ_{ij}	Thermoelastic Coefficient
$\epsilon_{klmi} \mathbf{e}_{kl}$	Dielectric Impermittivness
$\Delta \mathbf{L}_0$	Elongation of a stack actuator
θ_m	Pyroelectricity
ϵ^T	Permittivity at constant stress

b	Cutting depth
B	Magnetic induction
C	Total shunt capacitance
C_A	Amplifier input capacitance
c^D_{ijklmn}	Nonlinear Elastic Constants
c^D_{ijklmn}ε_{mn}	Elastic Constant
C_f	Feedback capacitor
C_k^E	Electromagnetic couples
ε_{klm}	Permutation symbol in k (-1,0,1)
c_s	Resistance stiffness
c_t	Actuator stiffness
d	Piezoelectric constant
D	Dielectric displacement
e_{ij}	Strain tensor
E	Electric field
F^E	Electro-Magnetic body force
F_f	Feed cutting force
F_{fc}	Feed shear force contribution
F_{fe}	Flank feed force contribution
F_t	Tangential cutting force
F_{tc}	Tangential shear force contribution
F_{te}	Flank tangential force contribution
f_l	Body force
G_l	Electro-Magnetic stress
h	Chip thickness in cutting

\mathbf{h}	Heat vector
\mathbf{H}	Magnetic field
\mathbf{h}_{ijklm}	Nonlinear Piezoelectric Constants
$\mathbf{h}_{ijklm}\mathbf{D}_m$	Elastic Constant
$\mathbf{h}_{ijklm}\mathbf{e}_{kl}$	Piezoelectric Constant
\mathbf{K}_f	Feed cutting proportionality coefficient
\mathbf{K}_{fe}	Edge force feed contribution
\mathbf{K}_{se}	Edge force tangential contribution
\mathbf{K}_t	Tangential cutting proportionality coefficient
\mathbf{M}	Magnetization (per volume)
\mathbf{P}	Polarization Factor
\wp	Poynting vector
\mathbf{q}	Heat vector
\mathbf{q}_e	Volume free charge density
\mathbf{q}_{in}	High-impedance charge
\mathbf{R}	Gate resistance
\mathfrak{N}	Scalar, time invariant constants
\mathbf{s}^E	Elastic compliance.
\mathbf{TC}	Sensor discharge time constant
\mathbf{T}_f	Force transmission ratio
\mathbf{t}_{kl}	Cauchy's stress tensor
\mathbf{t}_{kl}^{em}	Electro-Magnetic stress
\mathbf{V}	Instantaneous gate voltage
\mathbf{V}_0	Initial voltage
σ	Discontinuity surface

Acknowledgements

I would like to thank my supervisors, Dr. Yury Stepanenko and Dr. Sadik Dost for their help, guidance, and financial support throughout my program at the University of Victoria.

I also thank IRIS/PREARN for their financial contribution to the project.

I appreciate the help of Nolan Sackney with the system design and the FEA simulation.

The theoretical advice of Dr. Yusuf Altintas is greatly valued as well.

In addition, I thank Dilian Stoikov for his help during the final stages of the project and Dr. Shpak for always being able to think of the “right word” during the writing of this thesis.

Finally, I’d like to thank my dear wife Darla for being so proud of me.

To my beloved MOM and DAD

and

my sweet late puppy RITA

Chapter 1

Introduction

1.1 Problem Statement

Chatter vibration is a problem that occurs with most machining practices. The nature of chatter vibrations in machining is associated with random self-excitation mechanisms during the chip generation process of metal removing. The presence of large cutting forces during normal machining operations excites the natural vibration modes of the tool-workpiece set. Chatter vibrations result in a wavy surface finish, and in some severe cases, they can render the workpiece or the cutting tool useless. Chatter phenomena are complicated and, despite the increasing research activity in the field, have not been fully investigated to date. In general practice, it is operator experience and observation that most often prevents unexpected chatter vibrations.

The demands for high shape accuracy, surface roughness control, and reduction of sub-surface damage on manufactured parts are continuously increasing. Traditionally, the production machining process consists of a roughing step and a sequence of finishing steps, like grinding and polishing. Presently, there is an ever-increasing demand for new processes that combine high removal rates with high surface quality in a single step. Classical solutions, based on traditional stiff guide-way technology, cannot meet the requirements of these new machining processes because the machine cannot

effectively dissipate the energy transferred during the metal removing and the resultant vibrations make a smooth finish impossible.

Reducing unwanted vibrations has always been a challenge for engineers. Not too long ago, the only methods available for reducing undesired vibrations were redesigning the product or incorporating passive damping components. Active vibration control is a modern alternative solution that can yield increased performance with a significant efficiency in terms of time and money. Piezoelectric transducers have been widely used over the last decade for vibration control in university, corporate, and government research laboratories. Unfortunately, their introduction into commercial applications has lacked momentum. Utilization of piezotransducers and piezoactuators for suppression of chatter vibrations in machining is one particular application that has not fully benefited from the many possibilities piezo-technology can offer.

The development of industrial devices for active damping of chatter vibrations in machining is one of the ultimate goals of a collaborative IRIS/PRECARN project titled “Intelligent Systems for Precision Manufacturing”. Such an innovative undertaking involves various stages that need to be completed to reach the final objective. The successful implementation of chatter suppression control strategies first requires the development of a platform for experimental study of active vibration control in machining. The work presented in this thesis describes the design, implementation, and testing of a novel 1-DOF piezoelectric-actuated device that is intended to operate as a platform for future realization of various chatter suppression control strategies. This apparatus was designed at the IRIS Advanced Control and Instrumentation Laboratory of the Department of Mechanical Engineering of the University of Victoria.

1.2 Thesis Outline

This thesis is a detailed presentation of the design of a piezoelectric tool for active control of cutting forces in machining and includes relevant background work. The work is organized in five chapters.

Chapter 1 is an introduction to the problem and outlines the structure of the thesis.

Chapter 2 gives a brief review of historical developments associated with piezoelectricity, and presents the piezoelectricity phenomenon and related concepts like ferroelectricity, poling, and hysteresis. The purpose of chapter 2 is to provide a brief review of the theory behind the piezoelectric effects. An in-depth discussion of the subject is out of the scope of this thesis. In addition, chapter 2 also presents the derivation of the fundamental equations of piezoelectricity that provide the basis for practical engineering applications. The commonly used equations of piezoelectricity are simple linear equations that have been derived from complex macroscopic electro-mechanical relationships.

Chapter 3 introduces practical applications of the piezoelectric effects for production of sensors and actuators. Chapter 3 is an overview of the latest developments in piezotechnology. The first part of the chapter presents the two types of piezosensor designs that are used in practice: Charge Mode Systems and Low Impedance Voltage Mode (LIVM) Systems. The second part of the chapter is a detailed analysis of piezotransducer devices. Due to their particular relevance to this thesis, piezoelectric stack actuators and their characteristics are covered in details.

The main contribution of the thesis and a discussion of the design process that resulted in the development of the apparatus for studying and actively reducing mechanical vibrations in machining are presented in chapter 4. The chapter briefly covers the basics of machine cutting and the nature of chatter vibrations in machining. Since the design is targeting active control applications, chapter 4 contains a review of the major active control concepts. In addition, several relevant background designs are discussed in detail.

The main topic of chapter 4 is the design approach that was implemented in the research process. This work involved several distinct steps: conceptual proposal, requirements identification, system design, system integration, testing, improvements and fine-tuning. All steps are covered in details.

Finally, chapter 5 summarizes the results of the research and recommends areas for future improvements.

Appendix A contains the detailed drawings of the device.

Chapter 2

Piezoelectricity and Piezoceramics

2.0 History of Piezoelectric Ceramics

The word “piezo” is derived from the Greek word for pressure “piesi”. It was originally used to describe the ability of some solid materials to produce an electric field proportional to an applied mechanical deformation; known as “direct piezoelectric effect”. Pierre and Jacques Curie discovered this phenomenon in 1880. In their early research, they discovered piezoelectric properties in the crystals of sodium chlorate, boracite, tourmaline, quartz, and Rochelle salt. Soon it was realized that these materials must also show the “converse effect”, a geometric deformation proportional to an applied voltage. Despite its promising characteristics, the piezoelectric effect remained a scientific curiosity until the First World War when its particular military applications were further investigated. In France, Langevin used quartz crystals to emit, and later receive, high-frequency sound waves for the detection of enemy submarines. This research resulted in the development of oscillators, stabilizers, and filters [13].

Piezoelectricity remained a branch of crystal physics until the discovery of the first piezoelectric ceramics during the Second World War. Barium titanate (BaTiO_3) was the first ceramic material to show piezoelectric properties comparable to those of Rochelle salt. Moreover, it was easy to produce, it could withstand higher temperature, and it was not water-soluble. The record shows that BaTiO_3 was first clearly

recognized by R. B. Gray of the Erie Resistor Company, as described in his patent application filed in 1946. However, S. Roberts who worked independently of Gray made the first publication on piezoelectric barium titanate. The work of both Gray and Roberts demonstrated piezoelectric interaction between an electric signal applied to a BaTiO_3 specimen and stress or strain not only parallel to the electric field but even perpendicular to it. The first commercial BaTiO_3 piezoelectric devices were phonograph pickups marketed by Sonotone Corporation in 1947 [24].

Rapid development of barium titanate followed in conjunction with the development of new piezoelectric materials. Compositional modifications were found that improved its temperature stability and gain output. In the early 1950s, lead niobate led to the discovery of several lead based piezoelectric ceramics. The most significant of them was the lead zirconate titanate solid solution or PZT: $(\text{Pb}(\text{Zr},\text{Ti})\text{O}_3)$. PZT exhibited piezoelectric constants twice as large as the constants exhibited by BaTiO_3 . The modification of PZT by doping with metallic impurities has resulted in the discovery of a group of ceramics that have varying characteristics and currently are the primary materials used for piezoelectric applications [5].

PZT based ceramics can handle large-magnitude electric fields (up to 1 kV/mm), thereby generating large stresses (up to 9.8 MPa). When the applied electric field is small, the induced strain is nearly proportional to the electric field. However, as the electric field becomes larger (greater than 0.1 kV/mm), the strain curve significantly deviates from this linear trend and large hysteresis is exhibited. This limits the use of PZTs for actuator applications [5].

The recent study of electrostriction (a second order phenomenon of electromechanical coupling that used to be considered a negligible effect in early studies) has a potential to lead to the discovery of piezoelectric ceramics that exhibit significant strains without the presence of significant hysteresis effects. Lead magnesium niobate (PMN) based ceramics are amongst the electrostrictive materials that have captured the interest of the researchers [15].

Another group of materials with a promising future is the composites of piezoelectric ceramics and polymers. With composite piezoelectric ceramics, superior piezoelectric performance has been achieved while maintaining the mechanical flexibility of the polymers [5].

2.1 Piezoelectricity

The piezoelectricity phenomenon cannot be explained without the definition of concepts like ferroelectricity, poling, and hysteresis. However, the purpose of this section is to provide only a brief review of the theory behind the piezoelectric effects and in-depth discussion is out of the scope of this thesis.

2.1.1 Ferroelectric Ceramics

Some ceramic ionic crystalline materials have unit cells that do not have a center of symmetry and as a result their unit cells can sustain a small permanent dipole. Such materials are known as ferroelectrics. An industrially important ceramic material in this class is barium titanate, BaTiO_3 . Above 120°C , BaTiO_3 has the cubic symmetry of the

perovskite crystal structure shown in Figure 2.1a. Below 120°C , the central Ti^{4+} ion and the surrounding O^{2-} ions of the BaTiO_3 unit cell shift slightly to create a small permanent electric dipole moment (see Figure 2.1b).

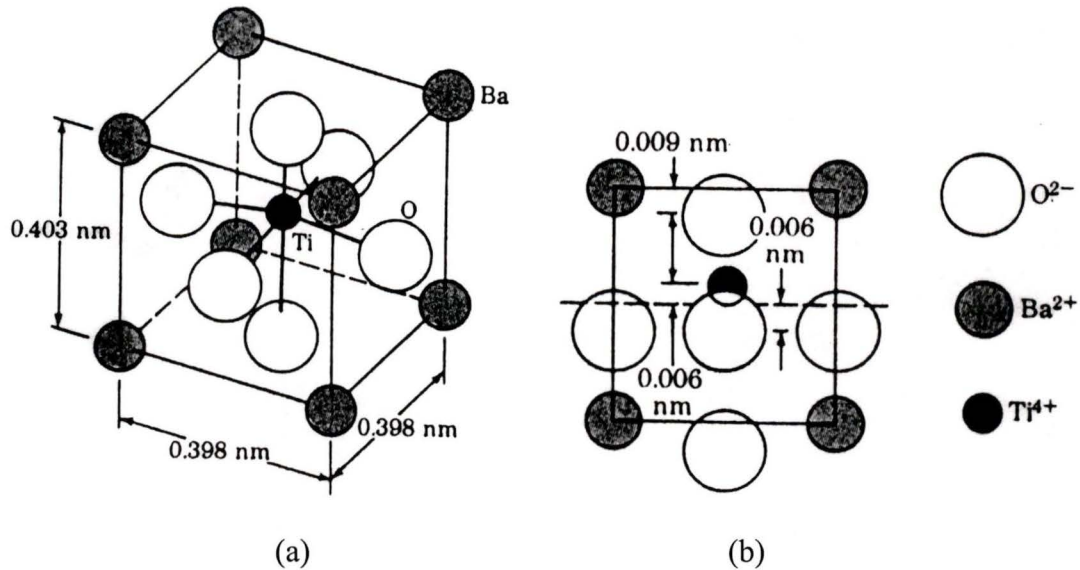


Figure 2.1: Structure of BaTiO_3 at temperatures above and below its Curie temperature [23]

This shifting of the ion positions, at the critical temperature of 120°C , changes the crystal structure of BaTiO_3 from cubic to tetragonal and eliminates the centre of symmetry. The temperature at which this phenomenon occurs is specific for each material and is known as the Curie temperature [23].

2.1.2 Poling

On a larger scale, solid BaTiO_3 ceramic material has a domain structure within which the small electric dipoles of the unit cells line up in one direction. As the resultant dipole moment of a unit volume of this material is the sum of the small dipole moments

of the unit cells, if the moments of the domains are randomly oriented, there is no net charge at the surface of the crystal (as shown in Figure 2.2a). If polycrystalline BaTiO_3 is slowly cooled through its Curie temperature in the presence of a strong electric field, the dipoles of all the domains tend to line up in the direction of the electric field to produce a strong dipole moment per unit volume of the material as illustrated on Figure 2.2b. This process is known as *poling*. The poling process switches the direction of the dipoles in the ferroelectric materials and converts them into piezoelectrics [9].

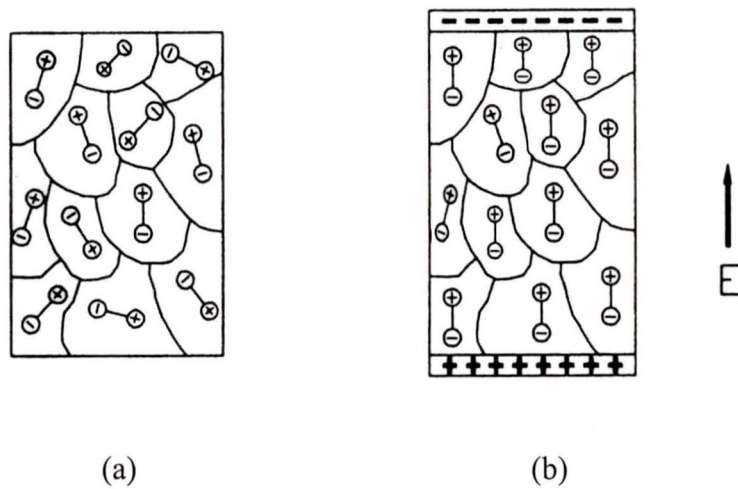


Figure 2.2: Poling of ceramics a) Random polarization b) Application of an electric field [9]

The switching of dipole direction during poling does not involve any physical rotation of the domains. What happens is that the Ti cations are displaced in the opposite direction relative to the oxygen anions. This occurs when they gain enough energy from the poling electric field to overcome the crystal's internal energy.

2.1.3 Hysteresis Effects

The actual relations between strain and electrical field in the piezoelectric materials are very complicated. Usually, strain changes in the crystal structure result in domain re-

orientations, leading to hysteresis during an electric field cycle. Hysteresis effects are considered the major source of errors in the operation of piezoactuators.

The magnitude of the hysteresis can be assessed by measuring the maximum difference in the displacement of a test specimen for a series of applied voltages. The hysteresis measurement results for a lead zirconate titanate (PZT) sample, which is the most common industrial piezoelectric material, are plotted in Figure 2.3. This material exhibits an almost linear relationship between strain and applied field below 100 V/mm, but for larger fields there is a non-negligible hysteresis during the rise and fall of the field. This is a great problem for actuator applications where the average electric field is about 1 kV/mm [15].

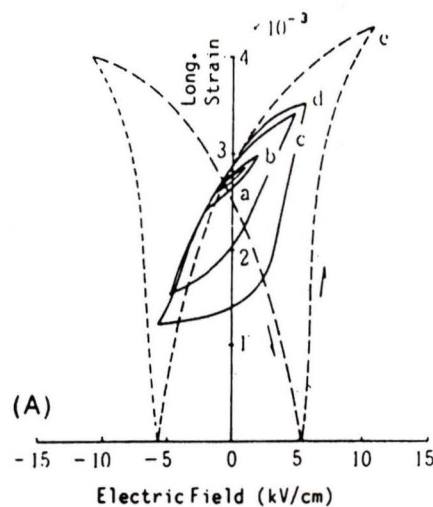


Figure 2.3: Strain vs. applied electrical field hysteresis for PZT [15]

The recent research in electrostrictive materials has resulted in the development of a group of new materials that exhibit almost no strain/electric field hysteresis. The best examples of non-hysteresis electrostrictive materials are the lead magnesium niobate (PMN) based ceramics. A 1-cm long PMN specimen can elongate by 10 μ m without

hysteresis. The preparation of ultrafine PZT ceramics has promising future as another way of avoiding the unwanted hysteresis effects. Significant reduction in hysteresis has been observed in PZT ceramics with grain sizes $<1.8\mu\text{m}$ [14].

Piezoceramics are classified in two major groups depending on the characteristic Curie temperature for the material. In general, piezoceramics with Curie temperature above $300\text{ }^\circ\text{C}$ are classified as *hard* piezoceramic materials. Hard piezoceramics have smaller piezoelectric constants that produce smaller expansions. However, they exhibit better linearity and less severe hysteresis effects that are within 2% tracking error. *Soft* piezoceramics, on the other hand, have lower Curie temperatures that can even be as low as room temperature in some cases. They produce far greater expansions in comparison with the hard piezoceramics but the tradeoff is a significant deviation from linearity and hysteresis effects as high as 20% [15].

2.2 Piezoelectric Effects

Piezoelectric effects can be used to convert mechanical energy to electrical *energy* (*direct effect*) or electrical energy to mechanical deformation (*indirect* or *converse effect*). Many commercial devices utilize these effects primarily in the form of sensors and actuators.

2.2.1 The Direct Piezoelectric Effect

As a result of the poling effect, the transformed ferroelectric material will have an excess of positive charge at one end and negative charge at the other end in the direction

of polarization (see Figure 2.4a). As a uniform compressive stress is applied on the opposite surfaces of a test specimen, the overall length of the sample will be reduced (see Figure 2.4b). This reduces the distance between the unit dipoles and thus the overall dipole moment per unit volume of the material is reduced proportionally.

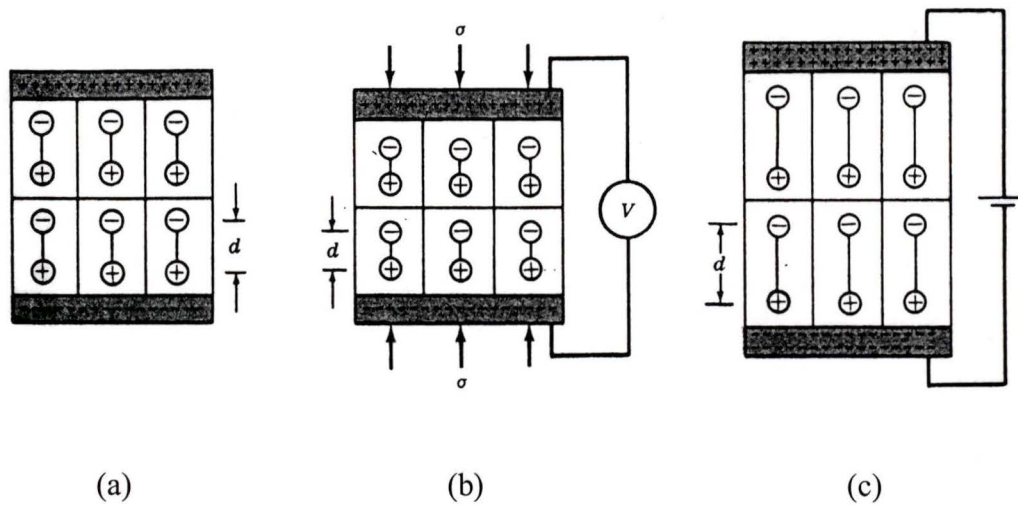


Figure 2.4: Schematic illustration of the piezoelectric effects [23]

The change in the dipole moment of the material changes the charge density at the ends of the sample and thus changes the voltage differential between the opposite faces of the sample. The phenomenon is known as the direct piezoelectric effect and is particularly useful for producing sensors [23].

2.2.2 The Indirect Piezoelectric Effect

In reverse, if an electric field is applied across the end of the sample, the charge density at each face of the sample will be altered (Figure 2.4c). This change in the charge density will cause the sample to change its dimensions in the direction of the applied field. In the case of Figure 2.4c, the sample is elongated due to the increased amount of

positive charge attracting the negative poles of the dipoles (this works in reverse order at the other end of the sample). This phenomenon is known as the indirect piezoelectric effect [23]. Although in practice the overall displacement of the opposite faces of the crystal is in the range of micrometers, a significant amount of force can be generated in the process. The indirect piezoelectric effect is particularly useful in the design of solid-state actuators.

2.3 Fundamental Equations of Piezoelectricity

The majority of piezoelectric equations used in many practical engineering applications are simple linear equations that have been derived from complex macroscopic electro-mechanical relationships. The macroscopic electro-mechanical theory is based on two sets of equations. The first set of equations can be applied regardless of the material and has been derived from the basic laws of continuum physics, simultaneously applied with Maxwell's equations. The second set of equations, known as the *Constitutive Equations*, is applied strictly for the material under investigation. The utilization of these principles leads to expressions for the change in the electric field and the change in mechanical stress during the direct and during the indirect piezoelectric effects.

2.3.1 Balance Laws

The balance laws applicable to any material consist of Maxwell's equations and the thermo-mechanical balance laws. These principles are axioms that have never been proven wrong. The thermo-mechanical balance equations consist of four equalities that are the conservation of mass, the balance of momentum, the balance of moment of

momentum, and the conservation of energy. The fifth principle is the change in entropy. These laws, including the electric contributions, are written below for a body with volume V (excluding a discontinuity surface σ and its velocity v) [16].

Conservation of Mass

$$\frac{\partial \rho}{\partial t} + (\rho v_k)_{,k} = 0 \quad \text{in } V - \sigma \quad [1]$$

$$\| \rho (v_k - v_k) \| n_k = 0 \quad \text{on } \sigma \quad [2]$$

Balance of Linear Momentum

$$\rho \dot{v}_l = t_{kl,k} + \rho f_l + F_l^E \quad \text{in } V - \sigma \quad [3]$$

$$\| \rho v_l (v_k - v_k) - (t_{kl} + t_{kl}^{em} + v_k G_l) \| n_k = 0 \quad \text{on } \sigma \quad [4]$$

Balance of Moment of Momentum

$$\varepsilon_{klm} t_{lm} + C_k^E = 0 \quad \text{in } V - \sigma \quad [3a]$$

$$\| \rho v_l (v_k - v_k) - (t_{kl} + t_{kl}^{em} + v_k G_l) \| n_k = 0 \quad \text{on } \sigma \quad [4]$$

Conservation of Energy

$$\rho(\dot{\Psi} + \dot{\theta}\eta + \theta\dot{\eta}) + t_{kl}v_{l,k} - q_{k,k} - \rho h + P_k \dot{E}_k + M_k \dot{B}_k - \mathfrak{T}_k E_k = 0 \quad \text{in } \mathcal{V} - \sigma \quad [5]$$

$$\left\| \left\{ \rho(\Psi + \theta\eta) + E_l P_l + \frac{1}{2} \rho v^2 + \frac{1}{2} (E^2 + B^2) \right\} (v_k - v_k) - (t_{kl} + t_{kl}^E + v_k G_l) v_l - q_k + \wp_k \right\| n_k = 0 \quad \text{on } \sigma \quad [6]$$

Entropy Inequality

$$\rho \dot{\eta} - \left(\frac{q_k}{\theta} \right)_{,k} - \frac{\rho h}{\theta} \geq 0 \quad \text{in } \mathcal{V} - \sigma \quad [7]$$

$$\left\| \rho h (v_k - v_k) - \frac{1}{\theta} q_k \right\| n_k \geq 0 \quad \text{on } \sigma \quad [8]$$

Discarding the surface polarization and the surface currents, the local electromagnetic balance laws over the same body can be written as:

Gauss' Law

$$\nabla \cdot \mathbf{D} - q_e = 0 \quad \text{in } \mathcal{V} - \sigma \quad [9]$$

$$\mathbf{n} \cdot \mathbf{D} = w_e \quad \text{on } \sigma \quad [10]$$

Faraday's Law

$$\nabla \times \mathbf{E} + \frac{1}{c} \frac{\partial \mathbf{B}}{\partial t} = 0 \quad \text{in } \mathcal{V} - \sigma \quad [11]$$

$$\mathbf{n} \times \left\| \mathbf{E} + \frac{1}{c} \mathbf{v} \times \mathbf{B} \right\| = 0 \quad \text{on } \sigma \quad [12]$$

Conservation of Magnetic Flux

$$\nabla \cdot \mathbf{B} = 0 \quad \text{in } \mathcal{V} - \sigma \quad [13]$$

$$\| \mathbf{B} \| \cdot \mathbf{n} = 0 \quad \text{on } \sigma \quad [14]$$

Ampere's Law

$$\nabla \times \mathbf{H} - \frac{1}{c} \frac{\partial \mathbf{D}}{\partial t} = \frac{1}{c} \mathbf{J} \quad \text{in } \mathcal{V} - \sigma \quad [15]$$

$$\mathbf{n} \times \left\| \mathbf{H} - \frac{1}{c} \mathbf{v} \times \mathbf{D} \right\| = 0 \quad \text{on } \sigma \quad [16]$$

Conservation of Electric Charge

$$\frac{\partial q_e}{\partial t} + \nabla \cdot \mathbf{J} = 0 \quad \text{in } \mathcal{V} - \sigma \quad [17]$$

$$\mathbf{n} \cdot \|\mathbf{J} - q_e \mathbf{v}\| = 0 \quad \text{on } \sigma \quad [18]$$

For an infinite, rigid, isotropic, dielectric, and paramagnetic body, the following linear relations can be applied [16]:

$$\mathbf{D} = \lambda \mathbf{E} \quad [19]$$

$$\mathbf{B} = \mu \mathbf{H} \quad [20]$$

$$\mathbf{P} = \aleph \mathbf{E} \quad [21]$$

Where λ , μ , and \aleph are scalar, time invariant constants. This approximation, however, is only valid for relatively weak electro-magnetic fields. For strong electro-magnetic fields, the proportionality terms take the nonlinear form [16]:

$$\aleph_{ij} = \delta_{ij} + \chi_{ij} \quad [22]$$

Where δ_{ij} and χ_{ij} are symmetric second order terms. In addition, the terms used in equations 1 through 21 are presented in Table 2.1.

Table 2.1: Symbols used in the balance equations

Symbol	Description
t_{kl}	Cauchy's stress tensor
t_{kl}^{em}	Electro-Magnetic stress tensor
G_l	Electro-Magnetic moment
\mathfrak{J}	Current vector
\wp	Poynting vector. Flux of Electro-Magnetic energy
F^E	Electro-Magnetic body force
D	Dielectric displacement. The density of the electric flux/area
E	Electric field
θ	Temperature
η	Entropy density
q_e	Volume free charge density
P	Polarization Factor
C_k^E	Electromagnetic couples
ϵ_{klm}	Permutation symbol in k(-1,0,1)
B	Magnetic induction
M	Magnetization (per volume)
h	Heat vector
H	Magnetic field
e_{ij}	Strain tensor
ψ	Free energy

2.3.2 Constitutive Equations

The second set of equations necessary to fully describe a complex media comes from the constitutive equations. These equations characterize the nature of the material media. They express the response of the media to external stimuli. Consequently, they

have different forms depending on the nature and constitution of the body. For example, elastic bodies, viscous fluids, electromagnetic fluids, memory-dependent electromagnetic elastic solids, and ferromagnetic materials all have different constitutive equations. These equations, applied simultaneously with the balance laws, exclusively define the media [10].

The general approach in defining the constitutive equations is dividing the variables into dependent and independent. The dependent variables are considered to be functions of the independent variables. Fundamentally, the independent variables are the temperature θ , the strain tensor e_{ij} , the electric field E_{ij} , the temperature gradient $\nabla\theta$, and the magnetic induction vector B . They are external to the media and are defined at all points X of the body, at all past times [16].

2.3.2.1 Piezoceramics as Elastic Dielectrics

In general, piezoceramics are rarely good magnetic materials. Therefore, we can assume that they are non-magnetizable dielectrics. On the other hand, we can assume that they are elastic, isotropic, and that they can undergo polarization effects. Thus, at all places and all times [16]:

$$q_f = 0 \quad ; \quad \mathfrak{I} = 0 \quad ; \quad M(x,t) = 0 \quad ; \quad \psi = \Sigma / \rho_0(e_{ij}, \theta, D_i, e_{ij}) \quad [24]$$

Eliminating the $\rho h / \theta$ term between Equations 5 and 7, we obtain:

$$-\rho(\dot{\Psi} + \dot{\theta}\eta) + t_{kl}v_{l,k} + \frac{1}{\theta}q_k\theta_{,k} - P_k\dot{E}_k \geq 0 \quad [25]$$

Substituting $D\psi/Dt$ from Equation 24 into Equation 25 and utilizing Equations 19 through 21, we get the following inequality:

$$\left(t_{ij} - \rho_0 \frac{\partial \psi}{\partial e_{ij}}\right)\dot{e}_{ij} + \left(E_i - \rho_0 \frac{\partial \psi}{\partial D_i}\right)\dot{D}_i + \rho_0 \left(-\eta - \frac{\partial \psi}{\partial \theta}\right)\dot{\theta} - \rho_0 \frac{\partial \psi}{\partial \theta_{,i}}\dot{\theta}_{,i} + \frac{1}{\theta}q_i\theta_{,i} \geq 0 \quad [26]$$

The entropy inequality is linear in $\dot{e}_{ij}, \dot{D}_i, \dot{\theta}, \dot{\theta}_{,i}$, and the free energy term is independent of these quantities. Therefore, in order for the inequality to be satisfied at all times, the coefficients of these terms must vanish. Such a restriction results in:

$$t_{ij} = \rho_0 \frac{\partial \psi}{\partial e_{ij}} \quad [27]$$

$$E_i = \rho_0 \frac{\partial \psi}{\partial D_i} \quad [28]$$

$$\eta = \frac{\partial \psi}{\partial \theta} \quad [29]$$

$$\frac{\partial \psi}{\partial \theta_{,i}} = 0 \quad [30]$$

Equations 27 through 30 imply that $t_{ij}=t(e_{ij},\theta,D_i)$, and $E_i=E(e_{ij},\theta,D_i)$. Expanding the free energy term (Σ) into a Taylor series about a reference state denoted by index 0, and assuming a uniform temperature distribution and no initial strain, we obtain [9]:

$$\begin{aligned}
\Sigma = & \Sigma_0 + \left(\frac{\partial \Sigma}{\partial e_{ij}} \right)_0 e_{ij} + \left(\frac{\partial \Sigma}{\partial D_i} \right)_0 D_i + \left(\frac{\partial \Sigma}{\partial \theta} \right)_0 (\theta - \theta_0) + \frac{1}{2} \left(\frac{\partial^2 \Sigma}{\partial e_{ij} \partial e_{kl}} \right)_0 e_{ij} e_{kl} + \frac{1}{2} \left(\frac{\partial^2 \Sigma}{\partial D_m \partial D_k} \right)_0 D_k D_m + \frac{1}{2} \left(\frac{\partial^2 \Sigma}{\partial \theta \theta} \right)_0 (\theta - \theta_0)^2 \\
& + \frac{1}{2} \left(\frac{\partial^2 \Sigma}{\partial e_{ij} \partial D_m} \right)_0 e_{ij} D_m + \frac{1}{2} \left(\frac{\partial^2 \Sigma}{\partial D_m \partial \theta} \right)_0 D_m (\theta - \theta_0) + \frac{1}{2} \left(\frac{\partial^2 \Sigma}{\partial e_{ij} \partial \theta} \right)_0 e_{ij} (\theta - \theta_0)
\end{aligned} \tag{31}$$

The subscript 0 is used to denote that these functions are evaluated at the reference state ($D_i=0$, $e_{ij}=0$, $\theta_i=0$). Substituting Equation 31 into equations 27 and 28 results in the equations for t_{ij} and for E_m .

$$\begin{aligned}
t_{ij} = & \frac{\partial \Sigma}{\partial e_{ij}} = \left(\frac{\partial \Sigma}{\partial e_{ij}} \right)_0 + \left(\frac{\partial^2 \Sigma}{\partial e_{ij} \partial e_{kl}} \right)_0 e_{kl} + \frac{1}{2} \left(\frac{\partial^2 \Sigma}{\partial e_{ij} \partial D_m} \right)_0 D_m + \frac{1}{2} \left(\frac{\partial^2 \Sigma}{\partial e_{ij} \partial \theta} \right)_0 (\theta - \theta_0) + \frac{1}{2} \left(\frac{\partial^3 \Sigma}{\partial e_{ij} \partial e_{kl} \partial e_{mn}} \right)_0 e_{kl} e_{mn} \\
& + \frac{1}{3} \left(\frac{\partial^3 \Sigma}{\partial e_{ij} \partial e_{kl} \partial D_m} \right)_0 e_{kl} D_m + \frac{1}{6} \left(\frac{\partial^3 \Sigma}{\partial e_{ij} \partial D_m \partial D_k} \right)_0 D_m D_k + \frac{1}{6} \left(\frac{\partial^3 \Sigma}{\partial e_{ij} \partial D_m \partial \theta} \right)_0 D_m (\theta - \theta_0) \\
& + \frac{1}{3} \left(\frac{\partial^3 \Sigma}{\partial e_{ij} \partial e_{kl} \partial \theta} \right)_0 e_{kl} (\theta - \theta_0) + \frac{1}{6} \left(\frac{\partial^3 \Sigma}{\partial e_{ij} \partial \theta \theta} \right)_0 (\theta - \theta_0)^2
\end{aligned} \tag{32}$$

$$\begin{aligned}
E_m = & \frac{\partial \Sigma}{\partial D_m} = \left(\frac{\partial \Sigma}{\partial D_m} \right)_0 + \left(\frac{\partial^2 \Sigma}{\partial D_m \partial D_k} \right)_0 D_k + \frac{1}{2} \left(\frac{\partial^2 \Sigma}{\partial e_{ij} \partial D_m} \right)_0 e_{ij} + \frac{1}{2} \left(\frac{\partial^2 \Sigma}{\partial D_m \partial \theta} \right)_0 (\theta - \theta_0) + \frac{1}{2} \left(\frac{\partial^3 \Sigma}{\partial D_m \partial D_k \partial D_n} \right)_0 D_n D_k \\
& + \frac{1}{6} \left(\frac{\partial^3 \Sigma}{\partial e_{ij} \partial e_{kl} \partial D_m} \right)_0 e_{ij} e_{kl} + \frac{1}{3} \left(\frac{\partial^3 \Sigma}{\partial e_{ij} \partial D_m \partial D_k} \right)_0 e_{ij} D_k + \frac{1}{6} \left(\frac{\partial^3 \Sigma}{\partial e_{ij} \partial D_m \partial \theta} \right)_0 e_{ij} (\theta - \theta_0) \\
& + \frac{1}{3} \left(\frac{\partial^3 \Sigma}{\partial \theta \theta D_m \partial D_k} \right)_0 D_k (\theta - \theta_0) + \frac{1}{6} \left(\frac{\partial^3 \Sigma}{\partial D_m \partial \theta \theta} \right)_0 (\theta - \theta_0)^2
\end{aligned} \tag{33}$$

Table 2.2: Symbols used in the derivations [9]

Tensor	Description	Formula
\mathbf{h}_{ijklm}	Nonlinear Piezoelectric Constants	$-\frac{1}{6} \left(\frac{\partial^3 \Sigma}{\partial e_{ij} \partial e_{kl} \partial D_m} \right)_0$
\mathbf{c}^D_{ijklmn}	Nonlinear Elastic Constants	$\frac{1}{4} \left(\frac{\partial^3 \Sigma}{\partial e_{ij} \partial e_{kl} \partial e_{mn}} \right)_0$
θ_m	Pyroelectricity	$-\frac{1}{2} \left(\frac{\partial^2 \Sigma}{\partial D_m \partial \theta} \right)_0$
β^E_{mki}	Electro-optical Coefficients	$\frac{1}{4} \left(\frac{\partial^3 \Sigma}{\partial D_m \partial D_k \partial D_i} \right)_0$
ϵ_{ijmk}	Electrostriction Coefficient	$-\frac{1}{12} \left(\frac{\partial^3 \Sigma}{\partial e_{ij} \partial D_m \partial D_k} \right)_0$
τ_{ij}	Thermoelastic Coefficient	$-\frac{1}{2} \left(\frac{\partial^2 \Sigma}{\partial e_{ij} \partial \theta} \right)_0$

The coefficients presented in Table 2.2 represent various physical effects observed in piezoceramics. Their appearance depends on the nature of the ceramic and the operating conditions. Some of the most important ones, other than piezoelectricity, are pyroelectricity and electrostriction [9].

Pyroelectricity is a state of electric polarity produced on crystal structures due to temperature changes. The prerequisite for strong pyroelectric effects is the presence of unique polar axis in the crystal structure. However, this topic is beyond the scope of this thesis [9].

Electrostriction is a second order phenomenon of electromechanical coupling that is directly proportional to the square of an applied electrical field and thus does not depend on the sign direction of the field [12].

2.3.2.2 Linear Equations

Using the terms presented in Table 2.2 and correcting for the linear relations expressing the dependence of the stress and the electric field on the strain and the electric displacement, we can write [9]:

$$t_{ij} = (c^D_{ijkl} + c^D_{ijklmn}e_{mn} - h_{ijklm}D_m)e_{kl} - (h_{ijm} + h_{ijklm}e_{kl} - \varepsilon_{ijmk}D_k)D_m - \tau_{ij}(\theta - \theta_0) \quad [34]$$

$$E_m = (-h_{mlk} - h_{ijklm}e_{ij} - \varepsilon_{klmi}D_i)e_{kl} + (\beta^e_{mi} - \varepsilon_{klmi}e_{kl} + \beta^e_{mki}D_k)D_i - \theta_m(\theta - \theta_0) \quad [35]$$

The second and third terms in each bracket in Equations 34 and 35 are nonlinear terms.

The corrections for the linear constants are presented in Table 2.3:

Table 2.3: Corrections for the linear constants [9]

Correction	Description	Cause
$h_{ijklm}e_{kl}$	Piezoelectric Constant	Strain
$c^D_{ijklmn}e_{mn}$	Elastic Constant	Crystal Deformation
$\varepsilon_{klmi}e_{kl}$	Dielectric Impermittiviness	Mechanical Strain
$\beta^e_{mki}D_k$	Dielectric Impermittivities	Elastic Displacement
$h_{ijklm}D_m$	Elastic Constant	Electric Displacement
$\varepsilon_{ijmk}D_k$	Piezoelectric Constant	Electric Displacement

In order to have a physical insight into the indirect and direct piezoelectric effects, we consider one-dimensional linear constitutive equations by simply neglecting the nonlinear material coefficients that have insignificant effect in the direction of the

electric field. The linear relation used in practice for the indirect effect is presented in Equation 36 and Equation 37 gives the linear dependence for the direct effect, rearranged for the electric displacement. Both equations neglect the temperature dependence [9].

$$\mathbf{e} = \mathbf{s}^E \mathbf{t} + \mathbf{d} \mathbf{E} \quad [36]$$

$$\mathbf{D} = \boldsymbol{\varepsilon}^E \mathbf{E} + \mathbf{d} \mathbf{t} \quad [37]$$

In these equations, \mathbf{d} is the *piezoelectric constant*, and \mathbf{s}^E is the *elastic compliance*. The elastic compliance denotes the interaction between the stress and strain under constant electric field. On the other hand, the component $\boldsymbol{\varepsilon}^T$ is the *permittivity* at constant stress. Of all constants, the one-dimensional piezoelectric constant is the most critical parameter in the design of piezoelectric actuators. However, the other constants may be significant in different applications. For example, the second order electrostriction phenomenon was neglected for many years [23].

Chapter 3

Applications of Piezoceramics as Actuators and Sensors

3.0 General Applications of Piezoceramics

As discussed in the previous chapters, piezoelectric materials can be used to convert mechanical energy into electrical energy and vice versa. These conversion phenomena are known as the “direct piezoelectric effect” and the “inverse piezoelectric effect”. Many areas of every-day life benefit in one form or another from the utilization of piezoceramic materials. Table 3.1 is only a brief summary of the many modern applications of piezoceramics [18].

Although the utilizations of piezoceramic materials presented in Table 3.1 are quite promising for present and future applications, one of the fastest growing research areas in this field, and by far the most intriguing, is in the design of “smart structures”. Conceptually, the term “smart structures” focuses on adding “smarts” to inanimate objects that allow them to interact with their environment. When a smart structure detects an undesired external condition, it alters its dynamic properties including stiffness, damping, and shape. One of the primary applications of “smart structures” is to control unwanted vibrations. Vibrations cause problems ranging from small annoyances to catastrophic failures and human casualties in a wide variety of products. The common practice of introducing viscoelastic treatments (springs and dampers) to

dynamically unstable systems is not suitable for a variety of applications where the cause of the vibrations cannot be properly predicted and simulated. In these cases, Active Vibration Control Module (AVCM) technology can sense, isolate, and damp vibrations or noise.

Table 3.1: Modern applications of piezoceramic materials

Industry	Application
Optics, Photonics, and Measuring Technology	<ul style="list-style-type: none"> • Image stabilization • Scanning microscopy • Auto-focus systems • Interferometry • Fiber-optic alignment & switching • Fast mirror scanners • Adaptive and active optics • Laser turning • Mirror positioning • Holography • Stimulation of vibrations
Disk Drive Manufacturing	<ul style="list-style-type: none"> • MR head testing • Pole tip recession • Disk spin stands • Vibration cancellation
Microelectronics	<ul style="list-style-type: none"> • Nano-metrology • Wafer and mask positioning • Critical dimension measurement • Microlithography • Inspection systems • Vibration cancellation
Precision Mechanics and Mechanical Engineering	<ul style="list-style-type: none"> • Vibration cancellation • Structural deformation • Out-of-roundness grinding, drilling, turning

	<ul style="list-style-type: none"> • Tool adjustment • Wear correction • Micro pumps • Linear drives • Piezo hammers • Knife edge control in extrusion tools • Micro engraving • Shock wave generation
Life Science, Medicine, Biology	<ul style="list-style-type: none"> • Patch-clamp drives • Gene technology • Micro manipulation • Cell penetration • Micro dispensing devices • Audiophysiological stimulation • Shock wave generation

Controlling such properties involves combining sensors (to sense particular properties), electronics (to process the sensor information), and actuators (to modify the structure and improve performance). The purpose of this chapter is the facilitation of in-depth understanding of modern piezoelectric sensors and actuators that are essential for designing Active Vibration Control Modules (AVCM).

3.1 Piezosensing Devices

All piezosensing devices operate on the principle of the “direct piezoelectric effect”. Generally, inside the sensor, piezoelectric ceramics are stressed in a controlled fashion by the specific phenomena to be measured. This stress displaces a quantity of electrical charge from the piezoelectric material. The displacement occurs in direct proportion to the input and creates measurable electrical output signals [8].

Piezoceramics have very high stiffness values that are comparable to that of many metals. Some reach orders of 15×10^6 psi (104×10^9 N/m²) that allow for high output generation with very little strain. In fact, piezoelectric sensing elements have virtually no deflection. Piezosensors are very rugged and feature such an excellent linearity over a wide amplitude range that they are often referred to as solid-state devices. Because of the high stiffness of piezoelectric materials, it is possible to produce sensors with very high resonant frequencies that are suitable for measurements of rapidly changing dynamic parameters. Piezoelectric sensors (transducers) measure dynamic phenomena such as force, pressure, and acceleration (including shock and vibration). When coupled with properly designed signal conditioners, piezoelectric sensors typically have a dynamic amplitude range (ie: maximum measurement range to noise ratio) on the order of 120 dB. Such bandwidth allows a single accelerometer to be used for acceleration measurements from as low as 0.0001g to as high as 100g [17].

Unfortunately, one of the greatest disadvantages of piezoelectric sensors is the fact that they can only measure dynamic events. Piezosensors are not able to measure a continuous static event, as would be the case with inertial guidance, barometric pressure, weight measurements, and slowly changing forces. A static event will cause an initial output signal that will slowly decay with time. The signal “fade-away” is proportional to a time constant that is based on the capacitance and the resistance of the device. Such performance is similar to the output through a high-pass filter and ultimately determines the low frequency cut-off or measuring limit of the device. Although limiting the applications of piezotransducers for measuring static events, the “high-pass” filter response can be compensated through the utilization of precision data

acquisition systems. However, this is only possible for transducers with relatively large time constants.

3.1.1 Ceramic Configuration in Piezoelectric Sensors

Many different sizes, shapes, and orientations of piezoelectric materials can be used to manufacture piezoelectric transducers. Different element configurations have demonstrated both advantages and disadvantages in various implementations. Figure 3.1 is a visualization of the three main material configurations that are currently most widely used, namely: compression, flexural, and shear.

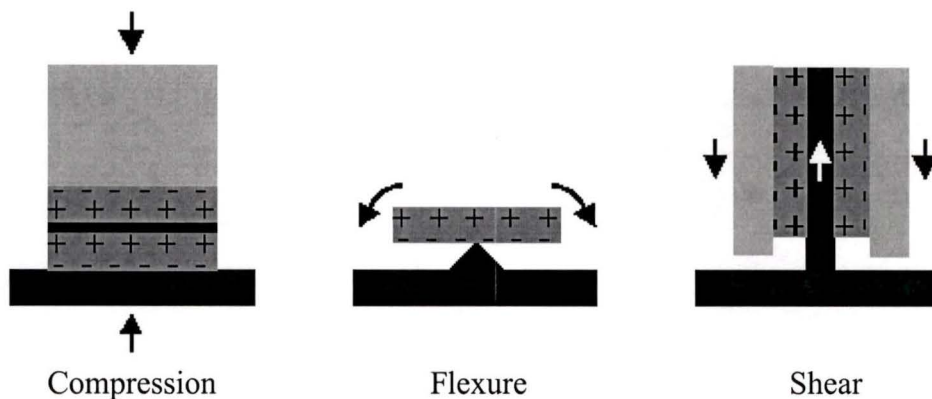


Figure 3.1: Material configurations used in piezotransducer design [17]

The compression design features high rigidity that makes it useful for implementation in high frequency pressure and force sensors. Its main disadvantage is that it is somewhat sensitive to thermal transients. The flexural design is the simplest of all three and therefore the cheapest and easiest to manufacture. Unfortunately, these advantages are offset by its narrow frequency range and low shock survivability. The shear configuration is typically used in accelerometers as it offers a well balanced blend of wide frequency range, low off-axis sensitivity, low sensitivity to base strain and low

sensitivity to thermal inputs. At the same time, the shear configuration results in fairly expensive transducers [17].

3.1.2 Operation and Types of Piezotransducers

Piezoceramic technology continues to evolve and is currently very accessible to small and intermediate size companies that are capable of frequently introducing novel piezoceramic products to the market. Although many innovative piezotransducer solutions are constantly being offered, the three main applications of piezotransducers remain: force measurements, pressure measurements, and acceleration measurements. A representation of a typical force, pressure and acceleration sensor is shown in Figure 3.2. The main principle of operation is identical in all three cases; the black electrode in the middle accumulates the charge before an external electronic circuit conditions it.

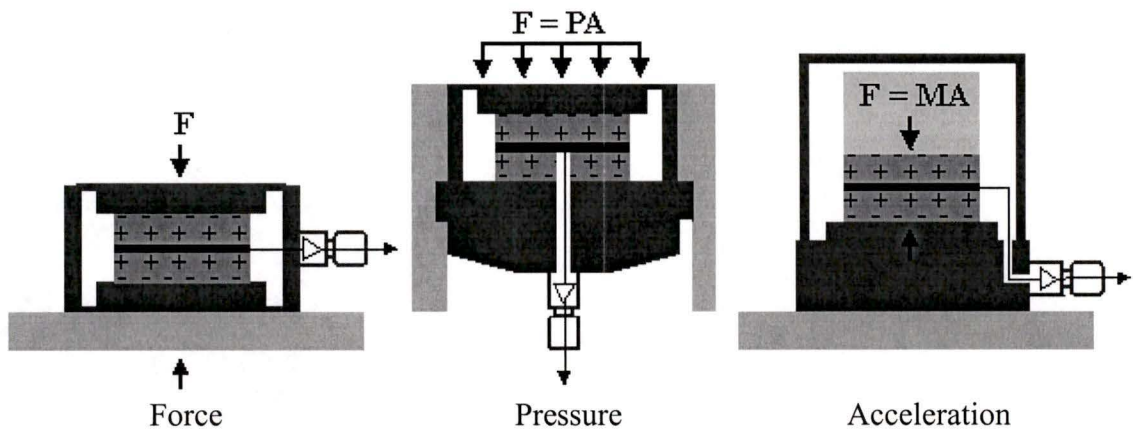


Figure 3.2: Piezoceramic transducer applications [17]

Pressure and force sensors are nearly identical and rely on an external force to strain the crystals. Figure 3.2 demonstrates the major difference between the two types of transducers; the pressure sensors utilize a diaphragm to collect pressure, which is simply force applied over an area. In contrast, accelerometers incorporate a mass element that converts the resulting force on the crystal into acceleration according to

Newton's Second Law of Motion: $\mathbf{F}=\mathbf{ma}$. In accelerometers, which in fact measure motion, the invariant seismic mass element is forced by the coupled piezocrystal to follow the motion of the base and the structure to which it is attached.

Because of the principle similarity of operation of the three types of sensors, sensors designed to measure one specific parameter are also somewhat sensitive to other inputs. To accurately measure the intended parameter, it is crucial to minimizing the transducer's sensitivity to unwanted events. Sophisticated pressure sensors often utilize a compensation element to reduce its sensitivity to acceleration. Other sensors employ thermal compensating amplifiers to reduce the sensors overall thermal coefficient. Finally, some accelerometers utilize alternative shear-structured sensing elements to reduce the affects of thermal transients, transverse motion, and base strain [8].

After the sensing element produces a presumably desirable output, this signal must be conditioned prior to being analyzed by an oscilloscope, analyzer, data acquisition, DSP, or other readout device. The measurement/conditioning electronics has to couple to the outside world the information contained within the small amount of electrical charge generated by the crystals. This process must occur without any charge dissipations or changes. The quantity of charge generated by the piezo element is usually very small and is measured in units of picocoulombs, (pC) which is 1×10^{-12} Coulombs.

Throughout the evolutionary process of piezoelectric sensor development, two types of systems have emerged as the main choices for dynamic output conditioning: charge signal utilization known as the *Charge Mode System* and voltage signal utilization known as the *Low Impedance Voltage Mode (LIVM) System*. The transducers used with

Charge Mode Systems are generally manufactured with crystalline quartz and in some cases with PZT piezoceramic inserts. The transducers used with Low Impedance Voltage Mode (LIVM) Systems are built with crystalline quartz.

The following sections introduce in detail the two types of electronic conditioning systems used in piezosensing and the specifics of the piezotransducers that are used with them. The LIVM force sensors are particularly relevant to the topic of this thesis and are introduced in great detail in a separate subsection.

3.1.2.1 Charge Mode System

When a piezocrystal is stressed, a charge output in response to the disturbance is generated. Since the charge is in the order of picocoloumbs, a special type of amplifier, called a charge amplifier, is used to measure the high impedance electrostatic charge signal from the crystals. The charge amplifier has the ability to convert the charge signal to a low impedance voltage mode signal without modifying it. This high-impedance output must be routed through a short low-noise cable to an impedance-converting amplifier or a source follower. The primary function of the charge or voltage amplifier is to convert the high-impedance output to a usable low-impedance voltage signal for recording or displaying purposes. Due to the high impedance of the signal, insulation resistance must be maintained in the cables and connections at all times. Figure 3.3 is a symbolic and graphic representation of a typical charge mode measurement system. The input stage of the charge amplifier utilizes a capacitive feedback circuit to eliminate the effect of the applied input charge signal [8].

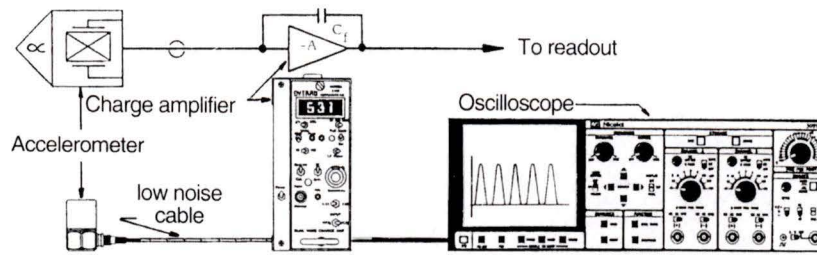


Figure 3.3: Charge mode transducer system [8]

The feedback signal is then a measure of the input charge. This amplifier presents essentially infinite input impedance to the sensor and thus measures its output without changing the charge of the crystal. In Figure 3.3, the gain (transfer function) of the basic charge amplifier is dependent only on the value of the feedback capacitor C_f and is independent of the input capacitance. The following discussion is a brief introduction to the basic operation of a Charge Mode Amplifier.

A charge amplifier is a high gain, high-input impedance, inverting voltage amplifier with capacitive feedback. The amplifier is usually an operational amplifier (op-amp) with near infinite voltage gain as shown on Figure 3.4. Usually, following stages add voltage gain and attenuation, filtering, and other functions to further process and refine the data before coupling it to the readout instrument [8].

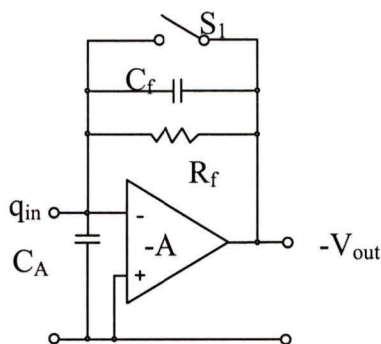


Figure 3.4: Charge mode amplifier (also known as analog integrator)

When the high-impedance charge q_{in} from the sensor is applied to the summing junction of the op-amp, it is distributed to the input capacitor of the amplifier C_A and the feedback capacitor C_f according to the following relationship:

$$q_{in} = q_A + q_f \quad [38]$$

Using the electrostatic equation $q = Cv$ and substituting in Equation 38 we derive:

$$q_{in} = v_A C_A + v_f C_f \quad [39]$$

By substituting V_A and V_f using the fundamental relationships for an ideal op-amp we obtain:

$$V_{out} = \frac{-q_{in} A}{C_A + C_f (A + 1)} \quad [40]$$

Where the open-loop gain A is assumed to be infinite for an ideal op-amp, Equation 40 becomes:

$$V_{out} = \frac{-q_{in}}{C_f} \quad [41]$$

Equation 41 is the transfer function of an ideal Charge Mode Transducer System. Clearly, the output is a function of the feedback capacitor C_f only and the input capacitance C_A has no effect on the system. This means that cable capacitance, for example, has no effect on the sensitivity of the overall system.

Charge Mode Piezosensing setups are widely used for industrial applications because they offer a variety of advantages to the alternative systems. Some of these advantages can be summarized with [17]:

- Piezotransducers used with Charge Mode Systems do not have electronic components contained within the sensor housing and therefore, the high temperature operation limit of the device is set by the Curie temperature of the piezoelectric material.
- Laboratory-type Charge Amplifiers currently available offer a wide range of signal conditioning choices such as filtering, ranging, standardization, integrating for velocity and displacement, and peak hold.
- Charge amplifier gain is independent of the input cable capacitance.
- In certain cases, Charge Systems can be designed with very long time constants and can be used as “Electrostatic”- type. This type of systems can be used for “quasi-static” measurements of events lasting up to several minutes duration.

Despite the many advantages of utilizing a Charge Mode System in an industrial setting, several application limitations must be mentioned:

- The output from the Charge Mode transducer is a high impedance charge. Therefore, to preserve the signal quality, all elements of the system, including the amplifier, must also have a very high insulation resistance. Environmental contaminants on the connector such as moisture, dirt, oil, or grease reduce insulation and result in signal drift and inconsistent results.
- Use of special low-noise cable is required with charge mode pressure sensors. When flexed, standard two-wire or coaxial cables generate charge between the conductors.

3.1.2.2 Low Impedance Voltage Mode (LIVM)

The Low Impedance Voltage Mode systems have recently become the prime choice for many practical applications. Fundamentally, the most significant difference between Charge Mode piezotransducers and LIVM piezotransducers is that LIVM sensors utilize the voltage generated by the crystal rather than the electrical charge. LIVM devices incorporate a built-in MOSFET (Metal Oxide Silicon Field Effect Transistor) high-impedance microelectronic amplifier to convert the charge output into a low-impedance voltage signal. Typically, the on-board sensor circuitry is powered by a constant-current source. This allows signals to be carried over long ribbon cables without significant data degradation. A block diagram of a common LIVM system is shown on Figure 3.5 [8].

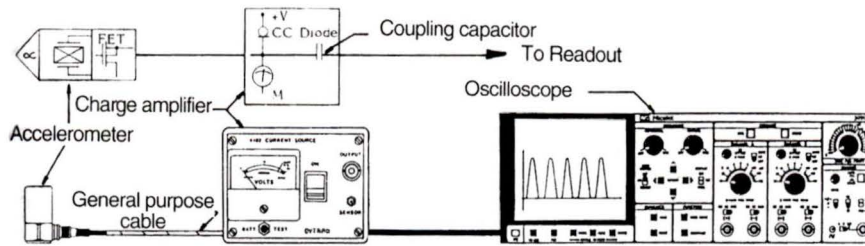


Figure 3.5: LIVM transducer system [8]

The voltage generated by the LIVM transducers is related to the charge signal according to Equation 41 with the exception that C is the crystal capacitance rather than the op-amp input capacitance. The sensors used with the LIVM setups are almost exclusively made with crystalline quartz inserts rather than PZT ceramic inserts. Compared to PZT, crystalline quartz has very low charge sensitivity. This disadvantage, however, is compensated by crystalline quartz's very low internal capacitance that, according to Equation 41, results in a high-sensitivity voltage signal.

In addition, Figure 3.6 shows a schematics example of two-wire system that uses a common conductor for power/signal and a second conductor for the ground. The transducer's built-in circuits are miniature charge amplifiers that typically draw power from standard 18 - 30 VDC, 2 mA constant current supply.

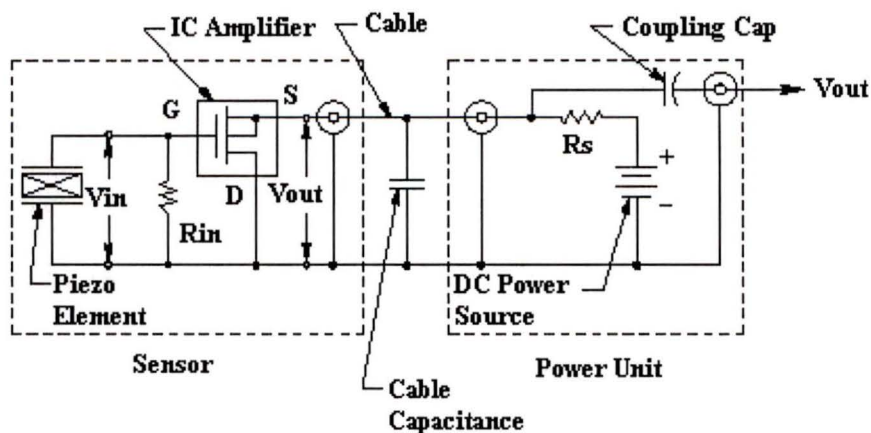


Figure 3.6: LIVM schematic diagram [8]

The system amplifier is a unity-gain source follower circuit. The output signal V_{out} is passed through a coupling capacitor that eliminates the DC bias voltage from the DC power source so that the conditioned signal may be connected to an external readout instrument.

The sensitivity of LIVM transducers is fixed at the time of manufacture by varying the total capacitance across the quartz crystal element. To obtain the highest possible sensitivity, no additional capacitance should be added to the native capacitance of the crystal. This, however, limits the distance of signal propagation and in many cases extra shunt capacitance is added so extra range can be achieved. The high impedance input to the MOSFET is completely enclosed by the metal housing. Therefore, due to this shielding effect, the LIVM sensor is not susceptible to external electrostatic interference and other disturbances. Setting the capacitance inside the casing determines the sensitivity of the LIVM transducer and it cannot be subsequently varied by external means. The fixed sensitivity of the transducer is calibrated at the plant and, to avoid errors, a data sheet must always accompany the instrument [7].

Similar to the Charge Mode systems, LIVM piezotransducer systems have both technical advantages and disadvantages. The main advantages that the LIVM setup offers can be summarized with [8]:

- The low output impedance of the transducer makes the sensitivity of the LIVM system independent of the cable length. Large distances can separate the transducer and the amplifier electronics. With proper design, LIVM amplifiers can drive cables up to thousands of feet long.

- The system sensitivity does not change when the cable type is replaced.
- Inexpensive twin-lead ribbon cables can be used to connect the sensor to the power unit.
- The sensitivity and the discharge time constant of the transducer are fixed at the time of manufacture and cannot be influenced afterwards. This makes LIVM sensors ideal for dedicated applications, as they do not require frequent calibration and servicing.
- The sealed durable construction of the sensors makes LIVM systems suitable for harsh industrial applications.
- LIVM power units are relatively simple and cheaper than the Charge Amplifiers.
- The tiny MOSFET amplifier chips built into the LIVM sensors are able to withstand shocks of over 100,000 g's. This characteristic of the LIVM transducers is particularly valued by the aerospace industry and by the military industry.

The main disadvantages of using LIVM measurement instrumentation are primarily due to the presence of the MOSFET electronic unit inside the transducer:

- Silicon-based Integrated Circuits have limited temperature range of operation and that restricts the LIVM transducer implementation to relatively low temperature applications. The temperature range of operation for a typical commercial LIVM transducer is $-60/+250$ °F ($-50/120$ °C).
- The MOSFET IC is susceptible to burnouts due to improper operation or unexpected voltage spikes in the circuit. A damaged transducer cannot be repaired in the field and must be sent to the manufacturing plant for refurbishing and calibration.
- LIVM transducers have short time constants and are rarely capable of measuring events longer than 1 Hz.

3.1.2.3 LIVM Force Transducers

The mechanical properties of piezotransducer materials, such as strength and stiffness, are almost comparable to these of steel. Therefore, they can easily be integrated into the parts of a mechanical structure. In addition, these sensors have very high natural frequencies and extremely short response characteristics that are ideal for measuring very quick transient forces, such as those generated by metal-to-metal impacts and high frequency vibrations [8].

Low Impedance Voltage Mode (LIVM) force sensors contain thin piezoelectric crystals that generate analog voltage signals in response to applied dynamic forces. A built in MOSFET IC chip amplifier converts the high impedance signal generated by the

crystals to a low impedance signal suitable for remote amplification and conditioning.

A cross section of a common piezo force sensor is shown on Figure 3.7.

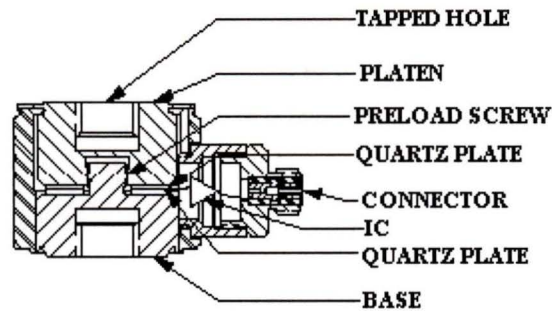


Figure 3.7: LIVM force piezosensor [8]

In Figure 3.7, a preload screw presses two crystalline quartz discs against the platen. Preloading is necessary for tight assembly fit and achieving best linearity and tension range of the device. The platen and the base are tapped so threaded inserts like mounting bolts, impact caps, or machine elements can be easily attached to the sensor. The platen can independently flex by being connected to the housing through a steel web. Environmental isolation is achieved by welding the platen and the base to the outer housing of the transducer. The miniature IC is contained inside a radially mounted connector housing.

When an external compressive force stresses the crystal, a positive voltage is generated. This voltage is accumulated on the electrode and transferred to the input of the MOSFET unity-gain amplifier contained within the transducer housing. The amplifier has a low output impedance so that the signal can be further conditioned and manipulated. The same sensor can operate both in tension and compression mode. The tension mode utilizes the preload that exists in the system. When the sensor is put

under tension, some of the preload is released causing the crystals to generate a negative output signal. However, the maximum tensile loading is limited by the ultimate strength of the internal preload screw thread and is usually much less than the compression range [18].

3.1.2.3.1 Sensor Discharge Time Constant

In general, applied force to the quartz crystals of a piezoelectric force sensor generates only an electrostatic charge. Unfortunately, despite the relatively large electrical insulation resistance of the device, the electrostatic charge will eventually dissipate to zero through the lowest path of resistance. The time that the sensor output voltage takes to lose 63% of its initial level is defined as the *Sensor Discharge Time Constant-TC*. The immediate implications of the TC are related to the low-frequency operation of the transducer and the quasi-static response capabilities of the transducer. If we consider a simplified LIVM piezo force transducer system as shown on Figure 3.8a, then the response of the system to a step function will be an exponential decay (See Figure 3.8 b) [17].

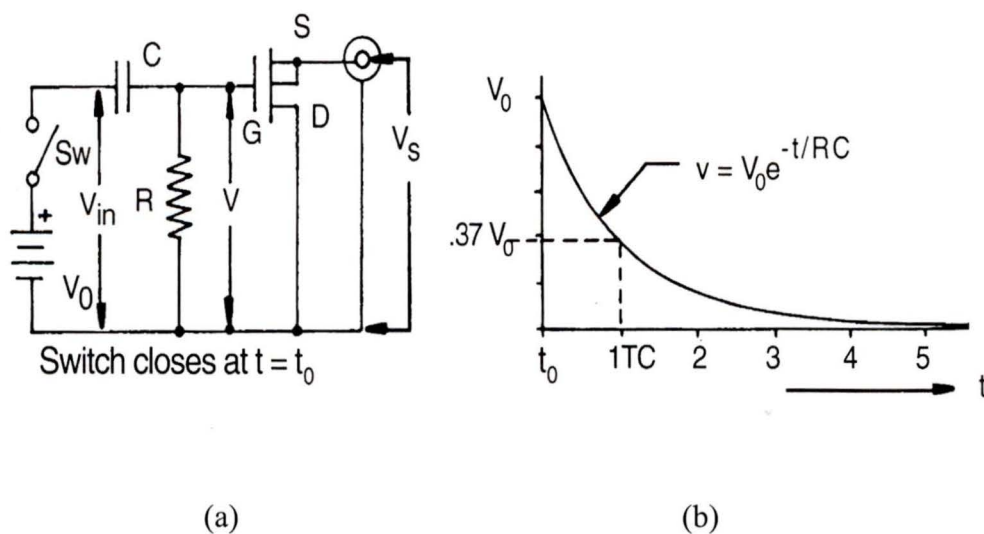


Figure 3.8: Simplified TC circuit schematics and Voltage vs. Time output diagram [8]

After the output voltage of the system reaches an initial level of V_0 , in time the voltage will go back to zero according to the following equation:

$$V = V_0 e^{-\frac{t}{RC}} \quad [42]$$

Where:

V is the instantaneous gate voltage

V_0 is the initial voltage created by the step function

R is the gate resistance

C is the total shunt capacitance

The capacitance C consists of the natural capacitance of the crystal insert, the input capacitance of the amplifier, the calibration shunt capacitance added during manufacturing, and other miscellaneous capacitance. In Equation 42, the product RC controls the time discharge of the system and the value of the product is equal to the time constant for the instrument - TC . When $t=RC$, the formula is reduced to:

$$V = V_0 e^{-1} = 0.37V_0 \quad [43]$$

As the time t in Equation 42 approaches $5xTC$, the output voltage will reach almost zero. Finally, the voltage response on Figure 3.8b is almost linear during the time duration before $0.1xTC$. The voltage drops only about 1% during that interval. Errors in the vicinity of 1% are acceptable even for some of the most precise industrial instruments. Therefore, it is a widespread practice to refer to the value of $0.1xTC$ as the quasi-static response time of a LIVM piezotransducer. In practice, the most commonly used LIVM force piezosensors have TC in the range of 1000 sec. Thus, the quasi-static

response of these sensors is 10 seconds. The sensor-specific quasi-static time response is essential during the transducer calibration procedures [17].

3.1.2.3.2 Frequency Response and Natural Frequency

The IC circuit schematic in Figure 3.8a is a first-order high-pass filter. To demonstrate the effect of TC on the system's response, a Bode plot of the frequency response of the circuit is shown on Figure 3.9. The response reaches 0dB attenuation at relatively low frequencies and becomes essentially flat beyond 20Hz.

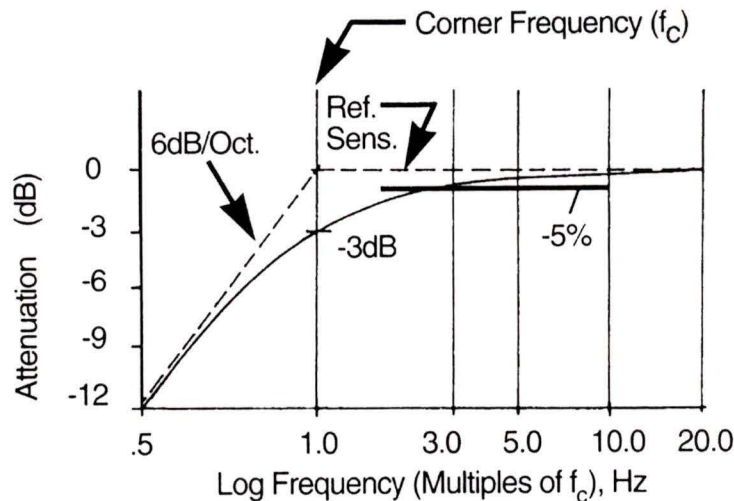


Figure 3.9: Frequency response of a LIVM sensor [16]

The initial slope of the graph is 6dB/octave (20dB/decade) that is characteristic for a first-order high-pass filter. A very significant point on the graph is the corner frequency that occurs at $f=f_c$. At that point, the instrument will be within 30% of its sensitivity. The corner frequency f_c is related to TC according to:

$$f_c = 0.16/TC$$

[44]

The constant TC is sensor specific and is always included in the calibration certificate of a LIVM sensor.

The natural frequency of a piezotransducer is proportional to the stiffness of the device and can be calculated according to:

$$f_n = \frac{1}{2\pi} \sqrt{\frac{k}{M}} \quad [45]$$

Where:

k is the sensor's stiffness

M is an external mass load

An important observation from Equation 45 is the fact that large external mass will lower the natural frequency of a piezotransducer. Even if the “unloaded” natural frequency of the sensor is high enough, heavy mass can result in unexpected, and in some cases destructive, resonance effects to the sensor body. In those cases, Equation 45 should be used to obtain a close approximation of the reduced natural frequency of the transducer [14].

3.2 Piezoactuators

In extreme-precision positioning applications, such as scanning tunneling microscopy, diamond turning machines, separation of cell cultures, etc., it is often required that actuators have nanometer resolution of displacement, high stiffness, and fast response. In practice, these requirements are met by the use of piezoceramic actuators.

Piezoelectric actuators employ the indirect piezoelectric effect to accurately convert an applied electric field into displacement. Even under high stress, some piezoactuators can produce a displacement of $10\mu\text{m}$ with an accuracy of $0.01\mu\text{m}$ in less than $10\mu\text{s}$. In addition to the high precision of displacement and the ultra-fast response speed, piezoactuators can produce large static and dynamic forces. These valuable performance characteristics make piezoelectric actuators the solution for a variety of problems that arise in the design of precision equipment.

The majority of present applications of piezoceramic actuators utilize their micro-positioning capabilities. However, dynamic applications such as vibration suppression and waveform excitation generation are becoming increasingly popular. Manipulator applications, and in particular, dynamic interactive manipulation, require control actuators that can provide both accurate position-tracking performance and robustly-stable force control. These applications utilize the force generation capabilities of the piezoelectric actuators.

The modern piezoelectric actuators are primarily manufactured with Lead-Zirconium-Titanate (PZT) ceramic active elements. Although new ceramic materials have recently

been introduced as replacements of PZT, for the short and midterm future, the broad industrial applications of solid-state piezoactuators will depend on PZT or a derivative from PZT. Presently, the solid-state industrial actuators are classified in four main categories that are: stack actuators, ring actuators, bending actuators (also known as bimorphs), and piezoelectric tubes. The following sections will introduce: the four major types of actuators, the control electronics used with the solid-state actuators, and actuator-specific technical parameters. Due to their particular relevance to this thesis, stack actuators will be covered in greater detail.

3.2.1 Types of Piezoactuators

Two main types of piezoactuators are available based on the field intensity necessary to produce full expansion: low voltage (multilayer) devices requiring about 100 volts for full motion and high voltage devices requiring about 1000 volts for full extension. Greatly improved piezoceramics capable of greater motion replace the natural material used by the Curies, in both types of devices. Lead zirconate titanate (PZT) based ceramic materials are most often used today. Actuators made of this ceramic material are often referred to as PZT actuators. In general, piezoceramics are manufactured to expand in a single direction that either coincides with the direction of the external electric field, or is perpendicular to the direction of the external electric field. However, in the case of bimorphs and piezoelectric tubes, the expansion is perpendicular to the direction of the electric field. The designers of piezoactuators utilize these inherent characteristics of the piezoceramics to produce devices with a variety of geometric configurations.

3.2.1.1 Stack Piezoactuators

The stack piezoactuators are the most common solid-state actuators used in industry today. The typical piezoactuator is constructed of stacked cylindrical piezoceramic discs and has a total length of L_0 and diameter of D . Figure 3.10 is an illustration of an ordinary stack piezoactuator. High voltage piezo actuators are constructed from 0.5 to 1.0 mm thick layers of ceramic material while low voltage piezoactuators are monolithic (diffusion bonded) multilayer designs constructed from 20 to 100 μm layers [17].

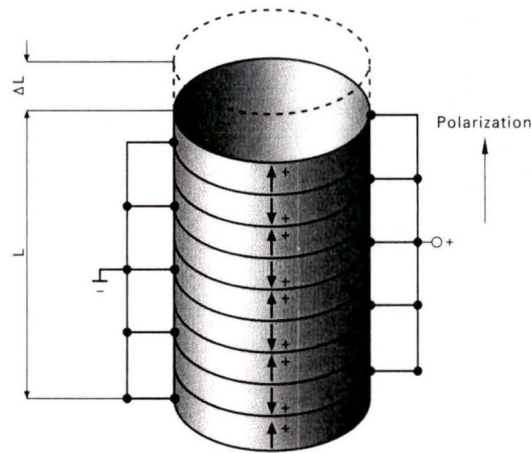


Figure 3.10: Piezoelectric stack [18]

As introduced in Chapter 2, the maximum electrical field PZT ceramics can withstand is on the order of 1 to 2 kV/mm. In order to keep the operating voltage within these limits and still be capable of practical expansions, PZT actuators consist of thin layers of piezoelectric ceramic material electrically connected in parallel (See Figure 3.10). The net positive displacement is the sum of the strain of the individual layers. Since all layers are connected to the same reference voltage, only a twisted pair of wires is necessary to deliver the control signal to the stack. The ceramic stack actuator length is

limited by stiffness and manufacturing considerations. The typical aspect ratio between length and diameter is 12:1 [18].

The ceramic stack is encapsulated within a metal case that protects it from external influences. If pulling action is desired, the case may contain a preloaded spring. For high-precision translations, the stack actuator will include an integrated high-resolution strain gage position sensor. Figure 3.11 illustrates a typical arrangement of a stack.

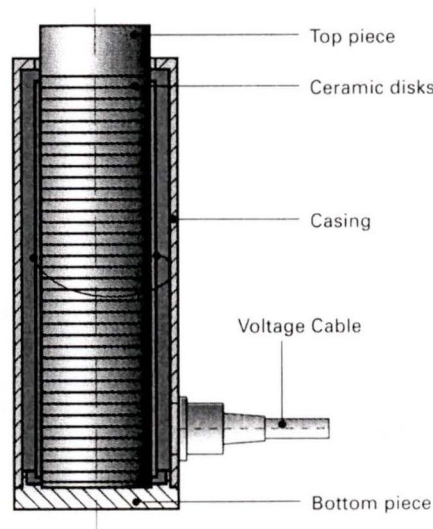


Figure 3.11: Stacked actuator [18]

In some applications, space restrictions do not allow for very long stacks. In these cases, it is possible to use mechanical lever amplifiers to decrease the length of the ceramic stack. The basic idea of a piezoactuator with mechanical amplifier is shown on Figure 3.12. Unfortunately, the increase in travel gained with a mechanical amplifier reduces the actuator's stiffness and maximum operating frequency [18].

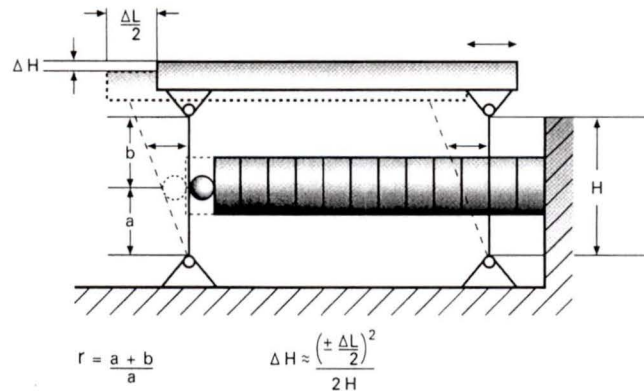


Figure 3.12: Stacked actuator with mechanical amplifier [18]

To maintain the sub-nanometer resolution of the piezoactuator, the leverage mechanism must be stiff, backlash free, and friction free. This introduces an extra level of complication to the device. To avoid ceramic damage, the coupling of the lever to the actuator must be very stiff in the pushing direction but should be soft in all other degrees of freedom.

3.2.1.2 Ring Piezoactuators

Ring piezoactuators have the same design principle as stack actuators with the exception of a through hole in the middle. The hollow stack is designed to accommodate feed-through electrical and mechanical components that are common in many applications. Generally, ring actuators can be designed with greater aspect ratios than simple stack actuators. This results in greater stability against bending and shear forces and allows the production of long actuators without an increase of the total ceramic surface area. Ring piezoactuators are very popular for dynamic applications because they can be cooled faster than stack actuators.

3.2.1.3 Bending Piezoactuators

Bending piezoactuators or *Bimorphs* utilize piezoceramic polarization perpendicular to the applied electric field. Electrical excitation of this characteristic results in planar motion within the ceramic. When a metal back plane is firmly attached to the ceramic, any electrical activation of the assembly will result in internal mechanical stress that will translate into bending movement of the composite structure. The maximum deflection depends on the length of the strip, the stiffness of the metal plank, and the intensity of the applied voltage.

3.2.1.4 Tube Piezoactuators

Monolithic ceramic tubes are another form of piezoactuators that utilize asymmetric polarization of the crystal. The ceramic element is shaped into a tube and the inside and the outside of the tube are covered with conducting film (See Figure 3.13).

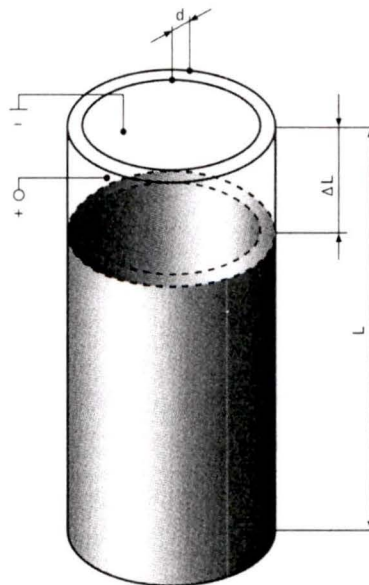


Figure 3.13: Tube actuators [18]

When voltage is applied between the inner and the outer ring, the tube expands along the L dimension and contracts radially. The overall effect is similar to the performance of piezoelectric ring actuators but the displacement is 50% less on average. In addition, tube actuators cannot withstand large bending and shear forces. These disadvantages are offset by the low price and simplicity of the tube actuators.

3.2.2 Parameters of Piezoelectric Actuators

Modern piezoactuators are produced with various characteristics that best suit different applications. In all cases, engineers base their designs on the actuator's technical data that is published by the manufacturers. The most significant actuator parameters are: stroke, force generation, stiffness, and resolution and accuracy.

3.2.2.1 Actuator Stroke

The strain of an actuator, measured as the ratio of its unexcited length over its fully expanded length, is known as the actuator's stroke. On average, modern piezoactuators show about 2‰ maximum strain. In practice, the value of the actuator's stroke is measured at room temperature at 10% of the maximum design load. The stroke of an actuator increases (stroke is a relative measurement) under increased mechanical load. As well, the stroke increases at higher temperature [19].

The data sheets of industrial actuators show two nominal values for the actuator's stroke. These values are known as A stroke and B stroke. The A stroke and the B

stroke for an actuator that is designed to operate at U_{\max} of 150V are shown on Figure 3.14.

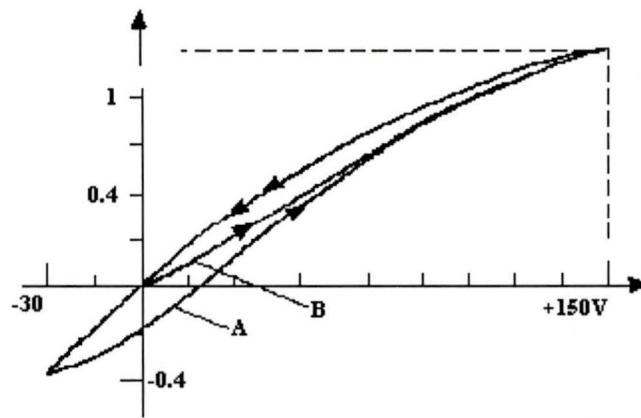


Figure 3.14: A and B stroke of piezoactuators [19]

The A stroke is measured for the maximum operational bipolar range of the device. In general, this range is between $-0.2 \times U_{\max}$ and $+U_{\max}$. B stroke is plotted for the maximum unipolar range of 0 V to $+U_{\max}$.

Figure 3.14 demonstrates that hysteresis effects can significantly affect the stroke of an actuator. However, the shown hysteresis characteristics are derived at room temperature under minimal load conditions and for short cycling periods. The exact shape of the hysteresis curves is a function of the operating conditions of the actuator. It is possible that some materials show remarkably increased hysteresis under real loads, elevated temperatures, etc. Controlling the hysteresis effects is very important and will be covered in a separate subsection.

3.2.2.2 Force Generation

The effective force produced by an actuator is its most valuable characteristic. The effective force depends on its stiffness c_t and the stiffness of the resistance c_s against which the actuator is pushing/pulling. Consequently, the generated force is given by the following expression 46:

$$F_{eff} = c_t \Delta L_0 \left(1 - \frac{c_t}{c_t + c_s} \right) \quad [46]$$

The ΔL_0 term is a result of the application of a static electric field and is equal to:

$$\Delta L_0 = EdL_0 \quad [47]$$

where d is in [m/V], and E is in [V/m]

Equation 46 demonstrates that the maximum force is generated when c_s approaches infinity. Such a condition is equivalent to zero stroke. Indeed, the maximum force generated by a piezoactuator is at zero stroke and is known as *blocking force*. Some industrial piezoactuators are capable of producing blocking forces in the magnitude of 10 kN to 45 kN.

Mechanical pre-stressing of piezoactuators is often used for improvement of the overall actuator stiffness and for compensation of tensile stress. The preload results in larger stroke and prevents damage from using the device with negative voltage. In addition, the application of mechanical pre-stress allows actuators to operate with high dynamic

acceleration forces. Without preload, the large alternating forces will immediately destroy the actuator.

In the case when sinusoidal voltage (AC voltage) with frequency f is applied to the same actuator, the resultant dynamic force can be computed with the following Equation 4:

$$F_{dyn} = \pm 4\pi^2 m_{eff} \frac{\Delta L_0}{2} f^2 \quad [48]$$

where $m_{eff}=m/2$ is in [kg], and f is in [Hz]

From Equation 48, the resonance frequency of the actuator can be calculated. The analytical expression for the resonance frequency is given by Equation 49 [9].

$$f_r = \frac{1}{2\pi} \sqrt{\frac{c_T}{m_{eff}}} \quad [49]$$

When piezoactuators operate in dynamic loading mode, 5% to 8% of the electrical energy input into the actuator per cycle is converted into heat. This could cause considerable rise in temperature during high frequency operations.

4.2.2.3 Stiffness

Piezo stiffness is an important parameter for calculating the force generation, the dynamic response, and the resonant frequency of a piezoactuator. Stiffness is a measurement of the elastic spring constant of the piezoactuator's assembly. Equation

46 demonstrates that high stiffness is desirable for high force generation capability and for minimizing the unwanted passive variations of the length of the actuator under loads. In practice, the stiffness of a low voltage actuator will be higher than the stiffness of standard high voltage actuator of the same size. The reason is that the high voltage actuators consist of a metal-ceramic compound structure, whereas the low voltage stack is a dense ceramic blocks [17].

The above argument is valid only when static force is applied to an actuator with shorted electrodes. Since piezo ceramics produce an electrical charge when mechanically stressed, when the electrodes are open, the electric charge cannot be drained from the PZT and generates a counter force to the mechanical stress. This is why a PZT element with open electrodes appears stiffer than one with shorted electrodes. The poling process of PZT ceramics leaves a remnant strain in the material that depends on the magnitude of polarization. Both the drive voltage and external forces affect the polarization and therefore the stiffness of the actuator. This explains why the dynamically measured resonance frequencies do not always agree with the predicted frequencies in Equation 49 [18].

3.2.2.4 Resolution and Accuracy

The resolution of piezoceramic actuators depends only on the applied electric field and is theoretically unlimited for a perfect voltage amplifier. The displacement of a piezo actuator is based on the orientation of electrical dipoles in the ceramic and external voltage is converted into a smooth linear movement. In fact, piezoactuators are capable of producing displacements smaller than the diameter of an atom. However, noisy and

unstable voltage sources greatly reduce the accuracy of the displacements achieved by the devices.

A major limitation of piezoceramic actuators, however, is their lack of accuracy due to hysteresis non-linearity and drift. Figure 3.14 illustrates that the maximum error due to hysteresis can be as much as 10-15% of the path covered when the actuators are run in an open-loop fashion. Because piezoceramic materials are ferroelectric, they fundamentally exhibit hysteresis behavior in their response to an applied electric field. The formation of hysteresis loop of piezoceramic actuators is a complicated phenomenon, and the microscopic explanation for the hysteresis is still unclear.

Ping G. et al present an explanation of the hysteresis phenomenon from a macroscopic viewpoint [20]. Based on this theory, the hysteresis loop is a consequence of the effects of domain switching due to the action of the external applied cyclic electric field. Since each domain is a composition of several parallel dipoles, the effective number of dipoles aligned in the direction of the electric field will be altered as domains switch under the action of an external electric field. This domain switching does not occur instantaneously and it is this delay response which gives rise to the hysteresis loop [20].

It should be noted that if the hysteresis effect is not incorporated into the piezoceramic actuator control system, it would act as an unmodeled phase lag whose presence will cause instability in a closed-loop system if sufficient phase margin is not provided. Many efforts have been made for improving the hysteresis behavior of the piezoceramic actuators. The schemes can be grouped into five main categories:

- Use of electric charge to drive piezoceramic actuators instead of applied voltage.
- Use of feed-forward non-linear models in driving the actuators.
- Use of closed-loop modified PID control schemes.
- The implementation of fuzzy logic control algorithms.
- Use of self-learning neural networks.

The closed-loop approach has become the most widely used method for increasing the accuracy of the modern piezoactuators. It offers very good linearity, stability, repeatability and accuracy. Closed-loop PZT agreements are equipped with position measuring systems that provides sub-nanometer resolution and bandwidths up to 10 kHz. In general, a digital servo controller determines the output voltage to the PZT by comparing a reference signal to the actual sensor position signal. The result is automatic compensation for varying loads or forces, virtual infinite stiffness, and elimination of hysteresis and creep effects.

Due to the unpredictable nature of the hysteresis effects, neural networks offer a promising alternative for the future. The neural network approach is very complicated and, at this point in time, still underdeveloped. However, the major strength of this type of controller is that there is no need for mathematical description of the plant operation. The controller performs similar to a human brain and learns how to avoid undesired effects. Several learning algorithms for neural networks have been proposed. However, none of the current methods has been proven reliable. A recent closer study of the Bayesian Learning for neural networks has exposed some promising features, but further study of the problem is required [21].

3.2.3 Practical Considerations

The performance and durability of piezoactuators depend on the operating conditions and the way the actuators are built. The reliability of piezoactuators is defined for steady state at high activation voltage and high dynamic cycling with high internal mechanical stress. Improving reliability and lifetime can be achieved by improving the way actuators are manufactured and installed in practical applications.

3.2.3.1 Actuator Breakage

Due to their nature, raw piezoelectrics are extremely fragile. If a piezoactuator is dropped during installation, it will most probably shatter upon impact. In addition, micro-fractures can develop after thousands or millions of repeated oscillations. With raw piezoelectric materials, these micro-cracks can expand and ruin the device. There are two major techniques to deal with the brittle nature of piezoelectric ceramics. However, none of them has been completely developed for industrial applications.

The first method is a result of extensive laboratory testing that has shown a direct dependence of the ceramic's grain size to its breakage tendency. Generally, the smaller the grains the less brittle the ceramic.

The second method involves packaging the actuators in polyamide coating. This process seals the fragile piezoceramics in a thin protective shell that absorbs various impact forces. The packaging also provides structural protection against micro-cracks by both preventing their formation and retarding their growth [4].

3.2.3.2 Lead Attachment

The manufacturer of piezoceramics must solder wires to the raw ceramic to provide electrical contact. This process is tedious and error-prone. Tedious, because in many applications, this is a manual, time-intensive technique. Error-prone, because solder does not adhere well to ceramics, so the solder joints are often the weakest link in the final product. In addition, solder-joint fatigue is accelerated by the high frequency oscillations of the actuators. The results are even worse when several piezoelectric elements have to be stacked together to form a multilayer actuator.

Unfortunately, there is no readily available solution for the lead attachment problems in piezoactuation. The implementation of semiconducting ceramics, like barium titanate, for electrodes is promising but its development is in the initial stages [24].

3.2.3.3 Mounting Guidelines

To achieve desired performance and to ensure a long, trouble-free operation, piezoactuators must be installed with extreme care. PZT stack actuators must be stressed only axially. Tip balls and flex couplings must be used to neutralize tilting and shearing forces. An external preload is recommended for applications requiring strong tensile forces. All manufacturers have an installation section in the technical data supplied with an actuator.

Chapter 4

Design of a Platform for Experimental Study of Active Vibration Control in Machining

4.0 Introduction

The control of mechanical structural vibrations is essential for realizing smooth-operating machines and reducing the acoustic noise generated by powered mechanical devices. Vibrations affect the quality of the finish in machining, reduce the life span of aircraft components, annoy automobile passengers, etc. Until recently, the only method of offsetting these undesired effects was the utilization of conventional passive damping components. Passive damping techniques are quite effective in reducing high-frequency mechanical vibrations. Unfortunately, the passive damping methods are inefficient against low-frequency vibrations. The recent advances in microelectronics and piezoelectric sensing and actuating have opened the possibility of applying active-control mechanical platforms for counteracting low-frequency mechanical vibrations.

A mechanical control platform is a system that exists for the purpose of regulating physical parameters in a desired fashion. Typically, a control system is an integration of many components or functional elements that produce a desired output. In a closed-loop active control system, there is typically a model of the system to be controlled, a control law, and some sensors that take measurements necessary to calculate a control

response. Piezoactuators and piezosensors, also known as adaptive materials, are becoming increasingly popular for designing active control systems. The practical use of adaptive materials in control systems presents challenges that are not commonly experienced in traditional implementations. Integrating the smart materials with the other components necessary to produce a structure that performs required functions in a predictable and repeatable manner is one of the greatest problems that the designer has to overcome.

This chapter introduces the background of active vibration control and presents an apparatus for studying and actively reducing mechanical vibrations in machining. Chatter vibrations in machining can be characterized with unpredictability, non-linearity, and large fluctuating forces. Such negative combination, most often, results in the destruction of either the machine tool or the machined part. The device described in this chapter incorporates a combination of precision piezotransducers, a fast switching piezoactuator, and Digital Signal Processing [DSP] motion control technology.

4.1 Background

Reducing unwanted vibrations has always been a concern for engineers. Not too long ago, the only methods available for reducing undesired vibrations were redesigning the product or incorporating passive damping components. Active vibration control is a modern alternative solution that can yield increased performance while saving valuable time and money.

Piezoelectric transducers are one of the most common means of producing and measuring vibration and sound. Piezoelectric transducers have enjoyed widespread use

over the last decade for vibration control in university, corporate, and government research laboratories. Unfortunately, their introduction into commercial applications has been lacking momentum. Utilization of piezotransducers and piezoactuators for suppression of chatter vibrations in machining is one particular application that has not fully benefited from the many possibilities this technique can offer.

The demands for high-shape accuracy, surface roughness control, and reduction of sub-surface damage on manufactured parts are continuously increasing. Traditionally, the production machining process consists of a roughing step and a sequence of finishing steps, like grinding and polishing. Presently, there is an ever-increasing demand for new processes that combine high removal rates with high surface quality in a single step. Classical solutions, based on traditional stiff guide-way technology, cannot meet the requirements of these new machining processes because the machine cannot effectively dissipate the energy transferred during the machining and the resultant vibrations make smooth finish impossible.

4.1.1 Active Control of Mechanical Vibrations in Machining

Piezoelectric actuators and transducers are common industrial devices used to generate and measure mechanical vibrations. Conversely, they are very suited for integration with passive and active electronic components to form systems that actively suppress mechanical vibrations. Such systems actively interact with the surrounding environment to achieve desired control and are referred to as *smart structures*. The early smart structures researchers envisioned piezoelectric actuators and sensors embedded in composite materials to create structures acting like artificial muscles,

nerves, and brains. Although this dream never fully materialized to date, the effort led to an innovative approach to transducer packaging that uses structural composite materials as a host into which the transducers are integrated. It is believed that such transducers will be widely used in future designs [3].

Presently, the most common approach to achieving active control with piezoactuators is integrating the device in a shunted configuration according to Figure 4.1. The one-DOF representation of the shunted configuration is quite accurate due to the typical one-dimensional nature of operation of the common piezoactuators.

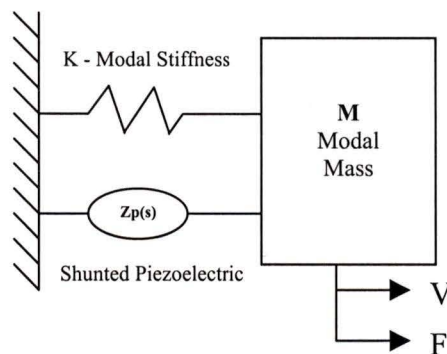


Figure 4.1: 1-DOF system with shunted piezoelectric actuator [25]

This approach is advantageous because, in combination with sensors and advanced DSP electronics, it can be used for practical implementation of closed-loop control strategies for active cancellation of mechanical vibrations and noises. A typical closed-loop disturbance control configuration is presented on Figure 4.2. Figure 4.2 shows the basic block representation of a piezo-based active cancellation of a time-varying disturbance $d(t)$ caused by a time-varying source $s(t)$. The source $s(t)$ is transferred into $d(t)$ through a physical mechanism called the plant. To cancel the disturbances by active means, the

structure incorporates sensors, a controller, and an actuator. The sensor measures the disturbance and passes it to the controller, which generates a control signal into the actuator. The actuator introduces an excitation that passes through the secondary plant and produces a reaction that counters the disturbance. The combined effect of the disturbance and the disturbance cancellation component produces the error $e(t)$ that is detected by the error sensor and passed to the controller for decision making calculations [6].

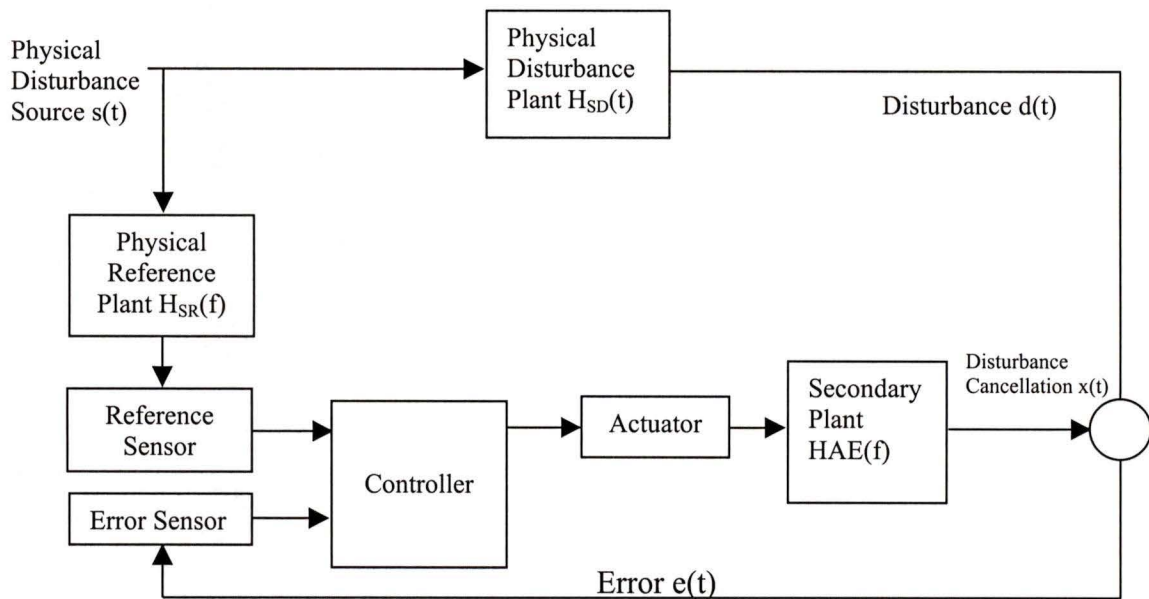


Figure 4.2: Active vibration control conceptual diagram [6]

In practical designs, the actuator cannot be directly coupled to the disturbance. It is connected through a physical plant $H_{AE}(f)$. The addition of a reference sensor as close to the disturbance source as possible is advantageous because it allows for the implementation of feed-forward control algorithms. When feed-forward control strategy is implemented, the error becomes small if the net transfer function from the

source through the reference sensor, controller, actuator, and secondary plant is comparable to the transfer function of the disturbance plant $H_{SD}(f)$. For an effective feed-forward control strategy, the control law must be constantly updated through adaptive means. If the reference sensor in Figure 4.2 is absent, the control strategy is limited to classical feed-back or state-space techniques [6].

The integration of the actuator system into the structure is traditionally done with one of the three methods shown in Figure 4.3. The methods are opposed force, compliant force, and structurally integrated.

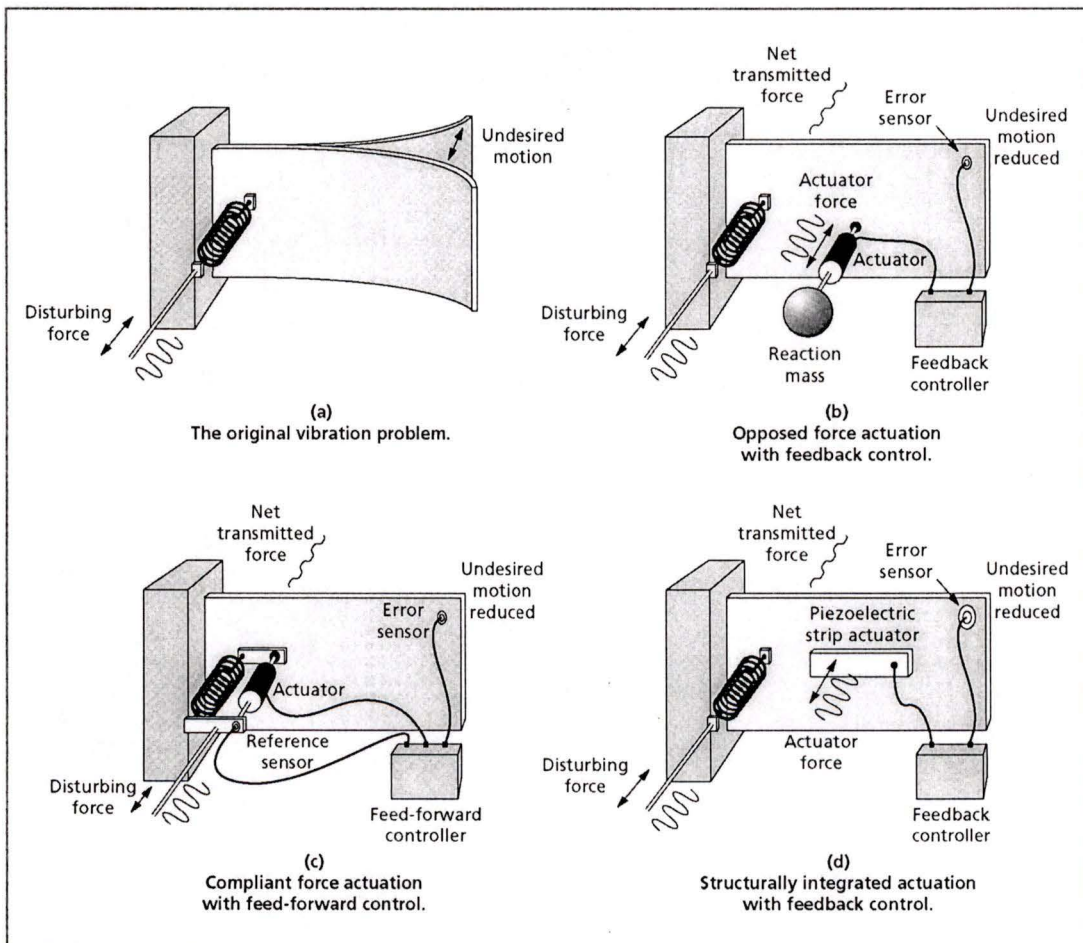


Figure 4.3: Basic actuation approaches [6]

Each approach can be combined with a variety of control strategies that lead to the desired performance. In the opposed force actuation mounting, the actuator produces force from a reaction mass. The compliant actuator mounting strategy targets active alteration of the transmission of the force disturbance into the structure. This approach is particularly popular with the automobile industry for design of active suspension shock absorbers. Finally, the integrated actuator is embedded within the structural material and actively changes the stiffness of the structure [6].

Damping of mechanical vibrations through active control means continues to capture the attention of researchers around the world. There are many innovative ideas that are currently under investigation. These projects target a variety of applications that require high precision. The following sections present three such examples from three different areas of technology.

4.1.1.1 Boring Bar Application for Turning

The actively controlled boring bar tool holder for turning operations has been designed and tested as a collaborative research project of the Lucent Technologies' Advanced Technology System for the Defense Advanced Research Project Agency (DARPA) and the Department of Defense (DoD) [6]. This design uses the natural resonance behaviour of a long overhang boring bar to counteract the cutting forces produced at the tool tip. Without active vibration suppression, the combination of these two effects leads to chatter vibrations that results in poor surface finish. Figure 4.4 shows a conceptual diagram of this approach. The tool-holding bar is cantilevered from a stationary clamp and the workpiece rotates on a horizontal lathe. The actuator is

mounted inside the bar in a opposed force configuration. The actuator is connected to a high-density tungsten reaction mass that is mounted on a hinge. When vibrations are present, even small angle displacements can produce reaction forces large enough to counteract the vibrations. The mass is pushed by a stack piezoactuator. The return motion force is produced by a counteracting spring. Although the piezoactuator produces small displacements, the overall displacement is adequate due to the mechanical advantage achieved through the hinged arrangement. An energy efficient switched capacitor amplifier powers the system [6].

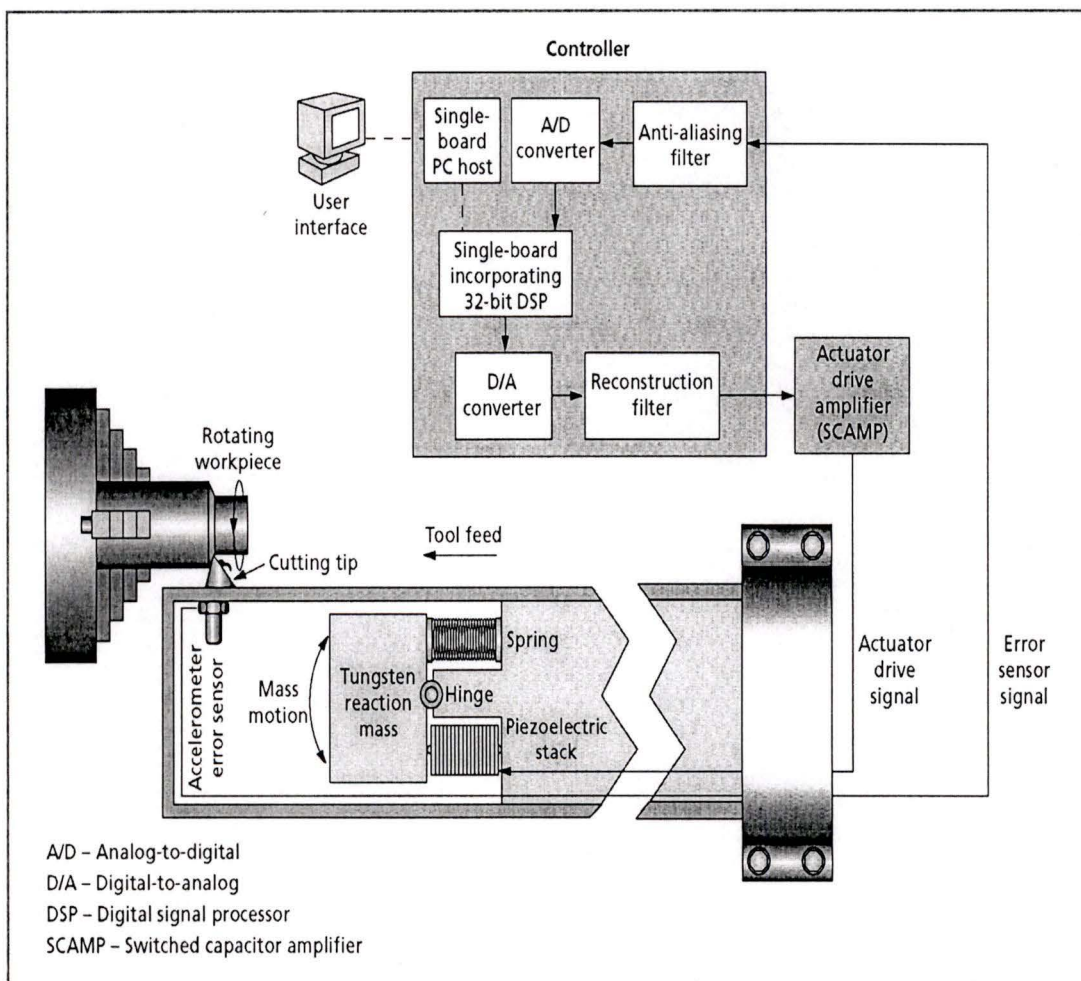


Figure 4.4: Actively controlled Boring Bar system [6]

The Boring Bar designers approached the chatter suppression task from a regenerative viewpoint. Conceptually, the regenerative theory describes chatter vibrations as a naturally occurring positive feedback mechanism that results from the overlapping of the cutting tip from one revolution to the next. The metal cutting process is caused by a large force applied by the tool tip perpendicular to the surface of the workpiece. If by random deflection, the tool produces an indentation on the surface, the tip will see it on the next revolution. When that happens, the tip will not have the surface support and the large constant orthogonal force will drive it into the metal. This process will produce a second indentation adjacent to the original indentation. Eventually, this repetition will produce a large gouge that will cause the tool tip to oscillate with growing intensity. The Boring Bar technique attempts to counter this regenerative process by interrupting the constant orthogonal force in a chatter suppression manner. Figure 4.5 shows the dramatic difference between the surface finish of a workpiece when cut with the control on and the control off.

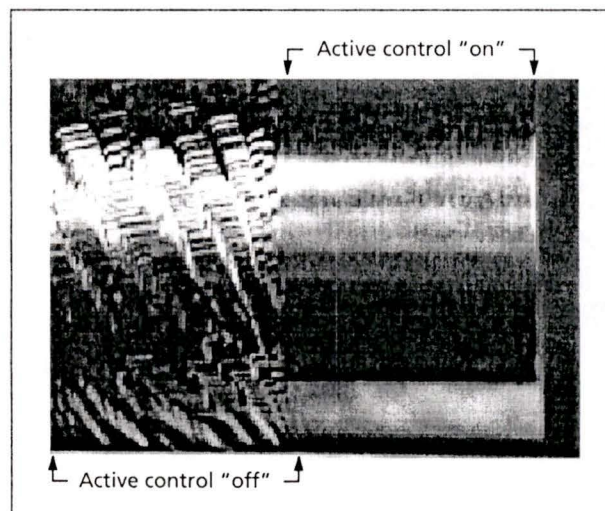


Figure 4.5: Surface finish comparison of surfaces produced with and without the Boring Bar active control tool [6]

The Boring Bar technique is very effective for cuts on workpieces of small length to diameter aspect ratios. Unfortunately, it is not feasible for cutting workpieces with large aspect ratio as the natural frequency modes of the workpiece will be interfering with the natural frequency modes of the tool and will be uncontrollably enhancing the vibrations rather than suppressing them.

4.1.1.2 Vibration Control for Active Bending of Structures

Suppression of mechanical flexing vibrations of the active elements of precision instruments is another area of intense research. One practical example is the work done at the Structural Dynamics and Vibration Control Department of the Sandia National Laboratories (SNL) in New Mexico. The research at SNL is targeting active damping of mechanical vibrations during ultra-fast positioning of magnetically levitated platens used in the production of silicon integrated circuits. The magnetically levitating platens exhibit 6-DOFs rigid body motion and are transported over 200 mm distances by non-linear magnetic actuator assemblies. The platens are magnetically suspended in order to eliminate inaccuracies due to machine tolerances, friction, hysteresis effects, and heat expansion. This allows positioning accuracy within 10nm. The flexible modes of vibrations of the platens are excited by inertial forces are the only limiting factor to achieving positioning cycles beyond 30 Hz [11].

The researchers at SNL designed an active damping system that was mounted on a prototype platen. The system incorporated a PZT stack actuator mounted flush with the platen top surface in an opposed-force manner. The actuator was placed in way that its motion suppresses the first two modes of vibration of the platen that are 972 Hz and

1619 Hz. The sample transfer function of the platen with and without the actuator is shown in Figure 4.6.

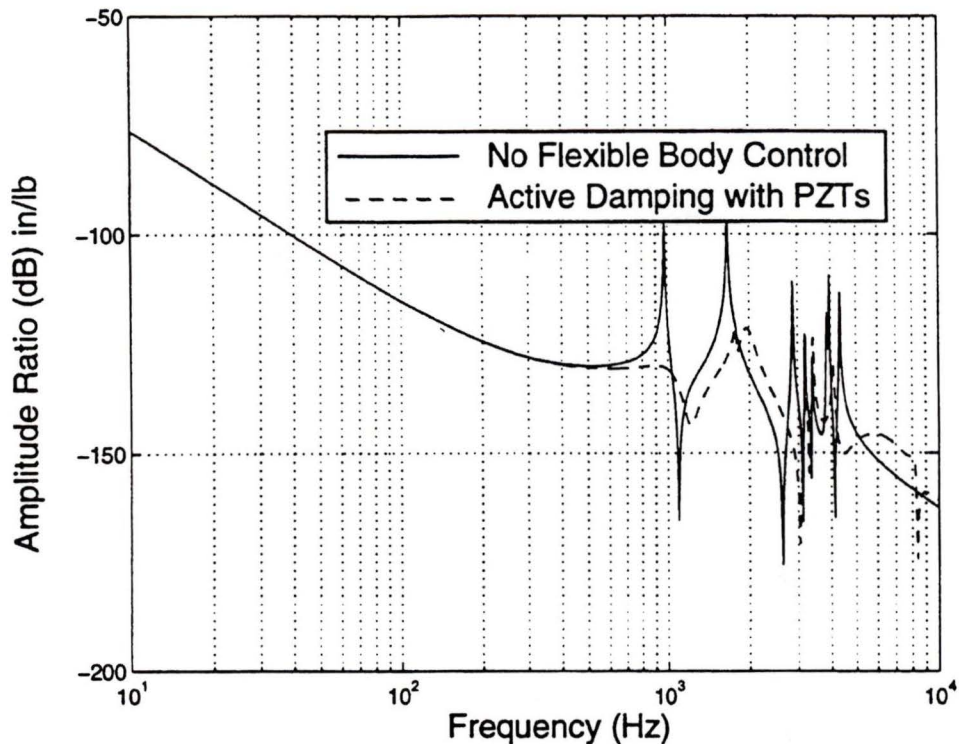


Figure 4.6: Sample transfer function with effect of flexible body control [11]

The active damping provides approximately 30 db of attenuation in the first and second mode of vibration that allows for increase of the maximum speed of platen positioning from 30Hz to approximately 125Hz. This corresponds to 416% performance improvement. An interesting observation recorded by the project researchers was the dramatic change of performance associated with varying the position of the actuator. These observations lead the investigators to the development of a finite element model of the structure and placing the actuator according to the strain pattern of the surface of the platen [11].

4.1.1.3 Generic Active Vibration Cancellation Mount

The Generic Active Cancellation Mount was designed at the Lockheed's Palo Alto Research Laboratories. The design incorporates shape-memory alloy springs acting as a passive isolator stage and a multilayer electrostrictive actuator for precise positioning and cancellation of transmitted forces. The purpose of the device is to address the generic mounting and vibration cancellation needs of precision space instrumentation. The principal of operation of that device is shown in Figure 4.7 [22].

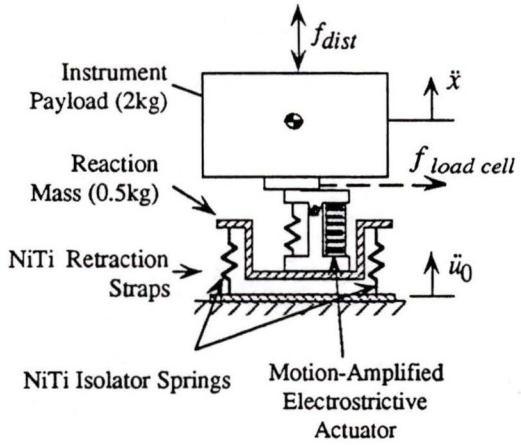
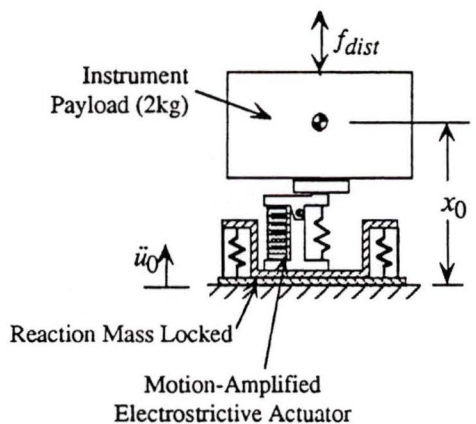
Device Configuration	Mode	Control Objective
	<p><u>Isolation</u></p> <p>base disturbance \ddot{u}_0</p> <p><u>Disturbance Rejection</u></p> <p>base disturbance \ddot{u}_0</p> <p>payload disturbance f_{dist}</p>	<p>Force Cancellation</p> <p>$f_{load\ cell} = 0$</p> <p>Acceleration Control</p> <p>$\ddot{x} = 0$</p>
	<p><u>Positioning + Disturbance Rejection</u></p> <p>payload disturbance f_{dist}</p>	<p>Position Control</p> <p>$x = x_0$</p>

Figure 4.7: Generic active vibration cancellation mount modes of operation [22]

The device operates in a single axis and employs nickel-titanium (NiTi) leaf springs in the passive isolation stage. The active stage is powered by a motion-amplified actuator that provides position control and payload disturbance rejection through an acceleration feed-back control loop. A cutaway of the device is shown in Figure 4.8.

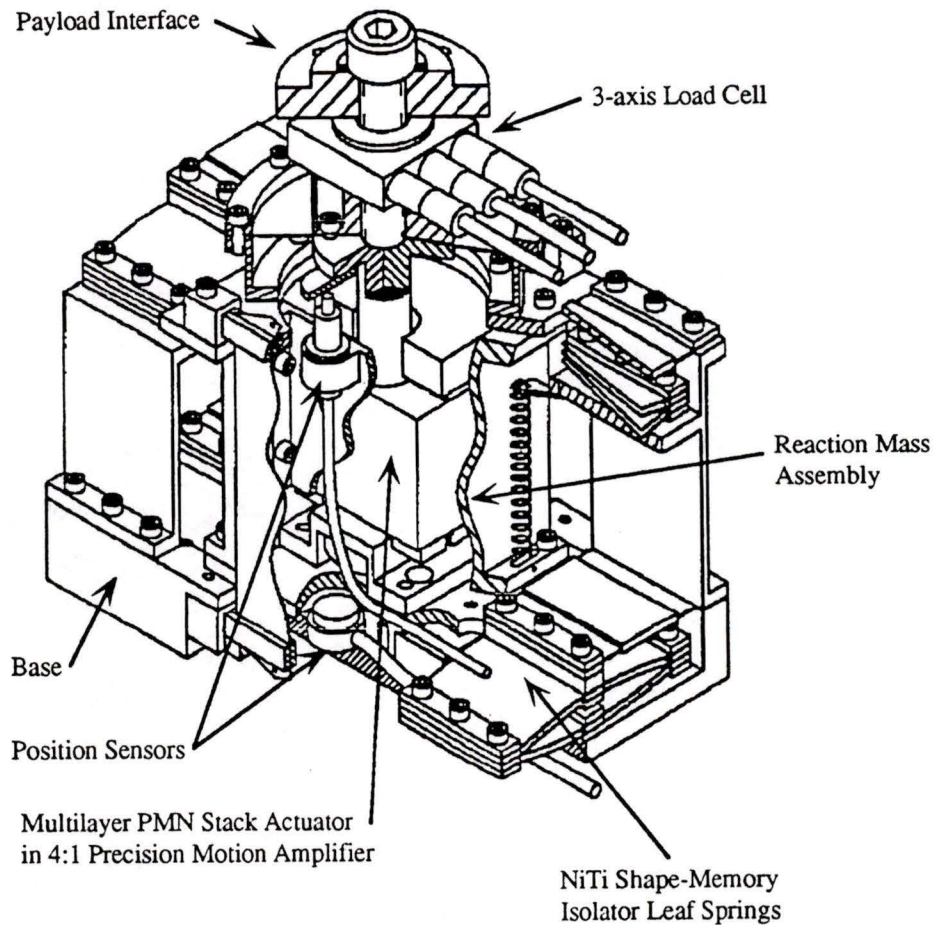


Figure 4.8: Cutaway view of the active vibration cancellation mount [22]

The Active Vibration Cancellation Mount is designed to provide significant attenuation of disturbances in the 20-200 Hz range for loads in the magnitude of 2 kg. Limitations of the device performance are almost exclusively related to the available stroke of the actuator. The condition is additionally worsened by the presence of the mechanical

amplifier assembly that provides 3.75 times increase of the end-point travel but significantly reduces the stiffness of the assembly. As a result, the device utilization is restricted within a tight specification bandwidth.

4.1.2 Vibration Phenomena in Machining

Machining chatter is a problem associated with most machining practices. In many instances, increasing or decreasing the cutting speed or changing cutting tools can simply eliminate the chatter. However, machine chatter can render a workpiece useless in a short period of time if left unattended. This results in not only a loss of material, but a loss of time as well.

Chatter phenomena are complicated and, despite the increasing research activity in the field, have not been fully investigated to date. In general practice, it is experience and observation that often prevents unexpected chatter vibrations. Simulation software tools for process optimization and troubleshooting, like CutPro[®] developed by the Manufacturing Automation Laboratories Inc., are becoming industry favourites as they offer methods of avoiding chatter vibrations [4]. The core computational engines that are used in these simulation packages are the results of many years of practical knowledge and research endeavors.

Fundamentally, chatter vibrations in machining are related to the transfer of energy during the cutting process. There are several theories that have been developed to describe this phenomenon. However, presenting the various approaches is outside the scope of this thesis. The cutting models used as a guideline during the design of the

chatter suppression device were developed and field-tested by Dr. Y. Altintas' research group at the University of British Columbia in Vancouver, Canada. The core objective of the approach is the macro-mechanics and the micro-mechanics modeling of the cutting process as a function of work material, tool geometry and material, chip load and cutting speed [1].

The macro-mechanics review at cutting produces a set of cutting coefficients that can be used to calculate the cutting forces, torque, power and chatter stability limits. The cutting coefficients have been developed through implementation of orthogonal cutting mechanics and mechanistic models. The micro-mechanics approach to metal cutting predicts the stress, strain and temperature distribution in the chip and tool. Its main application is tool design.

4.1.2.1 Mechanics of Metal Cutting

Most practical metal cutting operations are complex three-dimensional phenomena. However, a simplified two-dimensional orthogonal cutting example is sufficient for demonstrating the fundamental principles of automated metal removal. The orthogonal cutting macro-mechanics approach assumes that the plastic deformation occurs over a thin shear plane as shown on Figure 4.9. The cutting force in the radial direction is zero in orthogonal cutting as the cutting edge is perpendicular to the velocity of the material feed. In addition, it is assumed that the cutting edge is perfectly sharp and the metal removal occurs along the infinitely thin shear plane that is tilted at an angle ϕ_c in respect to the velocity vector. It is further assumed that all parameters are constant and all forces are in equilibrium. The process presented in Figure 4.9 is characterized with

three distinctive deformation zones. At the primary shear zone, the material ahead of the tool is sheared to form a chip. At the secondary deformation zone, the newly formed chip slides along the surface of the tool. Finally, the tool tip rubs over the newly machined surface in the tertiary friction zone [1].

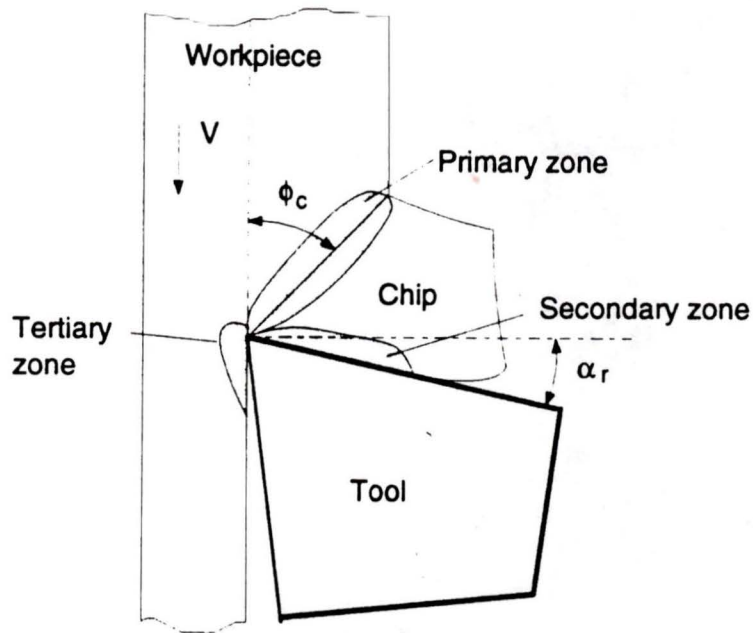


Figure 4.9: Deformation zones in orthogonal cutting [1]

The cutting force in the tangential direction is F_t and the cutting force in the feed direction is F_f . From force equilibrium, the total resultant force F exerted on the tool by the chip-removal process is the vector sum of the tangential and the feed forces. These forces are shown on Figure 4.10. In practical experiments, these forces are measured with force dynamometers. Since the measured forces are the result of superposition of the force contributions of the shear and rubbing phenomena, they are separated into shear (F_{tc}, F_{fc}) and flank contact/ploughing (F_{te}, F_{fe}) edge components. The cutting forces are assumed to be linearly proportional to the uncut chip area h and the edge forces are identified by extrapolating the measured forces at the zero cut thickness ($h = 0$)

intercept. The proportionality coefficient in the tangential and the feed direction are K_t and K_f respectively and the contributions of the edge forces are K_{se} and K_{fe} .

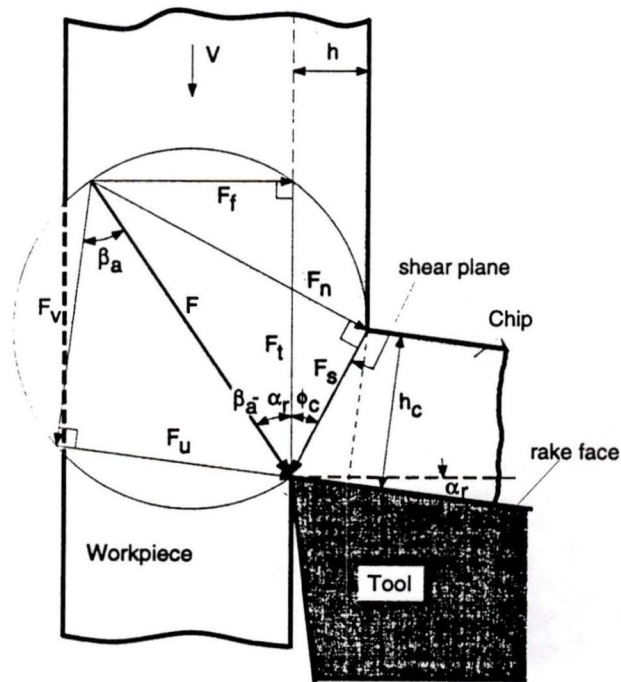


Figure 4.10: Cutting force diagram [2]

These coefficients are the slopes of the linear force plots of the force equations that are produced over a cutting depth b :

$$F_t = F_{tc} + F_{te} = K_t b h + K_{se} b \quad [50]$$

$$F_f = F_{fc} + F_{fe} = K_f b h + K_{fe} b \quad [51]$$

The machining coefficients K_t and K_f are known as specific cutting pressure and cutting force ratio and are directly calibrated from metal cutting experiments for a tool-workpiece set.

4.1.2.2 Fundamentals of Structural Vibrations in Machining

A simple 1-DOF structure can be presented as a combination of mass, a spring, and a damping element. When an external harmonic force $F_0 \sin(\omega t)$ is applied to such a system, the equation of motion for the system becomes [2]:

$$m\ddot{x} + c\dot{x} + kx = F_0 \sin(\omega t) \quad [52]$$

If Equation 52 is solved by utilizing the more convenient complex harmonic functions, the transfer function $\Phi(\omega)$ for the resulting amplitude can be expressed as a sum of a real component $G(\omega)$ and an imaginary component $H(\omega)$ according to [2]:

$$\Phi(\omega) = G(\omega) + H(\omega)$$

[53]

Where,

$$\left| \begin{aligned} G(\omega) &= \frac{1 - r^2}{k[(1 - r^2) + (2\zeta r)^2]} \\ H(\omega) &= \frac{-2\zeta r}{k[(1 - r^2) + (2\zeta r)^2]} \end{aligned} \right. \quad [54]$$

When the external forces are periodic but not harmonic, the force $F(t)$ can be expressed in Fourier Series according to:

$$F(t) = \frac{a_0}{2} + \sum_{n=1}^{\infty} a_n \cos(n\omega t) + \sum_{n=1}^{\infty} b_n \sin(n\omega t) \quad [55]$$

The response of a 1-DOF system to a periodic, non-harmonic function can be calculated by superimposing the contributions of each harmonic component of the periodic force $F(t)$. Substituting Equation 55 into Equation 52 leads to:

$$x(t) = \sum_{n=0}^N \frac{C_n}{k \sqrt{(1 - n^2 r^2)^2 + (2\zeta nr)^2}} e^{j(n\omega t - \alpha_n - \phi_n)} \quad [56]$$

In practice, the first four to five harmonics are sufficient to describe the vibration phenomena. In the majority of cases, any harmonic past the third harmonic does not represent sufficient energy that can cause relevant vibrations. As an example, the active cancellation of mechanical vibrations device presented in section 4.1.1.2 achieves a 416% improvement by suppressing only the first two harmonics of vibration. The majority of external force excitation associated with chatter phenomena in machining are described with periodic but not harmonic forces [2].

4.1.2.3 Chatter Vibrations in Cutting

The nature of chatter vibration in machining is associated with random self-excitation mechanisms in the chip generation process of metal removing. The presence of large cutting forces during normal machining operations excites the natural vibration modes of the tool-workpiece set. The resulting vibrations end in wavy surface finish. When the tool tip passes over the surface during the successive revolution, the chip thickness will vary as a result of the phase shift between the oscillations of the tool and the oscillatory surface produced during the previous pass. This mechanism is demonstrated

in Figure 4.11. The change in chip thickness causes changes in the cutting forces that in return feed additional vibrations in the successive revolutions. The growing vibrations are regenerative and may become substantial enough to cause tool damage or workpiece destruction.

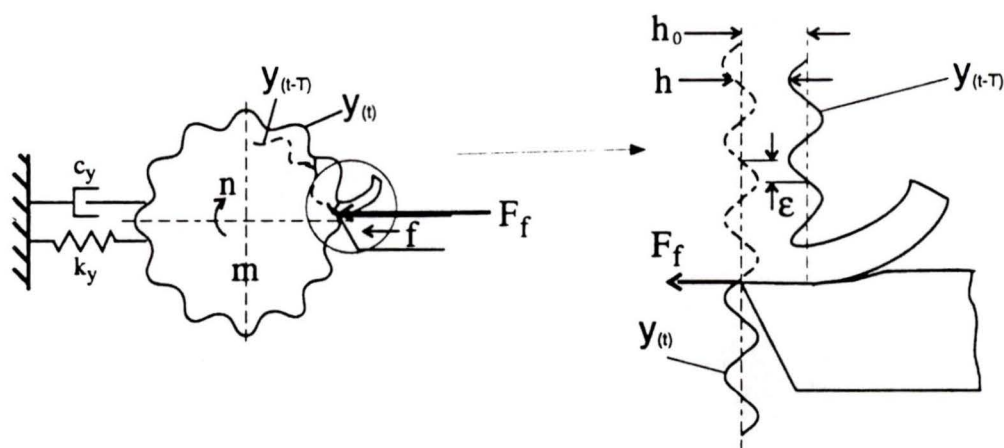


Figure 4.11: Regenerative wave generation [2]

Another chatter generation mechanism is mode coupling. Mode coupling occurs when vibrations exist in more than one direction in the cutting plane. However, mode-coupling chatter occurs later than regenerative chatter and therefore it is generally less important from a practical perspective [2].

As Figure 4.11 shows, the chip thickness is not constant and varies as a function of vibration frequency and the revolution period T . The dynamic chip thickness can be expressed as [2]:

$$h(t) = h_0 - [y(t) - y(t-T)] \quad [57]$$

Then according to Equation 51, the feeding force $F_f(t)$ becomes:

$$F_f(t) = K_f b h + K_{se} b = K_f b (h_0 - [y(t) - y(t-T)]) + K_{se} b \quad [58]$$

Substituting Equation 58 into Equation 52 produces the fundamental equation of 1-DOF chatter dynamics:

$$m\ddot{y} + c\dot{y} + ky = K_f b (h_0 - [y(t) - y(t-T)]) + K_{se} b \quad [59]$$

In addition to the previously described repetitive regenerative phenomena, unpredictable surface marks and deviations of material characteristics can further promote the generation of chatter vibrations. In general, the process of chatter excitation is extremely complex and nonlinear to model with analytical methods. Best results are achieved with the implementation of numerical analysis finite element techniques [2].

The generation of chatter vibrations can be illustrated with the block diagram shown in Figure 4.12.

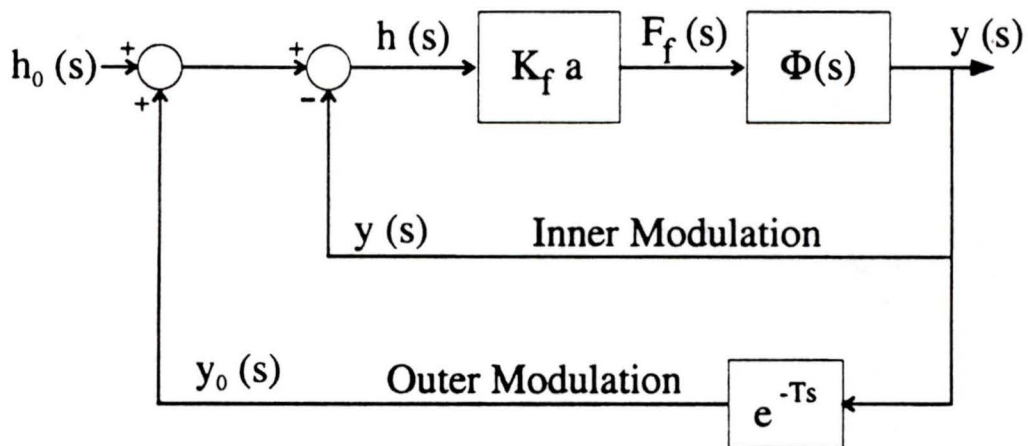


Figure 4.12: Chatter dynamics block diagram [2]

The functions in Figure 4.12 have been converted in Laplace domain. The input to the system is the desired chip thickness $h_0(s)$ and the output is the vibration $y(s)$ that is imprinted on the inner surface. Analysis of the transfer function produced from the block diagram from Figure 4.12 produces an equation for the critical stability of the system. Substituting $s=j\omega_c$, the borderline characteristic function becomes:

$$1 + (1 - e^{-j\omega_c T})K_f a_{\text{lim}} \Phi(j\omega_c) = 0 \quad [60]$$

In Equation 60, a_{lim} is the maximum axial depth of cut for chatter vibrations free machining. Solving Equation 60 leads to:

$$a_{\text{lim}} = \frac{-1}{2K_f G(\omega_c)} \quad [61]$$

Equation 61 demonstrates that the critical depth of cut is inversely proportional to the cutting constant K_f and the flexibility of the structure. Harder workpiece materials have greater cutting constants and the maximum depth of cut is therefore smaller. Similarly, more flexible workpieces result in reduced maximum depth of cutting. At the same time, Equation 61 demonstrates that chatter can be avoided at any speed as long as the maximum depth of cutting is below the calculated values [2].

4.2 Platform Design

To prevent the negative effects of the large, unpredictable, and non-linear fluctuating chatter forces, a 1-DOF piezoelectric-actuated device has been designed and implemented as shown in Figure 4.13.

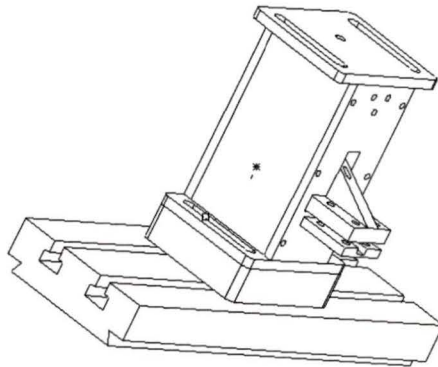


Figure 4.13: Piezoelectric device for control of chatter forces

The device employs a piezoelectric translator acting upon a drum. A spring-mounted cutting tool rests against the only unconstrained edge of the drum. The design allows for two modes of operation that are functionally separated by a preset internal preload. The first mode of operation is passive and, for as long as the system sensors register contact and the cutting forces remain steady, no active control is attempted. When the original preload is overcome by the presence of a large external cutting force, the device reacts in a way that counter-acts and stabilizes the external disturbance. The design approach that was implemented in the research process involved several distinctive steps that are:

- Conceptual proposal
- Requirements identification
- System design
- System integration
- Testing
- Improvements and fine-tuning

4.2.1 Conceptual Proposal

As discussed in the previous sections, the most common approach to achieving active control with a piezoactuator is integrating the device in a shunted configuration according to Figure 4.1. Such deployment results in a second-order differential equation similar to Equation 52. The second order term is due to the presence of significant mass that results in considerable reduction of the system's resonance frequency and in substantial phase shift.

Although it is impossible to design a massless device, it is feasible to greatly reduce the influence of the mass component to a level where it becomes insignificant. For obvious reasons, such a design must incorporate lightweight components. On the other hand, lighter components are generally associated with lower stiffness, which according to Equation 49 will reduce the natural frequency and will therefore not be capable of producing smooth finishes. In addition, chatter phenomena are unpredictable and in the majority of cases, the tool holder will normally operate under chatter-free conditions. Therefore, the new design must offer acceptable performance in two functionally very different modes of operation: normal mode of operation and chatter suppression mode.

The performance of traditional tool-holders is sufficient under chatter-free conditions. It makes most sense that during the normal mode of operation, the device operates passively while sensor-monitoring the cutting force for signs of chatter vibrations. If chatter vibrations occur, or are close to occurring, the system must respond to actively suppress the undesired effects. As presented in a previous section, chatter occurs as a

result of the periodic fluctuations of the cutting forces. Therefore, a device capable of active cutting-force control will theoretically be capable of reducing the regenerative phenomena that lead to catastrophic chatter vibrations.

Figure 4.14 shows the theoretical operation of a system that naturally has two modes of operation.

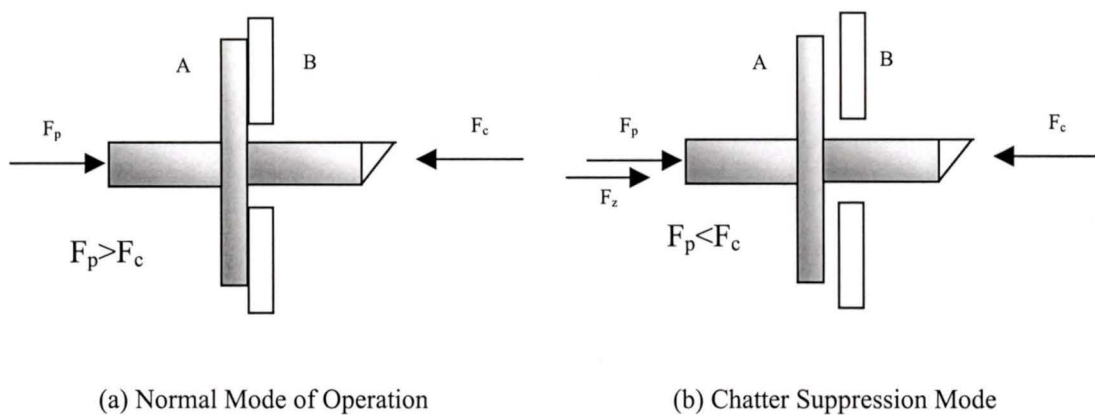


Figure 4.14: Basic principle of operation of the new tool holder

During the normal mode of operation shown in Figure 4.14a, the cutting force F_c is smaller than the preload force F_p . The reaction forces between the tool A and the housing B compensate the difference in the force balance and no motion of the tool occurs. When the external cutting force begins to fluctuate due to vibration phenomena and exceeds the preload force F_p , the force equilibrium will be distorted and the tool will separate from the housing B. As explained in section 4.1.2.3, the periodically fluctuating cutting force will cause the tool to oscillate against the workpiece as shown in Figure 4.14b. If an actuator, connected in series with the tool, exerts a control force F_z against the cutting force, it is possible to quickly restore the system's equilibrium and counteract the vibrations. In addition, if the device can predict the occurrence of

chatter vibrations before they occur, it is possible to deploy the control force earlier in a chatter preventive fashion.

4.2.2 Requirements identification

The model shown in Figure 4.14 is just a basic conceptual representation of an idea. In reality, the tool will have characteristic stiffness and the housing point of contact will have characteristic stiffness as well. In addition, since the monitoring of the housing contact forces is essential for the implementation of a chatter preventive control strategy, the device will be equipped with sensors at these points. Figure 4.15 represents a realistic model of the proposed system.

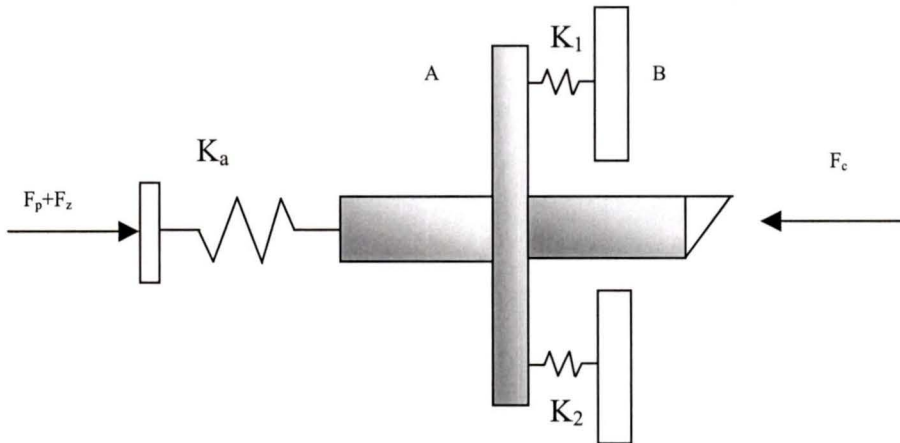


Figure 4.15: Chatter suppression tool holder

The values of the sensor stiffness K_1 and K_2 and the combined value of the internal stiffness and the actuator stiffness K_a are critical for the effective operation of the device. The only way the model in Figure 4.15 can become theoretically equivalent to the ideal model in Figure 4.14 is through the implementation of sensors and actuators that have stiffness coefficients close to the stiffness coefficients of the solid material

that the housing is made of. As previously presented, piezoelectric sensors and actuators have characteristic stiffness values close to the stiffness of high-quality steel.

Chatter vibrations events are delayed by at least one revolution as described in section 4.1.2.3. If a workpiece revolves at 3000 rpm, then it takes 0.02 sec for one revolution to occur. That is the time available to the control system to counteract the vibration forces and restore the normal cutting conditions. If the control electronics implements 100 control signals per revolution, then the actuator should be capable of expanding within $0.02/100 = 0.0002$ sec. In addition, depending on the conditions, the cutting forces that lead to chatter vibrations can reach levels in the kilo-Newton range. This requires actuators capable of producing large expansion forces very rapidly. As introduced in Chapter 3, piezoelectric actuators are the natural choice for achieving such performance.

4.2.3 System design

A crucial step in implementing the proposed design is selecting the active elements and the passive elements to be used in the system. To turn the conceptual idea from Figure 4.14 into a real design, integrating piezoelectric sensors and actuators, it is necessary to begin with a general design diagram that identifies the main components. Figure 4.16 is a general system diagram of the proposed chatter vibration tool. When tool chatter is detected and the system's electronics is activated, the piezoactuator (1) pushes upon the drum (2), which in turn acts upon the cantilevered spring (3) and creates a control force counteracting the cutting force. The control signal is generated as a result of real-time processing of the force data collected by the three system sensors.

The drum is restricted in 4-DOF and can move only along the x-axis and y-axis. The drum has a single point of contact (point B) with the actuator due to actuator mounting restrictions as presented in Chapter 3. The drum transmits the actuator force to the tool over a line of contact (line A).

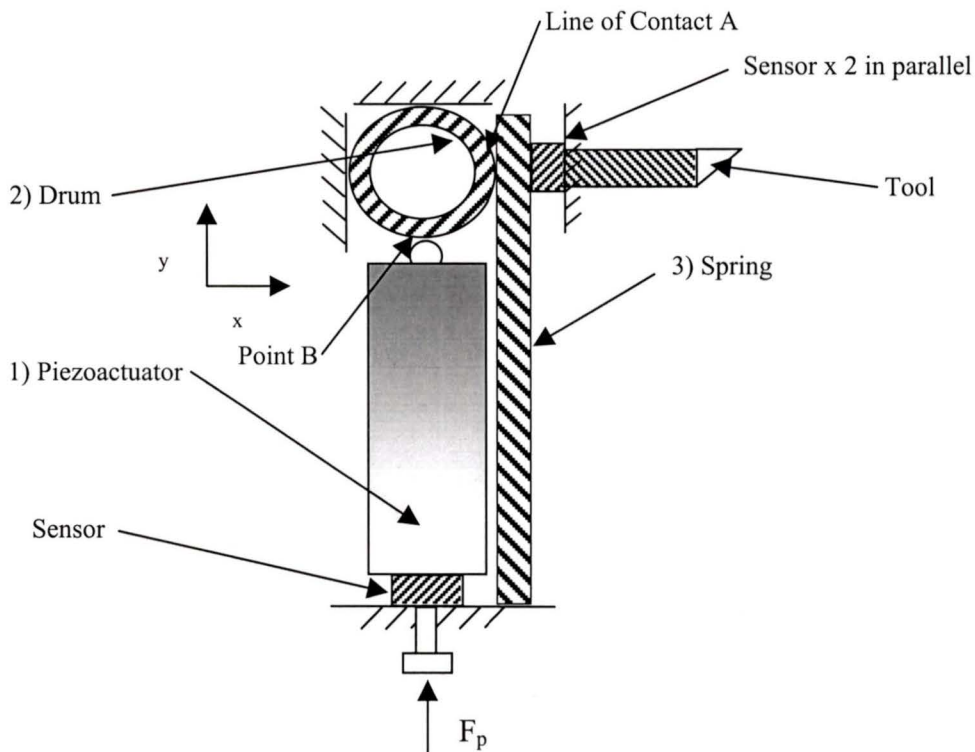


Figure 4.16: Chatter suppression tool system diagram

A circular drum has been selected for transferring the force. Drum springs offer very high stiffness to mass ratio. In addition, the use of drum eliminates the sliding motion that is typical for traditional spring elements. The actuator is mounted in the vertical direction for space optimization and taking advantage of the drum force-transmitting element. Spring (3) supports the tool and prevents bending around the x-axis. The system has a mechanism for applying the preload. This is accomplished with a screw mechanism mounted at the bottom of the actuator. A sensor positioned between the

preload mechanism and the piezoactuator measures the preload in the x direction. The two parallel sensors mounted between the drum and the housing measure the preload in the y-direction and detect any load differential that is associated with bending. Once the device is assembled, the preload is set as a constant.

As mentioned earlier, correct system stiffness calculation is critical for designing a practical device. The stiffness of all elements of the design is readily available as most of the components are off-the-shelf and come with detailed data sheets. The only element stiffness that has to be calculated is the stiffness of the drum. A thorough analysis of the drum and piezoelectric translator contact must be performed to establish the feasibility of the device. However, the enclosure must first be designed in order to establish the drum dimensions before the analysis can proceed. To design the enclosure and related components, the appropriate force sensors and piezoactuator must be selected beforehand.

4.2.4 System integration

The main elements of the system are: the force sensors, the piezoactuator, the drum, the drum and support components, and the control electronics. The selection of these components is presented in the following sections.

4.2.4.1 Force Sensors

Three force sensors are required for the correct operation of the device. One sensor is mounted beneath the piezoelectric actuator to measure the translator force. The remaining two sensors are mounted between the spring and the housing to measure the

force produced by the cutting tool during operation. These two sensors are used to detect any twisting motion or unequal loading of the spring.

As discussed in Chapter 3, Low Voltage Impedance Mode piezoelectric sensors are the appropriate choice for dynamic applications. The force sensors selected for the device are Low Impedance Voltage Mode (LIVM) piezoelectric force sensors, series 1051V, manufactured by Dytran Instruments Inc. These sensors are characterized with high stiffness and strength, as well as wide dynamic range. The two sensors selected for the cutting tool force each have a compression range of 1000 lbf with a nominal sensitivity of 5 mV/lbf. The force sensor selected for the translator has a range of 5000 lbf and a nominal sensitivity of mV/lbf. All sensors can be manually preloaded.

4.2.4.2 Piezoelectric Actuator

A piezoelectric translator, manufactured by Piezomechanik GmbH (part # PSt 1000/25/80 VS35), is the chosen actuator. The actuator is a stack design and has a length of 96 mm, a diameter of 35 mm, a compressive stiffness of 200 N/ μm , a prestress force of 2000N, and a measured maximum stroke of 95 μm at +1000V control signal. The translator is fitted with a spherical stainless-steel contact tip. The natural frequency of the actuator is 23 kHz. The expansion time is then $(0.33*23,000 \text{ Hz})^{-1} = 0.00013 \text{ sec}$.

The actuator is designed for fast dynamic switching operations in combination with a recharging amplifier. The recharging amplifier is part # RCV 500/400 also manufactured by Piezomechanik. The amplifier has a voltage range 0 V thru +500 V, a peak current of 4 A, and a resonance frequency of 2 kHz.

4.2.4.3 Enclosure and Support Components

The enclosure and the support components of the device are the piezocator, spring, drum supports, tool holder, box enclosure, and riser. Figure 4.17 shows the major parts of the design.

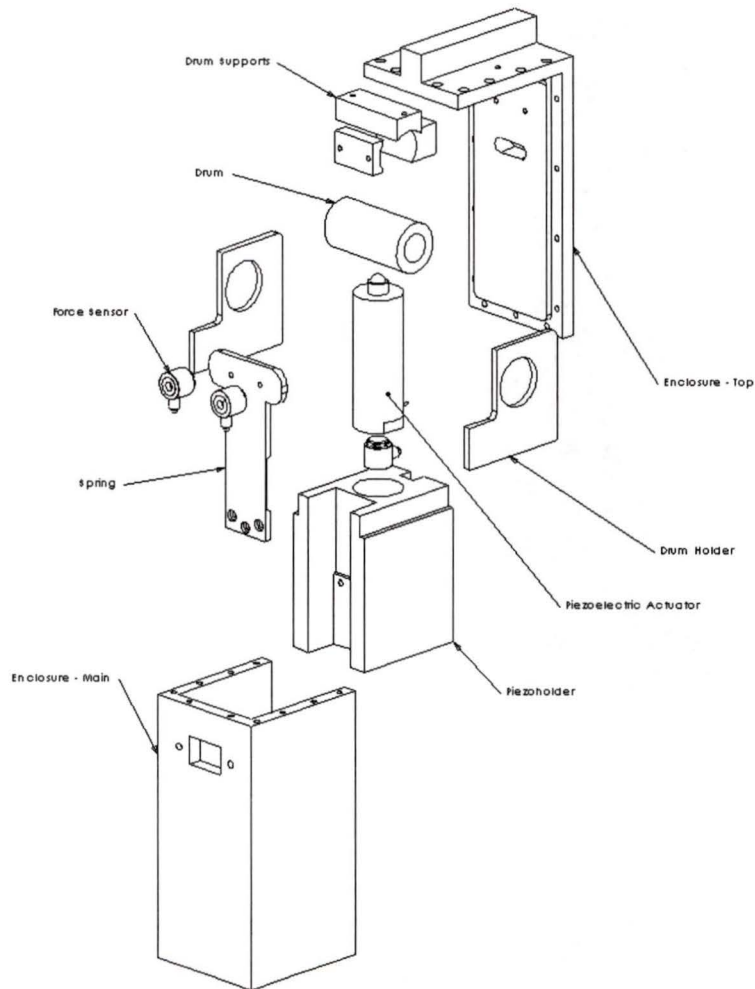


Figure 4.17: Chatter suppression tool components

The piezocator is designed to hold the piezoelectric actuator within the enclosure as well as providing a mounting location for the spring. The locator is manufactured from

AISI 1018 steel. Several small modifications were made to this component in response to unforeseen clearance issues.

The spring component serves several functions. In addition to allowing tool movement, the spring provides mounting locations for the force sensors and drum support. One end of the spring is attached to the locator. The force sensors and drum supports are attached to the other end. The upper tool holder is attached directly above the force sensors. The spring was also manufactured from AISI 1018 steel.

The three drum supports firmly secure the drum in position allowing it only 2-DOF. The bottom and back drum supports are mounted from the exterior of the box while the spring drum support is attached through the spring to the force sensors via countersunk bolts.

The cutting tool is attached to the device by way of a two-piece tool holder. The upper portion of the tool holder is shaped like an inverted “T”. This component is fixed to the spring by three bolts. The lower portion of the tool holder mounts underneath the upper, sandwiching the cutting tool. The upper and lower components are then assembled using four Grade 8 bolts.

The box enclosure portion of the device is comprised of six separate components: top, bottom, front, back, and two sides. All the components are manufactured from a minimum ½ inch thick AISI 1018 plate. The tool holder protrudes through the front plate to access the workpiece. The front and back plates are attached to the side plates by six ¼ - 28 UNF Grade 8 bolts per side. The entire assembly is then bolted to the riser by four ½ inch threaded rods.

The riser serves as the mounting point for the device. The riser is attached to the table via four T-bolts before the rest of the assembly is fastened in place. There is a small recess in the top of the riser to allow positive location edges for the box, clearance for the T-bolts, and cable access. The riser was also constructed of AISI 1018 steel.

4.2.4.4 Drum

The drum is essentially a tube-shaped beam. The housing sides locate the drum, the drum holders, and the piezoactuator. The force of the piezoelectric translator acts as a point force at the mid-point of the beam. As the only unconstrained edge of the drum is the one that is next to the spring, the force of the translator is transferred to the spring, and in turn to the cutting tool tip. The drum must be further examined in order to determine if it is able to transfer the force generated by the piezoelectric translator to the cutting tool tip. By analyzing the contact between the piezoelectric translator and the drum using finite element analysis, the resultant forces at the edge of the drum and the stiffness of the drum can be calculated.

Finite element analysis was used to model the contact between the piezoelectric translator and the drum. While modeling the loads and constraints is relatively straightforward, modeling the deformation at the contact point between the two curved surfaces of the piezoactuator's tip and the drum is a very difficult procedure. The analysis is additionally complicated by the relationship between the force generated by the piezoactuator and the characteristics of the drum. As introduced in Chapter 3, the force generated by a piezoactuator depends on the stiffness of the object that is being

pushed and the relative expansion of the piezo stack. On the other hand, the stiffness of the drum and the deformation in the area of contact depends on the force produced by the actuator. Calculating the stiffness of the drum can only be achieved by recursive methods; i.e. starting with an arbitrary force, calculating the stiffness of the drum and then matching the deflection which should be common for the drum and the actuator. This process is recursively implemented by using the stiffness value calculated during a previous run for calculating a stiffness value closer to the real value. The process repeats until a common displacement is produced for both the drum and the actuator. It makes most sense to begin the calculations with the maximum blocking force of actuation and the free expansion of the actuator.

4.2.4.4.1 FEA Model

The goal of the FEA model is to calculate the stiffness of the drum in the direction of the actuator expansion, the force transmission ratio, and the deformation profile that occur as a result of the actuator force. The half-drum and translator tip were modeled using Ansys 5.5.1/University high option. Due to symmetry, the drum/piezo tip system can be modeled as the half-structure illustrated in Figure 4.18. The half-drum, calculated after 6 consecutive repetitions, has an outside diameter of 35 mm, an inside diameter of 20 mm, and a length of 35 mm. The deformable top part of the translator has a diameter of 10 mm and a length of 15 mm. The drum's surface areas were divided into eight equal sections in order to provide constraint locations as well as evaluation points. The model was not further simplified because of the load cases being evaluated.

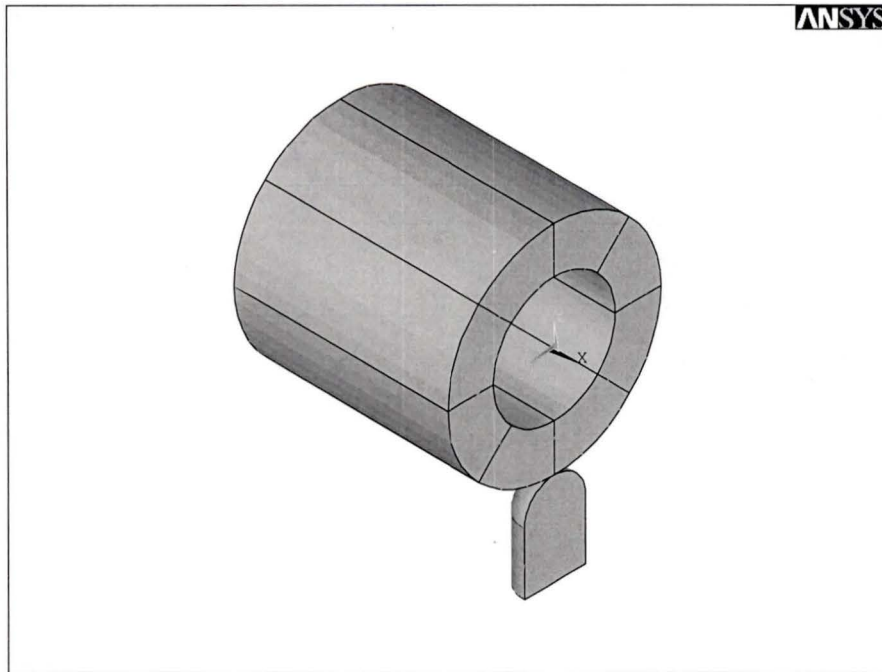


Figure 4.18: FEA model

The lines and associated keypoints are as illustrated in Figure 4.19.

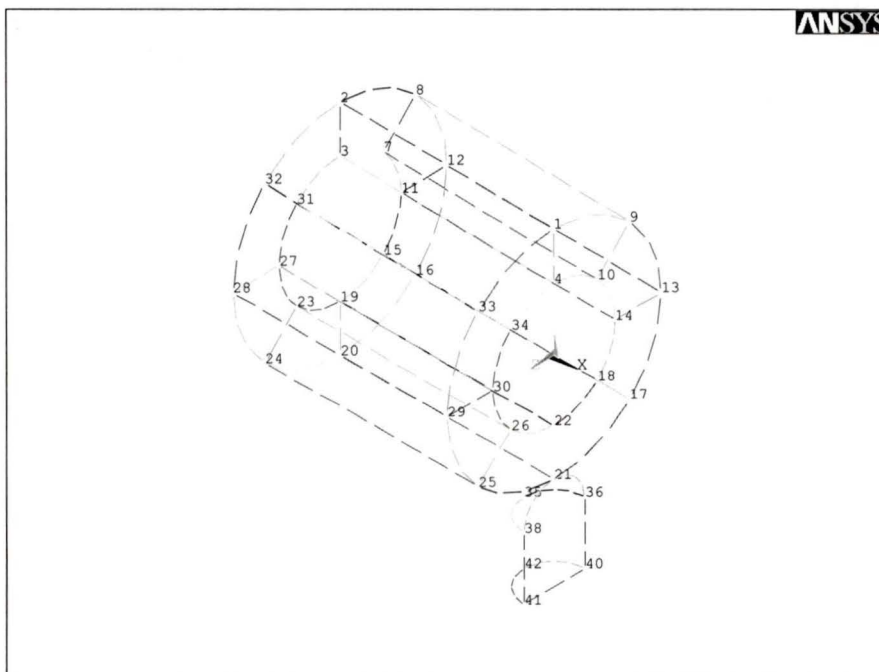


Figure 4.19: Line representation with keypoints

Constraints will be placed along several of the lines while a load is applied to the bottom surface of the actuator tip.

The material properties were then selected from the Ansys material library. The material chosen was AISI 1020 steel with $E = 207 \text{ GPa}$, density = 7850 kg/m^3 , and Poisson's ratio of 0.29. The element type for the solid volume was then selected. A ten node tetrahedral element (SOLID92) was chosen because of its large deflection and strain capabilities. After selecting the appropriate material properties and element styles, the model is meshed using the mesh tool within Ansys as illustrated in Figure 4.20. Several refinements were necessary to produce a satisfactory mesh

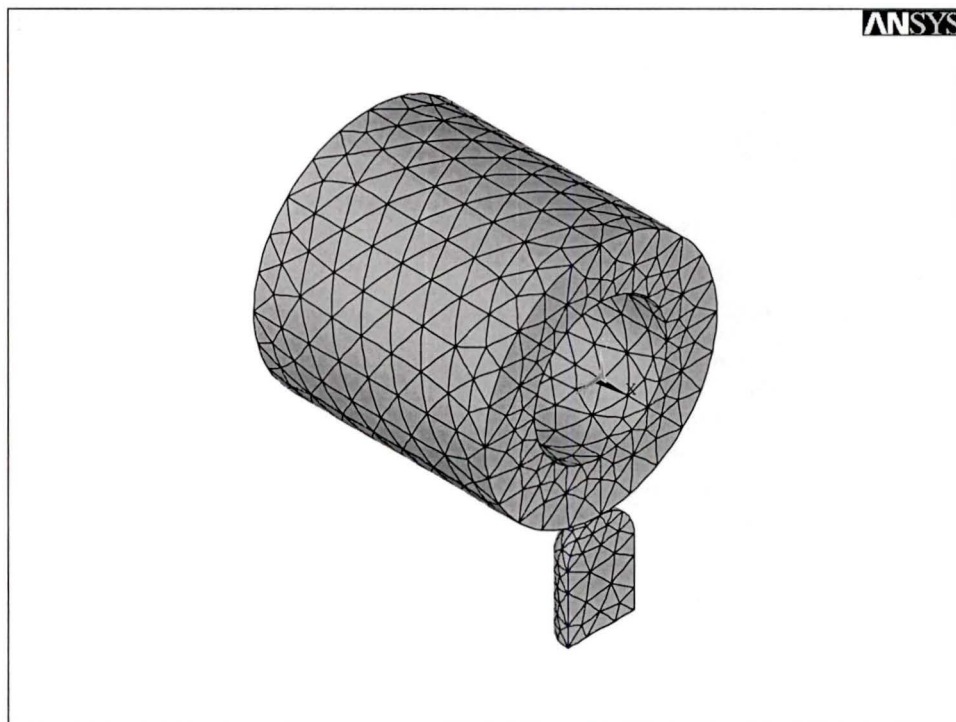


Figure 4.20: Meshed FEA volume

Once the volumes have been meshed, a contact pair was created using the Contact Wizard feature of Ansys as illustrated in Figure 4.21. A flexible-flexible contact was selected with the drum as the target element (TARGE170) and the translator tip as the contact element (CONTA174).

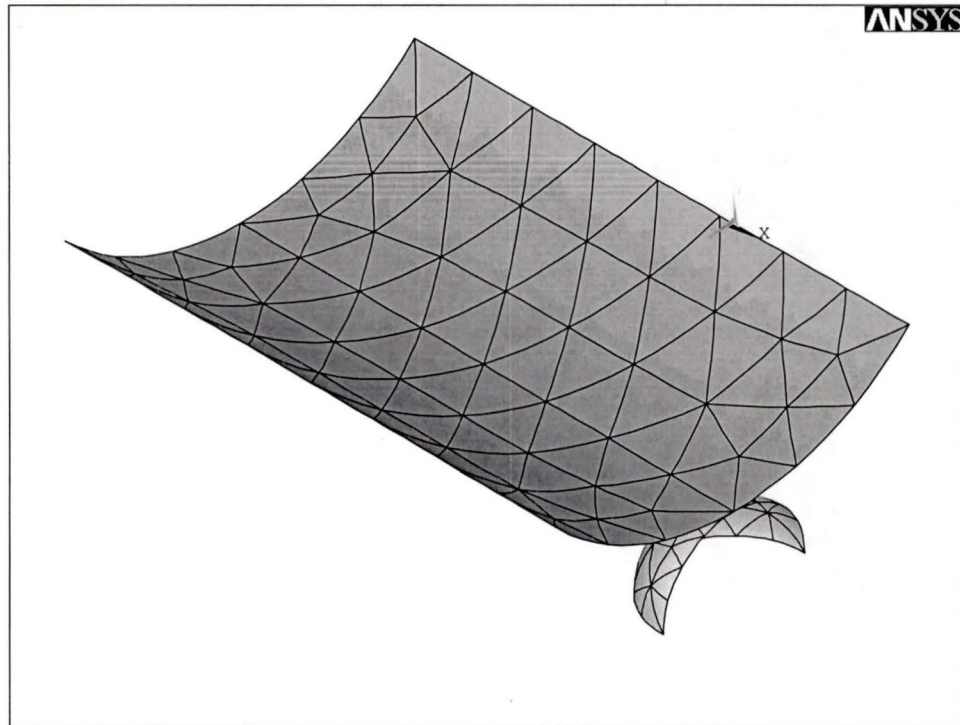


Figure 4.21: Contact elements

4.2.4.4.2 Constraints

After all of the elements have been defined, the drum and the translator constraints can be applied as shown in Figure 4.22. Symmetry constraints were applied first to model the other half of the components. The far edge of the drum was then constrained in all degrees of freedom in order to simulate the mounting method. To completely constrain the drum, a Z-translation constraint was applied to the front line, a Y-translation

constraint was applied to the top line, and an X-translation was applied to the back line. The translator tip was then constrained in both the X and Z directions to allow movement following the application of the load.

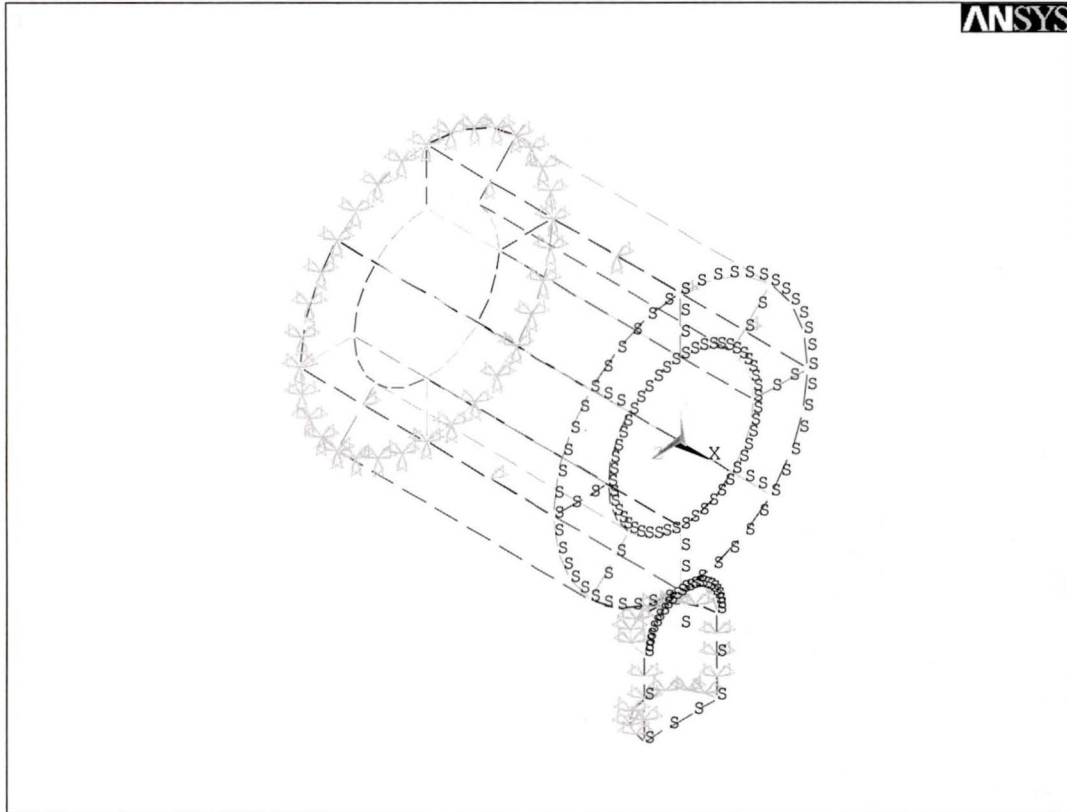


Figure 4.22: Model constraints

4.2.4.4.3 Loads

The piezoelectric translator to be used in the device has a prestress force of approximately 2000N, a compressive stiffness (C_T) of 200 N/ μm , and a maximum unloaded stroke (ΔL_0) of 95 μm at +1000V. However, the recharging amplifier is only capable of +500V. Assuming a linear relationship (as presented in Chapter 3), the

maximum free stroke of the translator is $47.5\mu\text{m}$. The maximum blocking force the translator can generate depends on its stiffness and expansion capabilities and can be expressed as:

$$F_{MAX} = C_T \Delta L_O = (200 \text{ N}/\mu\text{m})(47.5\mu\text{m}) = 9500 \text{ N}$$

As introduced in Chapter 3, the blocking force of an industrial piezoactuator becomes smaller as the crystal stack expands. The value of 9500N corresponds to a zero displacement. However, 9500N was used for the original reaction force in the model and the maximum displacement of $47.5 \mu\text{m}$ was used as well. As expected, these values produced erroneous result but as the new values were used for the second run, the model began to quickly converge towards a solution.

The maximum expansion of the translator against external elastic body depends on the actuator's stiffness, the resulting reaction force pushing against it, and the maximum unloaded stroke of the translator. A value of 5000N for the reaction force produced the correct results.

$$\Delta L = \Delta L_O - \frac{F_{TOTAL}}{C_T} = \Delta L_O - \frac{F - F_{PRELOAD}}{C_T} = 47.5\mu\text{m} - \frac{5000\text{N} - 2000\text{N}}{200 \text{ N}/\mu\text{m}} = 32.5\mu\text{m}$$

A constant uniform pressure was applied to the bottom surface of the translator tip to replicate the force generated by the piezoelectric actuator as shown in Figure 4.23. The calculated pressure is as follows:

$$x = \frac{F}{\pi R^2} = \frac{5000\text{N}}{\pi(0.005\text{m})^2} = 63.662 \text{ MPa}$$

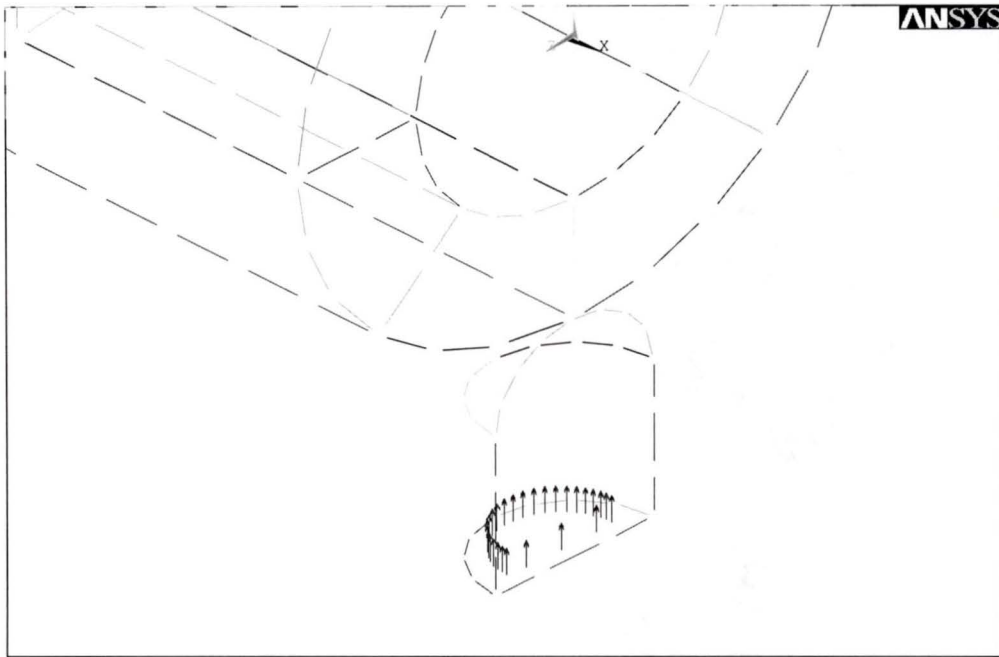


Figure 4.23: Pressure loads

4.2.4.4.4 Results

The results generated by Ansys indicated that $\Sigma F_x \approx 0$, $\Sigma F_y \approx 0$, and $\Sigma F_z \approx 0$. This confirms equilibrium and indicates that the results are relevant. The pressure load of 63.662 MPa resulted in a translator displacement of 32.15 μm and a contact point displacement of 15.77 μm . The relevant nodes, their locations, and their displacements are shown in Table 4.1.

Table 4.1: Displacement results

Keypoint	Node	Y Location [m]	ΔY [m]
21	607	-0.0175	1.5765E-05
35	1	-0.0225	2.9828E-05
42	4	-0.0325	3.2149E-05

As the translator displacement of 32.15 μm is close to the calculated displacement of 32.5 μm , the assumed drum reaction force of 5000N is valid. The deformation results, the translator cylinder deformation in particular, are of interest because they show that although the actuator stack expands 32.5 μm , the actual displacement at the point of contact is only 15.77 μm . The 16.73 μm loss is due to actuator tip deformation and indentation of the steel drum.

As the contact point moved 1.577 μm when a 5000 N force was applied, the drum's spring constant in the vertical direction is:

$$c_s = \frac{F}{x} = \frac{5000N}{1.577 \times 10^{-6}} = 3.172 \times 10^9 \text{ N/m}$$

The amount of force transmitted from the translator to the front line of the drum is of great interest as it is this force used to control the device. The force is determined by summing the Z-direction nodal forces of the front line of the drum. The seventeen nodes, their locations, and their reaction forces are listed in Table 4.2.

Table 4.2: Contact line force results

Keypoint	Node	X[m]	Y[m]	Z[m]	FZ [N]
29	615	0	-3.054E-12	1.750E-02	-57.783
-	966	-2.22E-03	-3.05E-12	1.75E-02	-167.100
-	965	-4.43E-03	-3.05E-12	1.75E-02	-99.152
-	964	-6.65E-03	-3.05E-12	1.75E-02	-162.360

-	963	-8.86E-03	-3.05E-12	1.75E-02	-85.382
-	962	-1.11E-02	-3.05E-12	1.75E-02	-123.850
-	961	-1.33E-02	-3.05E-12	1.75E-02	-79.447
-	960	-1.55E-02	-3.05E-12	1.75E-02	-104.720
-	959	-1.77E-02	-3.05E-12	1.75E-02	-48.499
-	958	-1.99E-02	-3.05E-12	1.75E-02	-59.821
-	957	-2.22E-02	-3.05E-12	1.75E-02	-32.015
-	956	-2.44E-02	-3.05E-12	1.75E-02	-36.989
-	955	-2.66E-02	-3.05E-12	1.75E-02	-16.439
-	954	-2.87E-02	-3.05E-12	1.75E-02	-20.720
-	953	-3.08E-02	-3.05E-12	1.75E-02	-7.990
-	952	-3.29E-02	-3.05E-12	1.75E-02	-9.469
28	614	-3.50E-02	-3.05E-12	1.75E-02	-1.138
				Totals	-1112.9

The force calculations are doubled to account for the other half of the model resulting in a total force of 2225.8N in the Z direction. The incremental force value at the center of each FEA ten-node tetrahedral element along the line of contact is plotted on Figure 4.24. The dark line on Figure 4.24 represents polynomial extrapolation of the results along the half-drum. The maximum force occurs at the middle of the drum and decreases towards the ends. Although a larger number of nodes would assist in the evaluation, the processing time becomes excessive before an appreciable difference is noticed. To further fine-tune the process, it is necessary to obtain a commercial version of the FEA software that does not have element number restrictions.

Reaction Force vs. X-Location

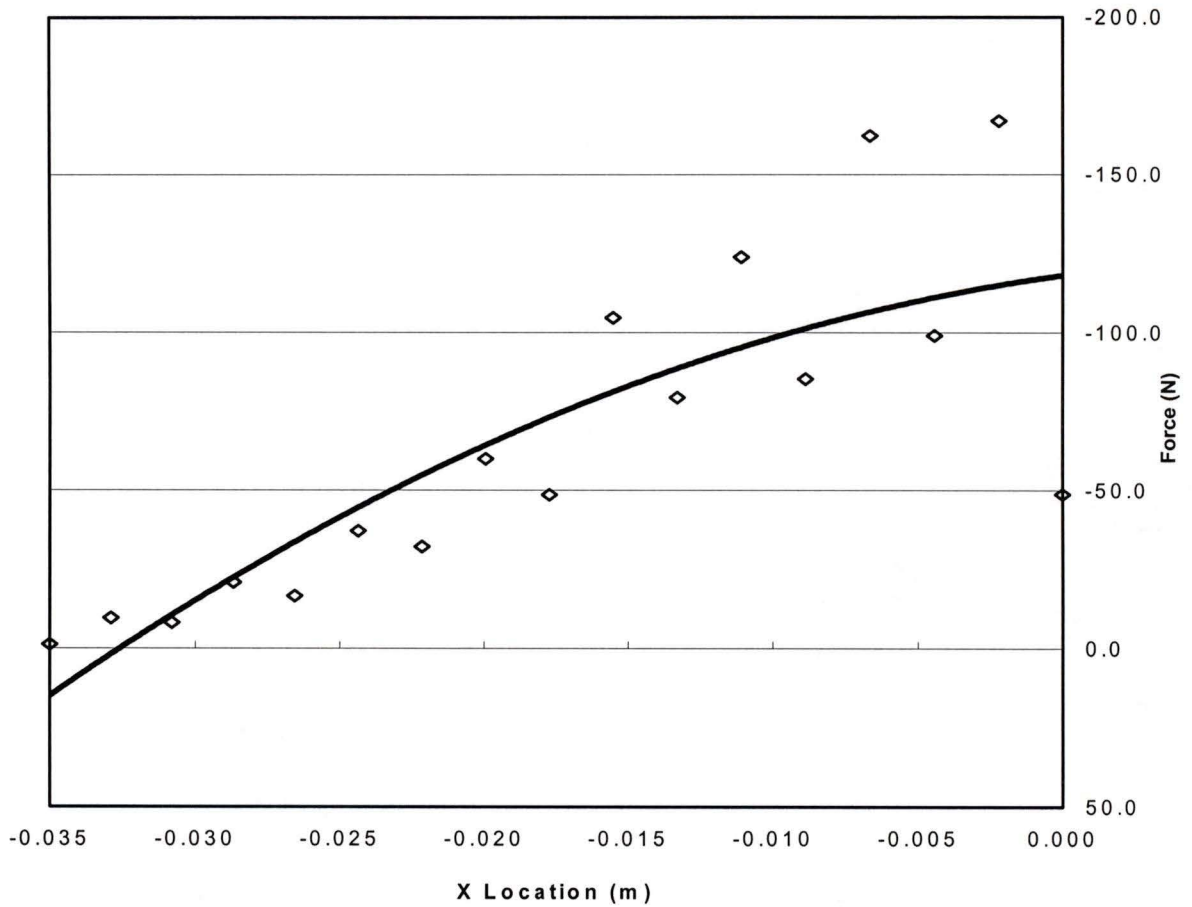


Figure 4.24: Half-drum reaction force distribution

The force transmission ratio is then:

$$T_f = 2225.8/5000 = 0.445$$

The model presented in this section accurately estimates the force transfer through the drum and verifies that the use of the drum spring element is suitable for the design.

4.2.4.5 Control Electronics

The control electronics used with the chatter suppression tool is a Real-Time National Instruments DAQ board with LabView software interface. The block diagram of the system is shown in Figure 4.25. Up to four sensors can be simultaneously connected to the LIVM conditioning unit that produces analogue output signal within -5V to +5V range. The piezoactuator amplifier is controlled by an analogue signal that ranges between 0V to +10V.

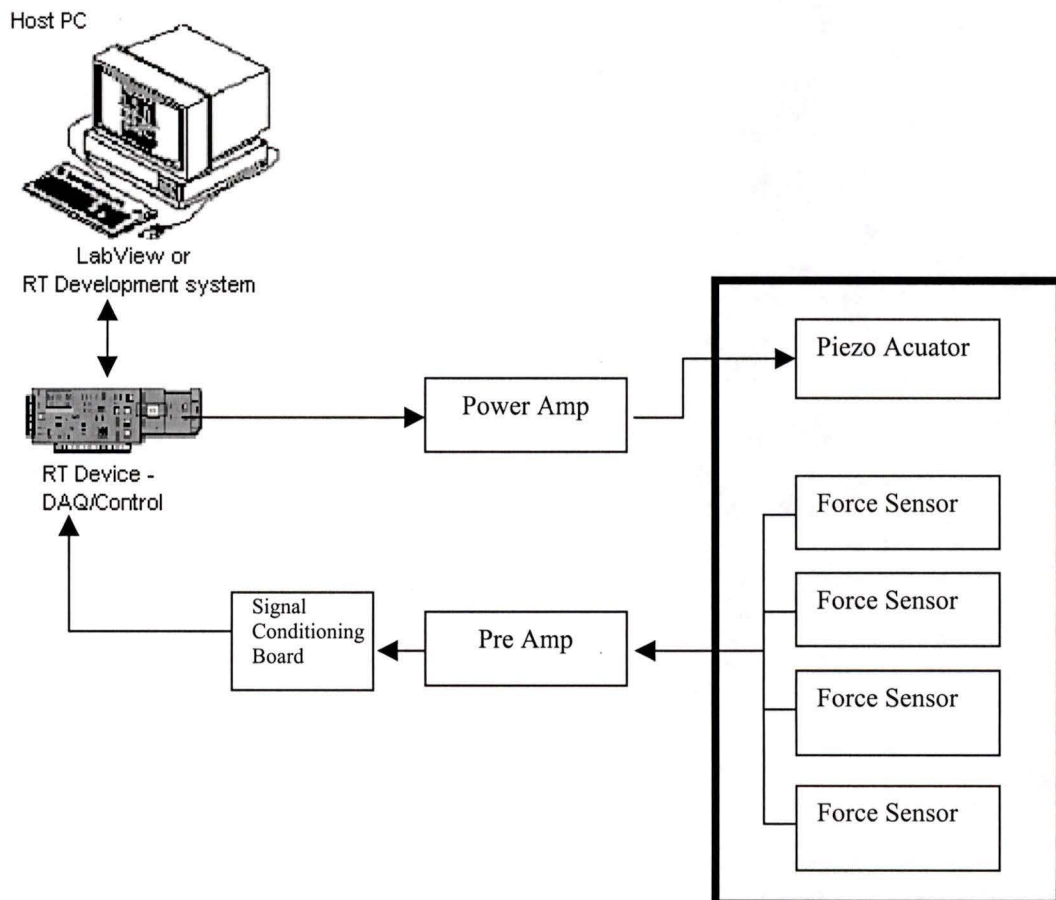


Figure 4.25: Control electronics block diagram

The purpose of the Signal Conditioning board is to increase the sensitivity resolution for the signals from the force sensors. It consists of four operational amplifiers providing 20 times amplification that is directly fed into the Data Acquisition (DAQ) Board. The National Instruments RT Series data acquisition board consists of a processor board and data acquisition board.

The processor board is part # NI 7030 featuring:

- Independent 32-bit, AMD 486DX5 processor running at 133MHz.
- 8MB user programmable RAM
- 16KB on-chip cache and 256KB L2 cache.
- The real time operating system running on the board provides an environment for applications written with LabView Real-Time to be executed independently on the board. The 7030 board is ideal for running time critical control applications.

When real-time control is implemented, it is preferable to run the control algorithm on the RT device (NI 7030) independently of the host computer. In such a case, the host PC is used solely for the purpose of displaying and manipulating the data. LabView and the real-time operating system running on the 7030 board provide communication between the board and the host PC by the means of TCP/IP. In addition, for some real-time applications, both the board CPU and the host PC can use the 1KB on-board shared memory.

The DAQ board on the NI 7030/6040E RT device is NI 6040E. The NI 6040E features:

- 16 single-ended or 8 differential input analog inputs.
- 12-bit ADC resolution with sampling rate up to 500kS/s (kilo samples per second). $\pm 0.05\text{V}$ to $\pm 10\text{V}$.
- 2 analog outputs with 12-bit resolution, output rate of 1MS/s and output range $\pm 10\text{V}$.
- 8 digital I/O channels.

The chatter suppression tool uses four analog inputs each connected to one of the signals coming from the four force sensors. They are configured as single-ended with working range of $\pm 10\text{V}$. For the control signal one of the analog output is used. The output is configured to work in the range 0-10V. The control algorithms and display are implemented with the LabView graphical programming language. LabView uses icons to create an application. LabView programs are called Virtual Instruments (Vis) because their appearance and operation imitate physical instruments, such as oscilloscopes and multimeters.

4.2.5 Testing

The tool was assembled and its resonance frequency was measured with a frequency analyzer for several preload values. In addition, the tool's dynamic response was measured for actuator frequency bandwidths of 0Hz to 800Hz. The device was then mounted on a testbed for further studies. Unfortunately, the tool holder proved to be too stiff and the small cutting forces that the test machine could produce were not large

enough to cause chatter effects in the device. Faced with a choice of reducing the stiffness of the tool by grinding the drum thinner or attempting to acquire a larger industrial lathe for the experiment, the first option was the natural choice.

4.2.5.1 Tool Holder Dynamic Characteristics

The final version of the assembled tool holder is shown in Figure 4.26. A hammer test was used to measure the natural frequency of the assembly in the direction of the cutting force. The sensor was connected to a HP frequency analyzer and the tip of the tool holder was tapped with a hammer.

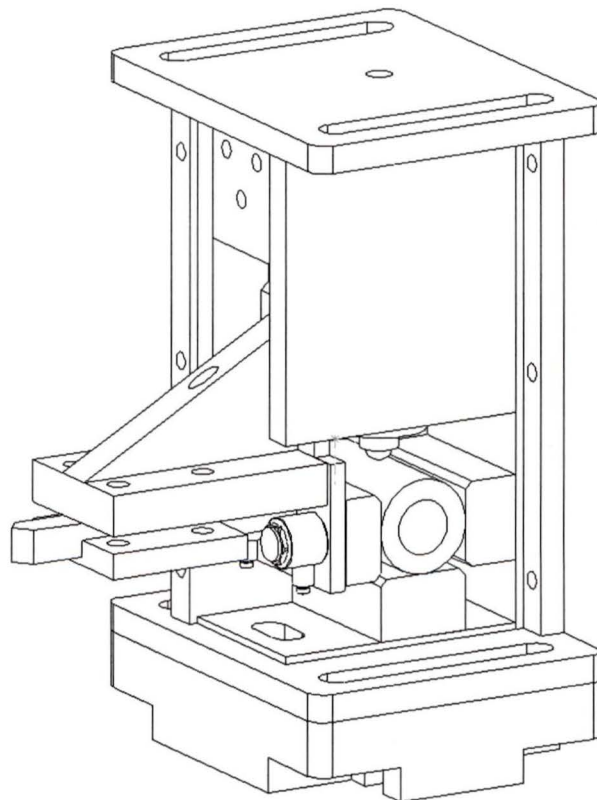


Figure 4.26: Final tool assembly

The natural frequency of the device is directly proportional to the device's internal preload force, i.e. the higher the preload, the higher the natural frequency of the device. Figures 4.27 and 4.28 show the natural frequency results for preloads of 750N and 1000N

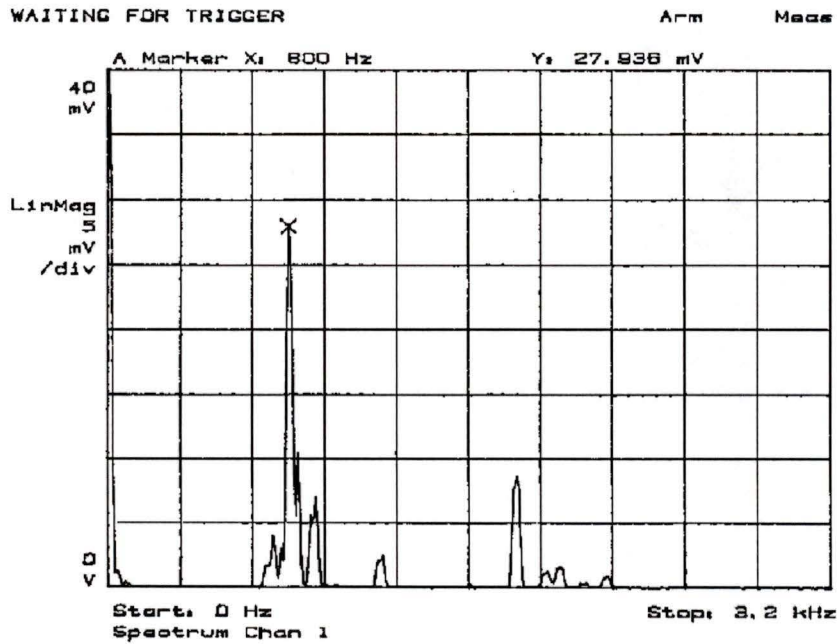


Figure 4.27: Resonance frequency characteristics (750N preload)

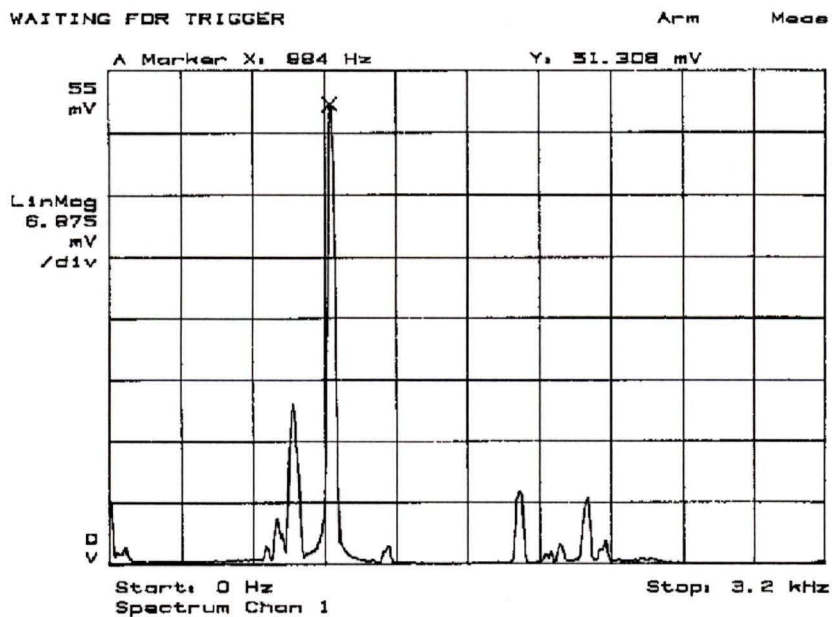


Figure 4.28: Resonance frequency characteristics (1000N preload)

It was observed that, depending on the system preload, the dominant natural frequency of the chatter suppression device is in the range of [750,1000] Hz. Such results allow for stable dynamic control in the 0-700 Hz bandwidth range of piezoactuator switching.

The force transferred from the piezoactuator to the tip of the tool was measured within a frequency range of 0-900 Hz at 750N preload. The measured force amplitudes are plotted in Figures 4.29.

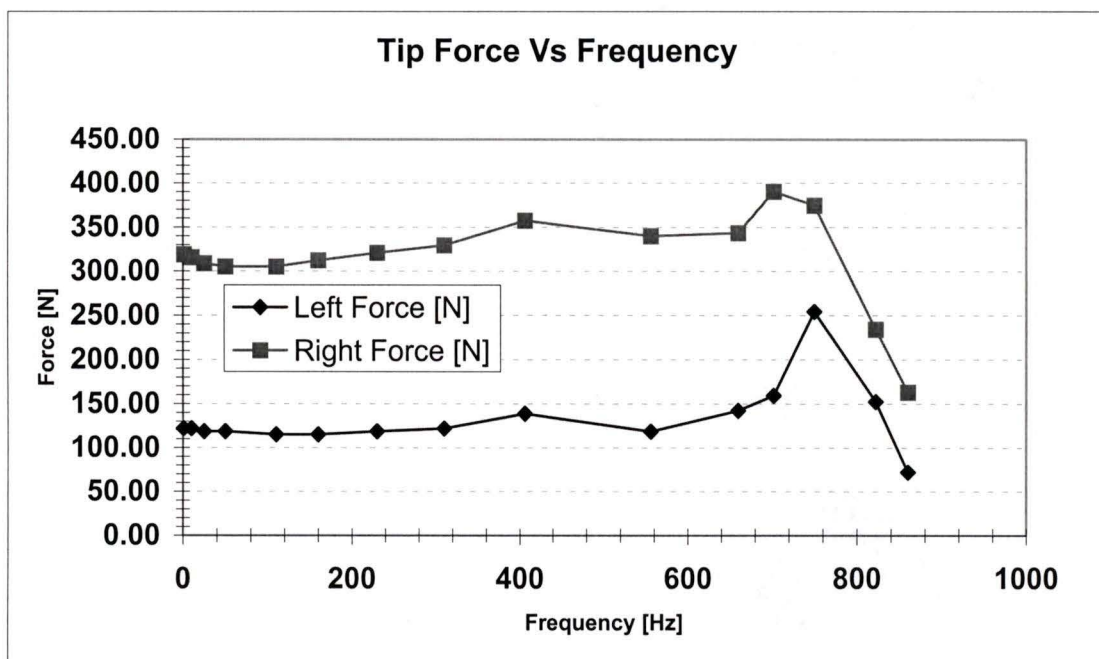


Figure 4.29: Tool-sensor dynamic response (750N preload)

Figure 4.29 demonstrates that the responses from both sensors follow the same curve but the readings from the right sensor are 2.33 time greater than the readings from the left sensor. This ratio is consistent over the experimental frequency range and clearly indicates a misalignment of the internal components of the device. As expected from the natural frequency tests, resonance occurs at around 750 Hz. Prior to the resonance frequency, the force at the tip of the tool is virtually unaffected and represents

sinusoidal oscillations above the preload force with combined amplitude of 500N as shown in Figure 4.30.

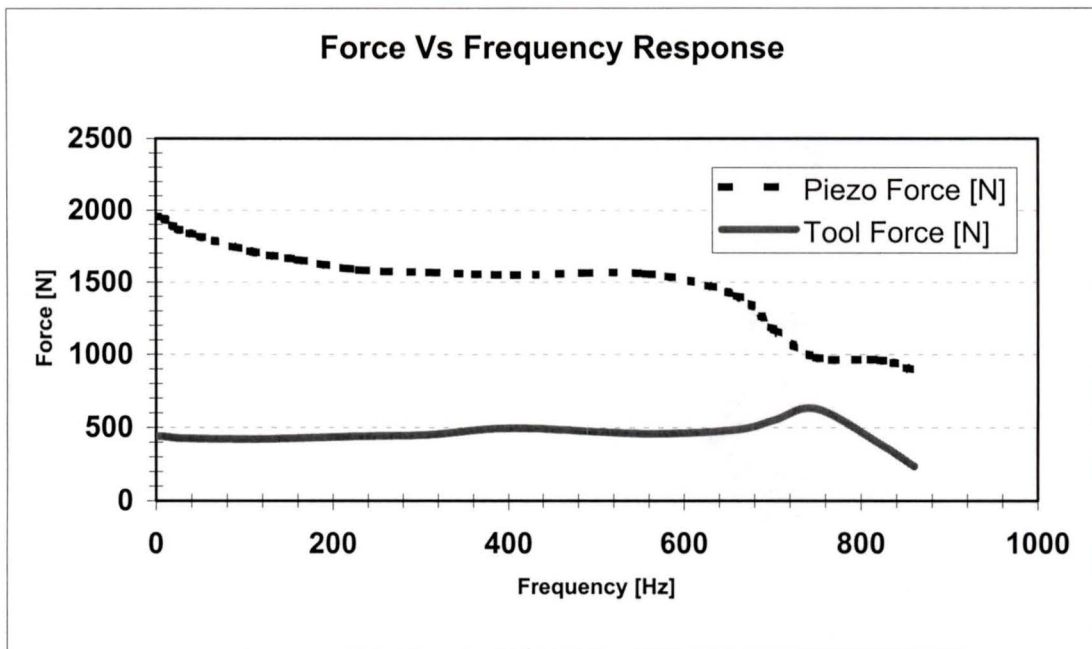


Figure 4.30: Tool-sensor and actuator-sensor dynamic force response (750N preload)

Around the resonance frequency, the actuator force causes strong vibrations of the entire assembly. Figure 4.30 shows a dip in the actuator force and an increase of the total force on the tip of the tool.

The force transmission ratio was calculated for the measured range of frequencies and is shown on Figure 4.31. The measured transmission ratio is in the range of 0.23 to 0.3 in the 0 Hz to 700 Hz range. This changes noticeably in the resonance range of the assembly where the transmission ratio increases dramatically. However, the most likely cause of this increase is modal vibration coupling and since it is outside the operational range of the device, the increase has no practical significance. The predicted force transmission ratio in Section 4.2.4.4.5 is 0.445, which is higher than the measured transmission ratios.

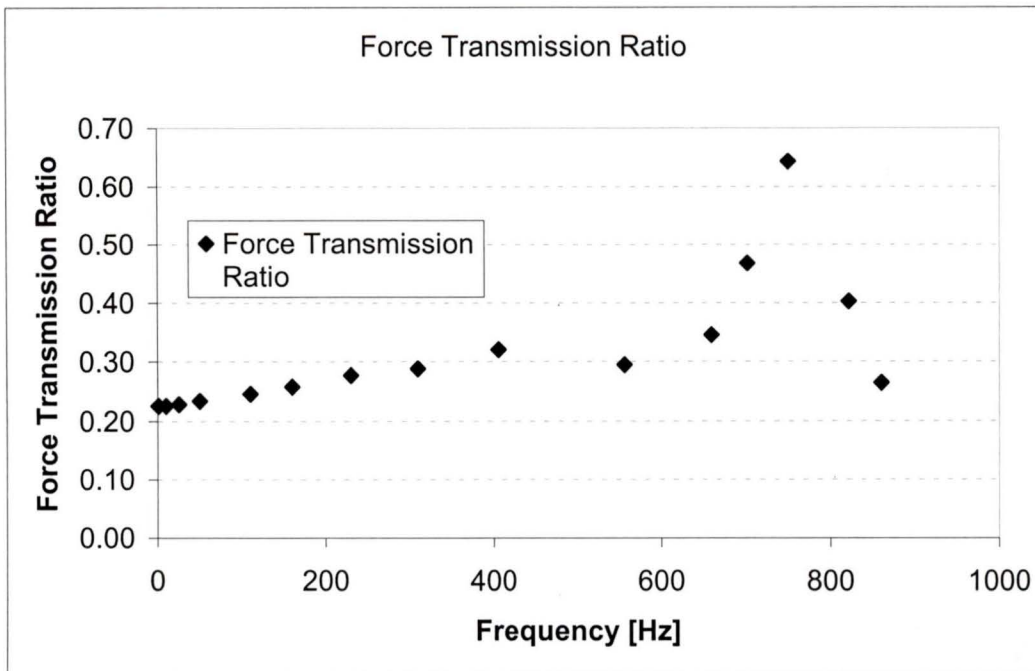


Figure 4.31: Force transmission ratio

The difference of almost 78% is most likely caused by elastic deformations in the assembly that additionally reduce the effectiveness of the translator. Indeed, the high pushing force produced by the actuator causes a permanent plastic deformation imprint of the steel-ball tip of the actuator onto the drum.

4.2.5.2 Machine Testing

A combination mill/lathe is utilized as the testbed for the chatter suppression device. The machine used for the experiments is ShopTask Shopmaster 2000 as illustrated in Figure 4.32. Despite its small size, the machine has been produced for over 20 years and performs satisfactorily during many machining operations. Unfortunately, the ShopTask Shopmaster 2000 has relatively low stiffness and, although the manufacturer claims that it can cut steel, it is primarily designed for machining plastics and soft

metals. During steel cutting, the machine vibrates heavily and it was decided to proceed with an aluminum workpiece for the experiments.

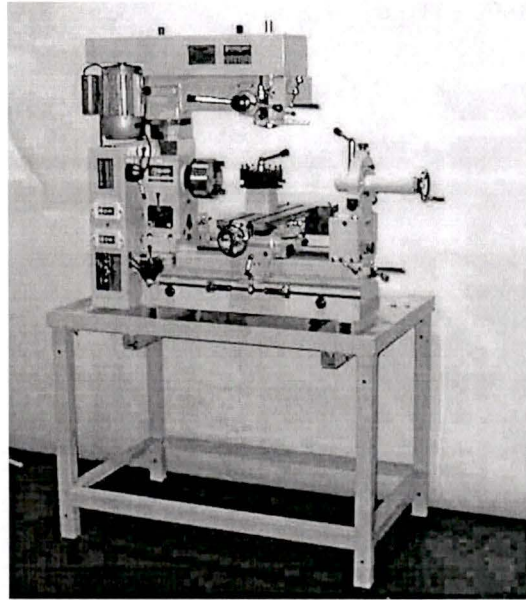


Figure 4.32: ShopTask Shopmaster 2000

The chatter suppression device was installed on the testbed as illustrated in Figure 4.33. The assembly mounts effortlessly and, as designed, the tool tip touches the workpiece at the centerline.

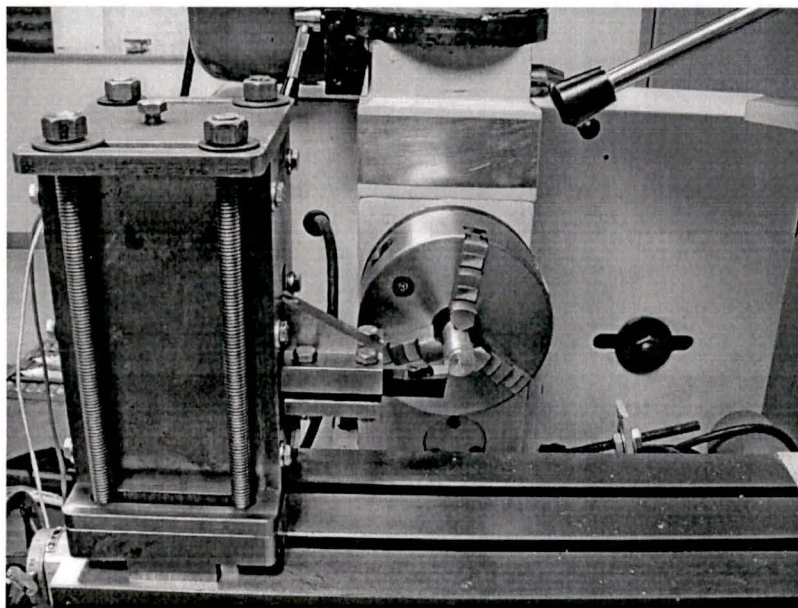


Figure 4.33: Tool installation

metals. During steel cutting, the machine vibrates heavily and it was decided to proceed with an aluminum workpiece for the experiments.

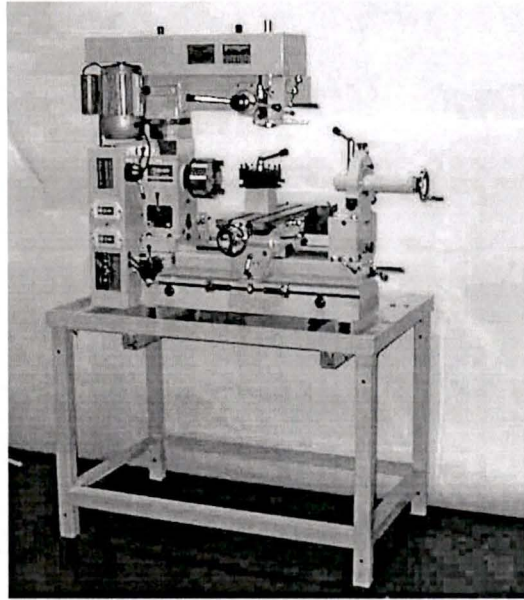


Figure 4.32: ShopTask Shopmaster 2000

The chatter suppression device was installed on the testbed as illustrated in Figure 4.33. The assembly mounts effortlessly and, as designed, the tool tip touches the workpiece at the centerline.

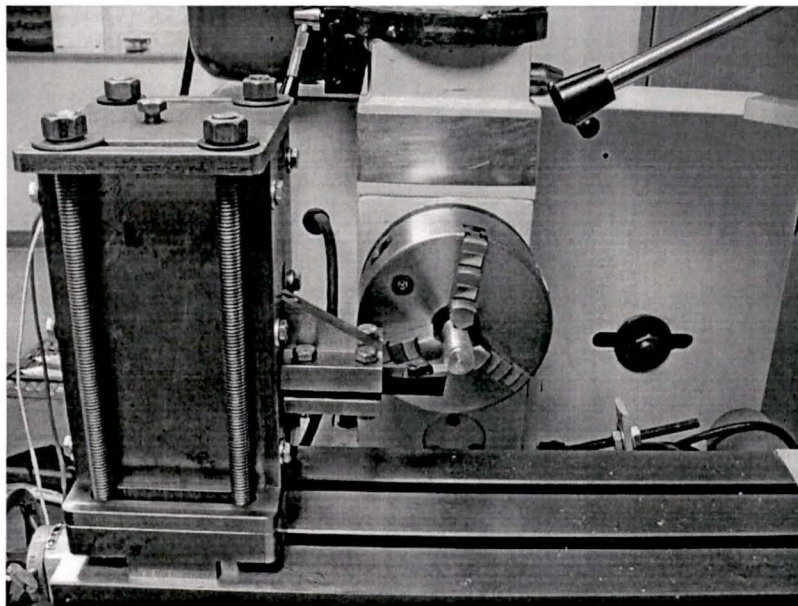


Figure 4.33: Tool installation

A series of cuts were made on a 1" diameter aluminum workpiece as shown in Figure 4.34. In all cases the tool performed as designed and the cuts were smooth.

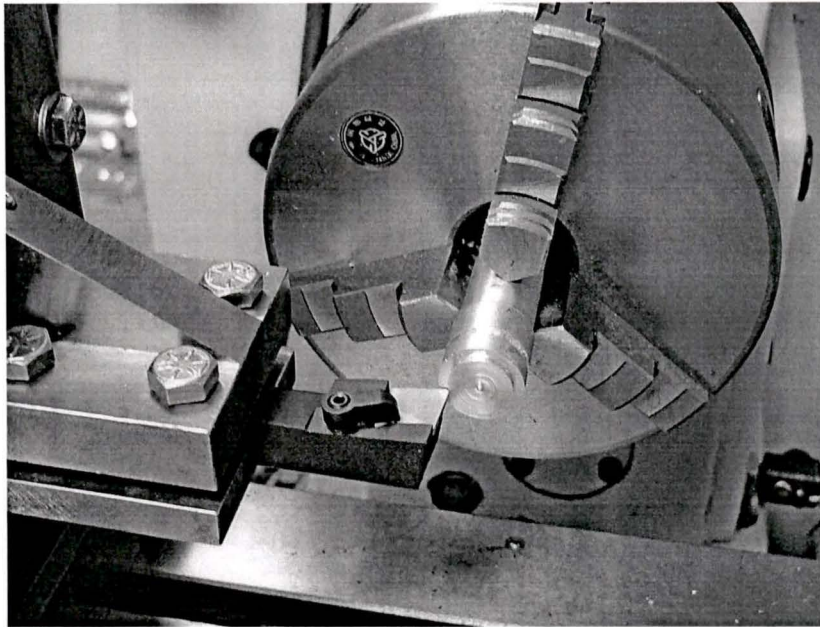


Figure 4.34: Experimental workpiece

The experiments performed with the tool indicate that the tool has reasonable dynamic characteristics within a bandwidth of 750Hz. Unfortunately, the device was originally designed for cutting steel with high cutting forces. The preload of the tool-holder was around 750N during the experiments but the cutting forces in aluminum machining are substantially lower. There are two ways of overcoming this problem: reducing the stiffness of the device by reducing the stiffness of the drum, or using a large industrial machine for the experiments. Large industrial machines are expensive and purchasing one for the purpose of this research is not feasible both from financial and from space availability viewpoints. The following section presents the modifications done to the tool that make it a feasible platform for further experimentation of chatter suppression control strategies.

4.2.6 Improvements and Fine-tuning

The most significant problems encountered during the initial experimentation with the newly designed tool holder were:

- The two front sensors were not reading equal forces.
- The tool was designed for preloads that are substantially greater than the cutting forces tolerated by the testbed.
- It was originally believed that three sensors would be sufficient for future deployment of various control strategies. However, a need for adding a fourth sensor was identified.
- Metal cutting and chatter vibrations experiment could be very dangerous and early-stage experiments with real cutting tools are not desirable. To fully understand the effects of various control strategies, it is necessary to rearrange the device in a more experiment-friendly manner.

The difference in the force reading of the front sensors was caused by a slight offset from parallel between the flat spring and the piezoholder (See Figure 4.17). Although the difference was less than 0.002", it was sufficient to cause a twist in the assembly. As a result, one of the force sensors was touching the housing before the other and thus was exhibiting greater loading. This problem was corrected fairly quickly.

Since acquiring a large machine was not feasible, it was decided that the internal stiffness of the drum spring had to be reduced by decreasing its thickness. Several new drums with various thickness were built. As expected, the thinner the drum, the lower the minimum achievable preload. For example, a drum of thickness 1/16" produces about 500N preload. In the future, if lower experimental forces are required, it is possible to make less stiff drums from other than steel materials.

It is believed that a fourth sensor located at the back of the drum will give an extra reading that can be valuable for implementing various control strategies. The back drum support was machined to accommodate a fourth sensor.

Finally, an experimental tool was designed for the purpose of further studying the performance of the device and for researching various control deployments. The tool is shown on Figure 4.35.

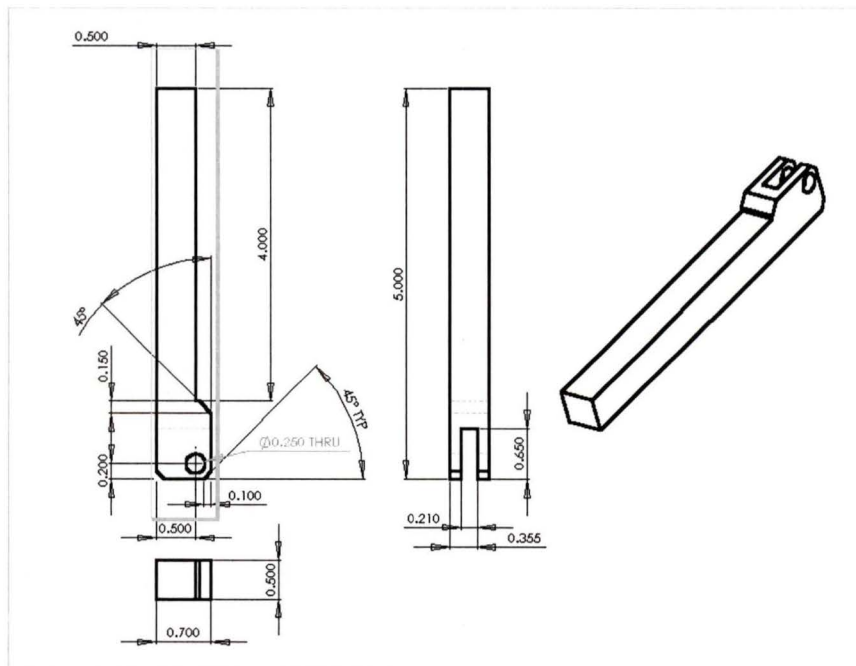


Figure 4.35: Experimental tool

The experimental tool has a ball bearing mounted at the front. The ball bearing allows force readings to be collected without actual destruction of the workpiece. With this arrangement, it is possible to make future experiments that are based on workpieces of various surface profiles.

Chapter 5

Conclusions and

Recommendations for Future Development

This work confirms the feasibility of using piezoelectric sensors and actuators for designing machine-chatter suppression devices that can operate within practical frequency bandwidths. The innovative approach of installing the piezoelectric actuator in series with the active element, rather than the traditional shunted configuration, proved to be capable of delivering the desired dynamic characteristics necessary for implementing future chatter suppressing control strategies.

The device presented in this thesis employs a piezoelectric translator acting upon a drum. The design allows for two modes of operation that are functionally separated by a preset internal preload. The first mode of operation is passive and, for as long as the system sensors register contact and the cutting forces remain steady, no active control is attempted. When the original preload is overcome by the presence of a large external cutting force, the device reacts in a way that counter-acts and stabilizes the external disturbance. A crucial step in implementing the proposed design was selecting the active elements and the passive elements to be used in the system. During this process, it was found necessary to implement Finite Elements Analysis modeling for calculating the stiffness of the novel drum spring. The FEA modeling resulted in predicted actuator displacement of $32.15 \mu\text{m}$ caused by a 5000N translation force. This corresponded to

total transmitted force to the tip of the tool of 2225.8N at a transmission ratio of 0.445 and a drum stiffness of 3.172×10^9 N/m.

The device was manufactured and assembled for testing at the Advanced Control and Instrumentation Laboratory in Victoria, BC. A Hammer test and an HP frequency analyzer were used to measure the natural frequency of the assembly in the direction of the cutting force. This test indicated a natural frequency dependency on the system preload and a natural frequency range of 750 Hz to 1000 Hz. The system was found suitable for dynamic control applications within a [0,700] Hz bandwidth. Dynamic tests of the device indicated satisfactory output force characteristics with rapid force degradation outside the upper bandwidth boundary. The measured force transmission ratio was between 0.23 and 0.30. This ratio was about 76% lower than the predicted force transmission ratio of 0.445. The reason for that is unaccounted internal elastic deformations that reduce the effectiveness of the translator.

Finally, the system's control electronics were integrated with the device. A Real-Time National Instruments DAQ board with LabView software interface provides the platform for future implementation of various control strategies. The assembly was tested with a ShopTask Shopmaster 2000 combination mill/lathe. Unfortunately, it was concluded that the test machine was not capable of operating at the high cutting forces that the tool was designed for. The tool was only tested with aluminum workpieces and the performance was satisfactory.

This thesis presents only the design of an integrated platform for future experimentation with chatter suppression control strategies. This work is only a small part of a large

project and several areas remain open for future development that can be summarized with:

- The tool was originally designed with high-speed steel cutting in mind. This requires high stiffness of the internal elements and large preload forces. This is not feasible for experimental studying of chatter vibrations control algorithms and, therefore, the stiffness of the device has to be reduced.
- The proposed device has a transmission ratio that is smaller than the expected force transmission ratio. This discrepancy can be reduced with design optimization and the use of high-grade materials.
- As the design evolves, new piezoelectric force sensors and a new piezoelectric actuator can be selected for optimal performance.
- The design can be evaluated for bending and twisting so additional reinforcements can be installed if necessary.
- It is possible to optimize the overall design and achieve partial miniaturization.

References

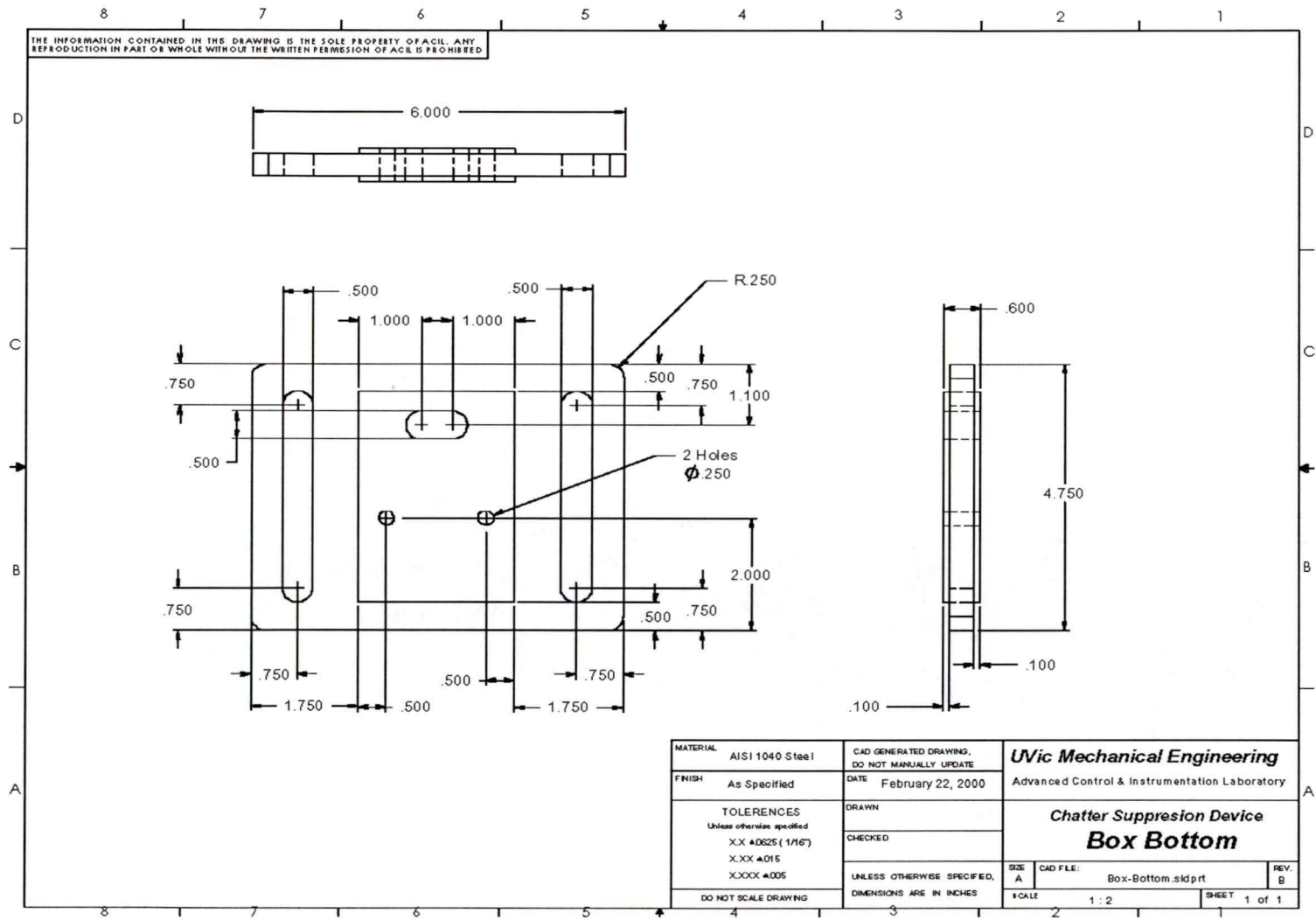
1. Altintas Y., "Modeling Approaches and Software for Predicting the Performance of Milling Operations at MAL- UBC", *Manufacturing Automation Laboratory*, University of British Columbia, 1997, Canada.
2. Altintas Y., "Principals of Metal Cutting and Machine Tool Automation", *Manufacturing Automation Laboratory*, University of British Columbia, 1997, Canada.
3. Anderson et al, "Integrated Electromechanical Devices for Active Control of Vibration and Sound", *International Mechanical Engineering Congress and Exposition*, Dallas, Texas, November 16-21, 1997
4. Ashley S., "Smart Ski and Other Adaptive Structures", *Mechanical Engineering*, Vol. 117, November 1995.
5. Auerbach J., "A Smarter Ski is Ready to Speed You Downhill", *The Boston Globe*, December 6, 1995.
6. Benning et al, "Active Control of Mechanical Vibrations" *Bell Labs Technical Journal*, Lucent Technologies, Spring 1997
7. Craig J., *Introductions to Robotics Mechanics and Controls*, Addison-Wesley Publishing Company, Massachusetts, 1989.

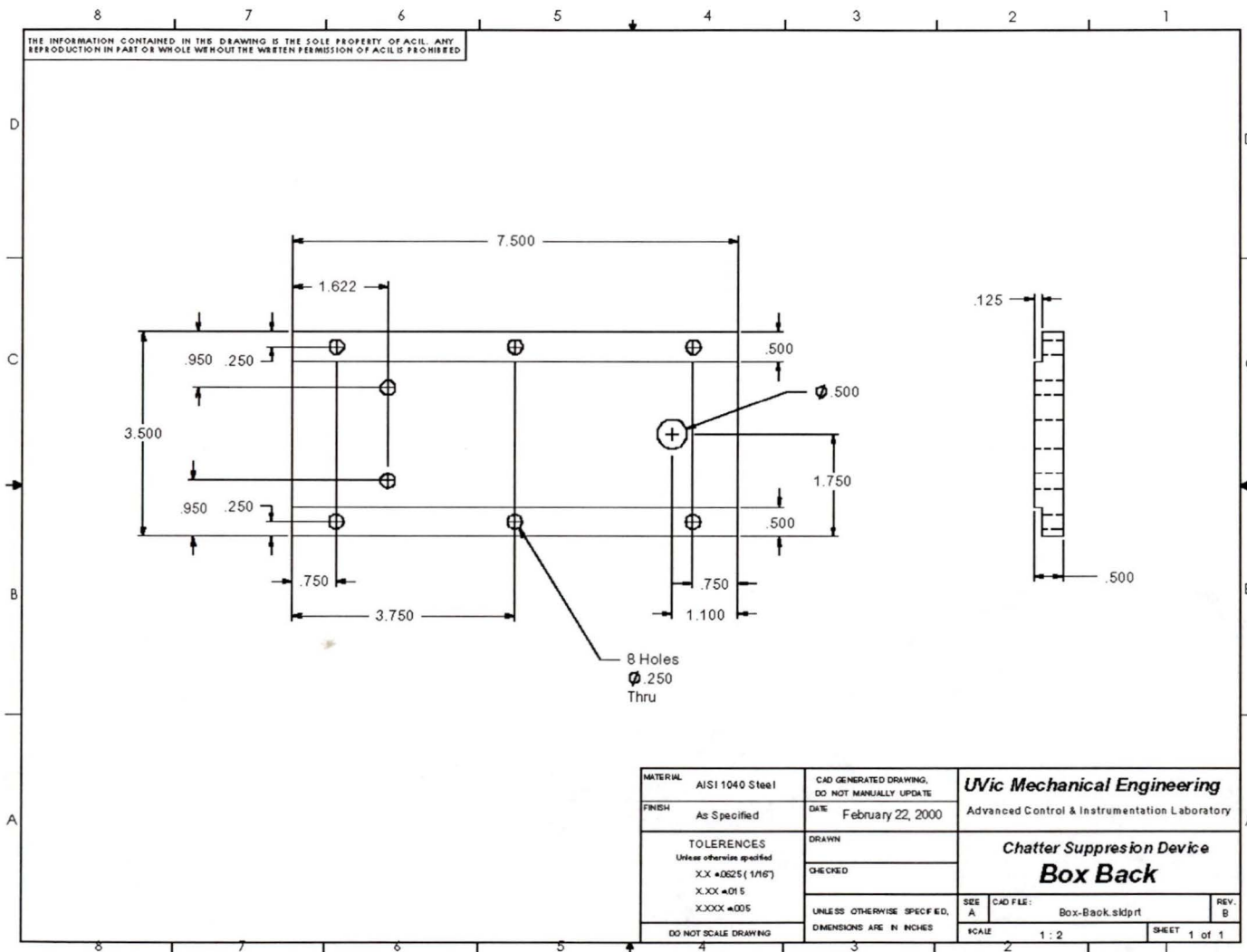
8. Dytran Instruments Inc., *General Catalog & Instrumentation Handbook*, Chatsworth, 1998.
9. El-Lakany H., *An Experimental and Theoretical Study on Piezoelectric Ceramic Processing*, University of Victoria, Victoria.1996.
10. Eringen A., *Continuum Physics*, Academic Press, New York, 1975.
11. Hinnerics et al, "Vibration Control for Precision Manufacturing at Sandia National Laboratories", *Smart Structures and Materials*, March 1995, SPIE Volume 2447
12. Jaffe B. et al., *Piezoelectric Ceramics*, Academic Press Limited, 1971.
13. Jaffe B., *Piezoelectric Ceramics*, R.A.N. Publishers, Marietta.1974.
14. Kenji U., "Electrostrictive Actuators: Materials and Applications", *The American Institute of Physics*, New York, 1992.
15. Kenji U., "Piezoelectric Ceramics", *Key Papers in Physics*, The American Institute of Physics, New York.1992.
16. Maugin A., *Continuum Mechanics of Electromagnetic Solids*, North-Holland, Amsterdam, 1987.

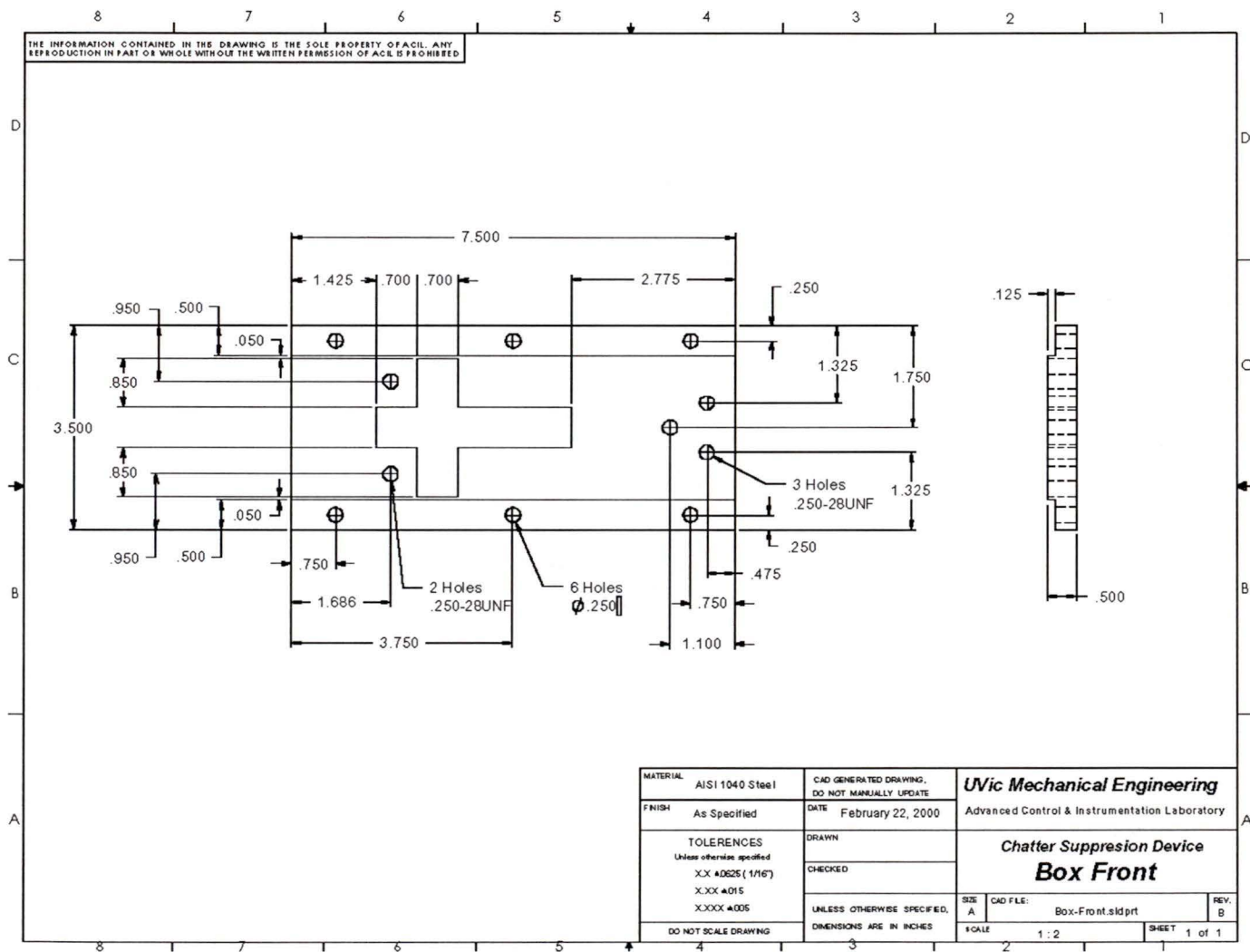
17. PCB Piezotronics, *General Piezoelectric Theory*, Depew, New York, 2000.
18. Physik Instrumente (PI), *Product Catalogue*, Germany, 1998.
19. Pickelmann L., *Piezoelectrical and Electrostrictive Stack Actuators*, Piezomechanik GmbH, Munich, 2001
20. Ping G. et al., "Tracking Control of Piezoceramic Actuator", *IEEE Transactions on Control Systems Technology*, Vol. 4, No. 3, May 1996.
21. Radford N., *Bayesian Learning for Neural Networks*, Springer, New York, 1996.
22. Regelbrugge et al, "Canceling Vibrations with Smart Materials: a Case Study", *Smart Structures and Materials*, March 1995, SPIE Volume 2447
23. Smith F., *Principles of Material Science and Engineering*, McGraw-Hill Inc, New York, 1990.
24. Tetsuro Takana, "Piezoelectric Devices in Japan", *The American Institute of Physics*, New York, 1992.
25. Versteijhe et al, "Hybrid force-position control of clamping with a piezo-stepper", *IEEE Control Systems Magazine*, Vol. 19(2), 1999.

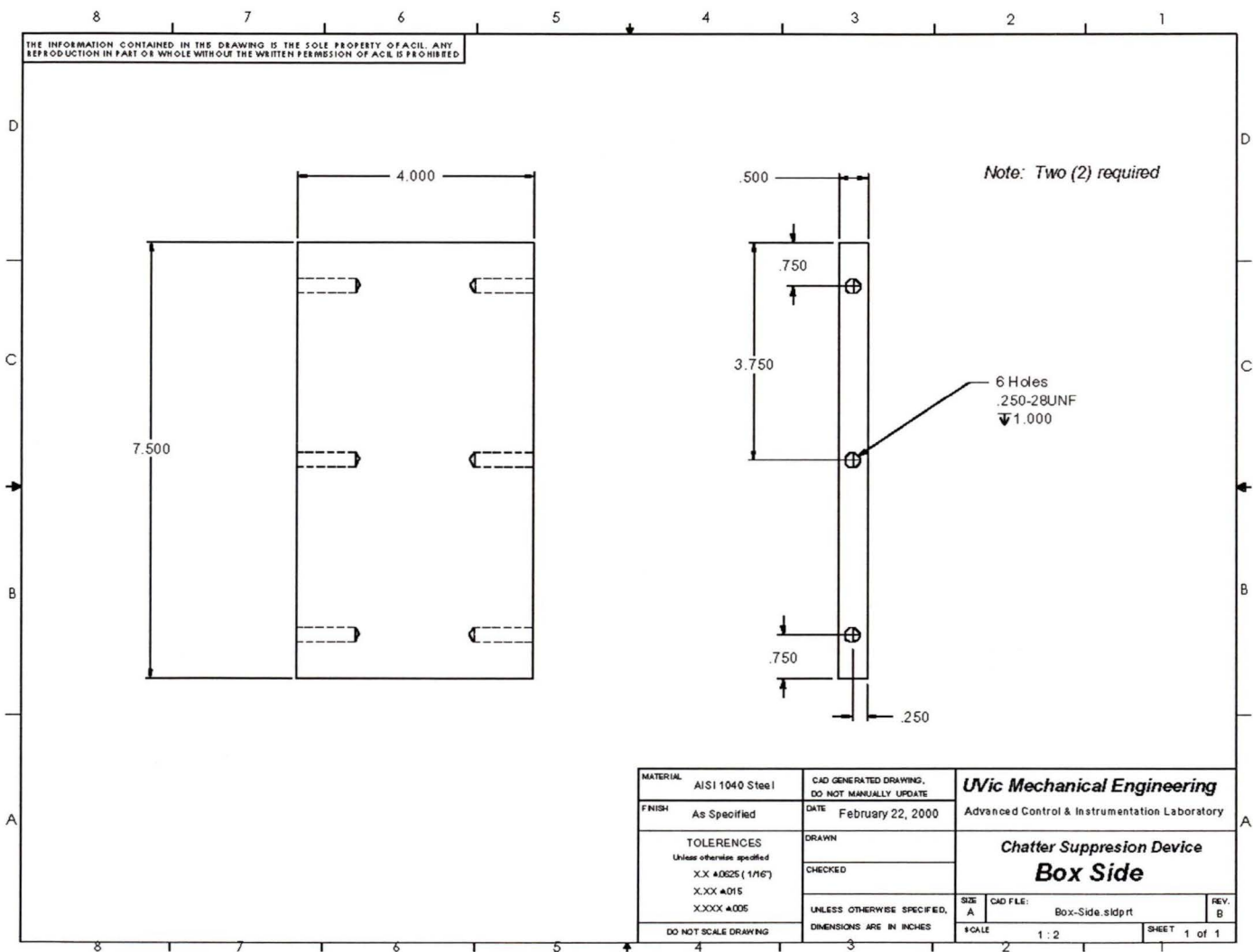
Appendix A

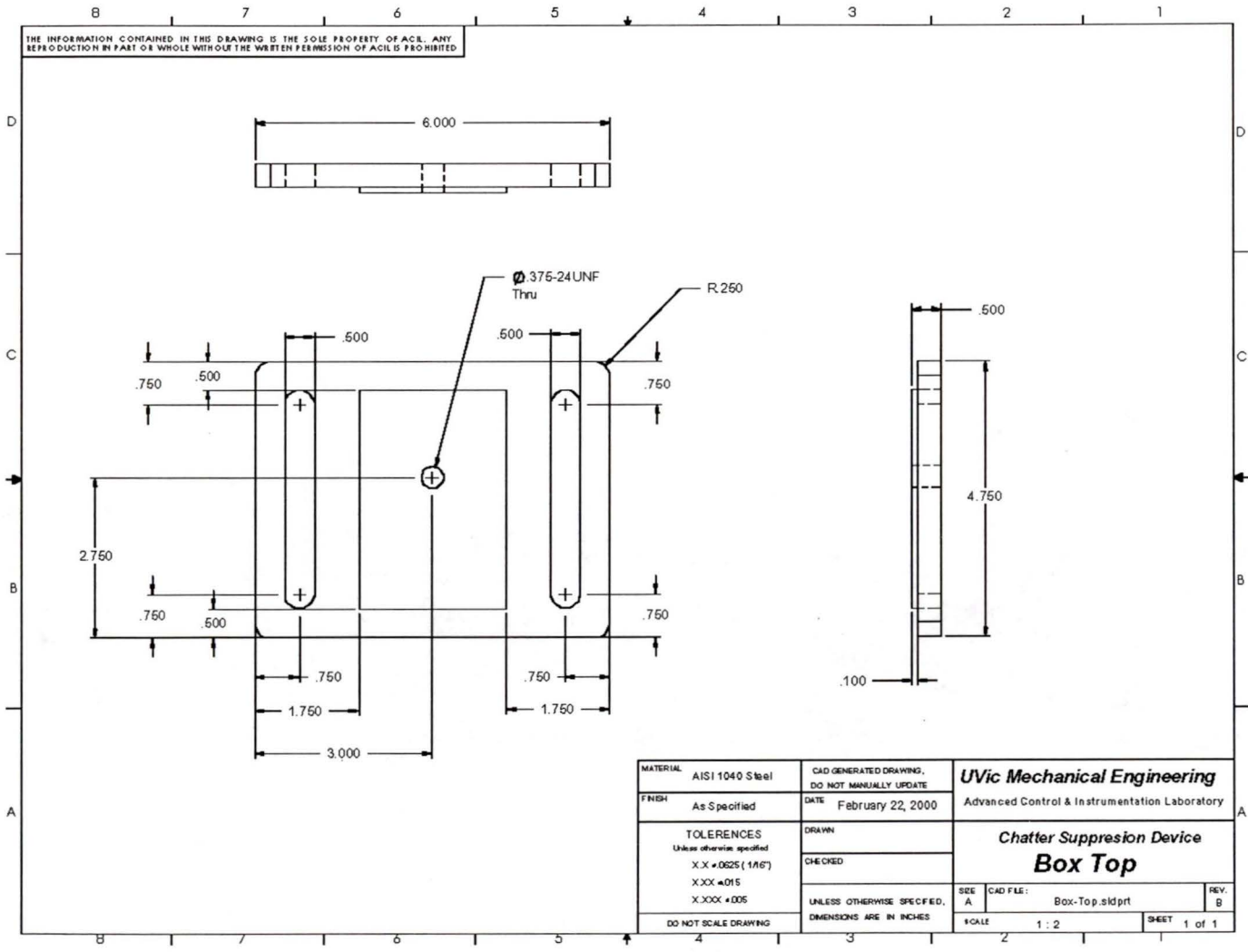
Technical Drawings of the Chatter Suppression Device

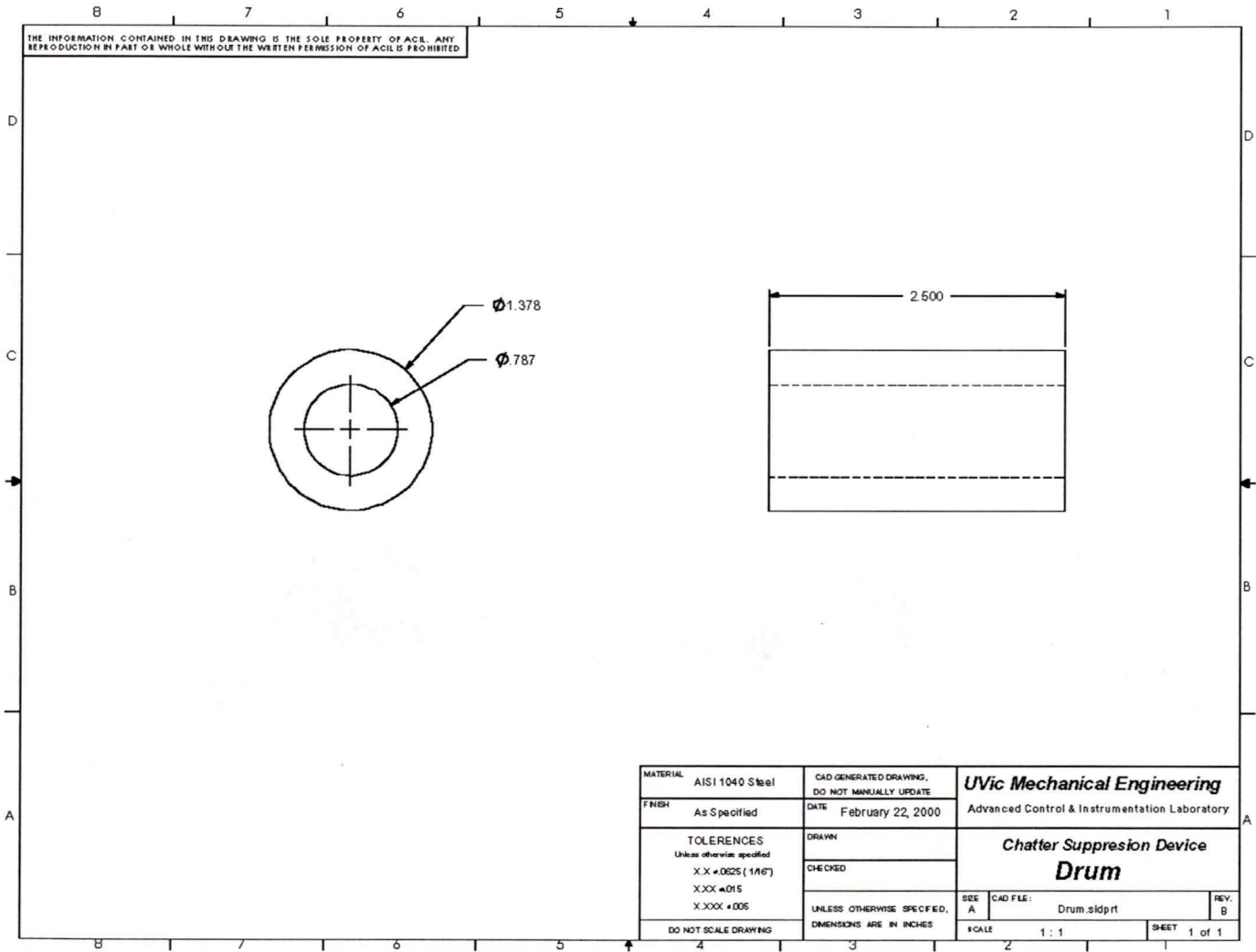


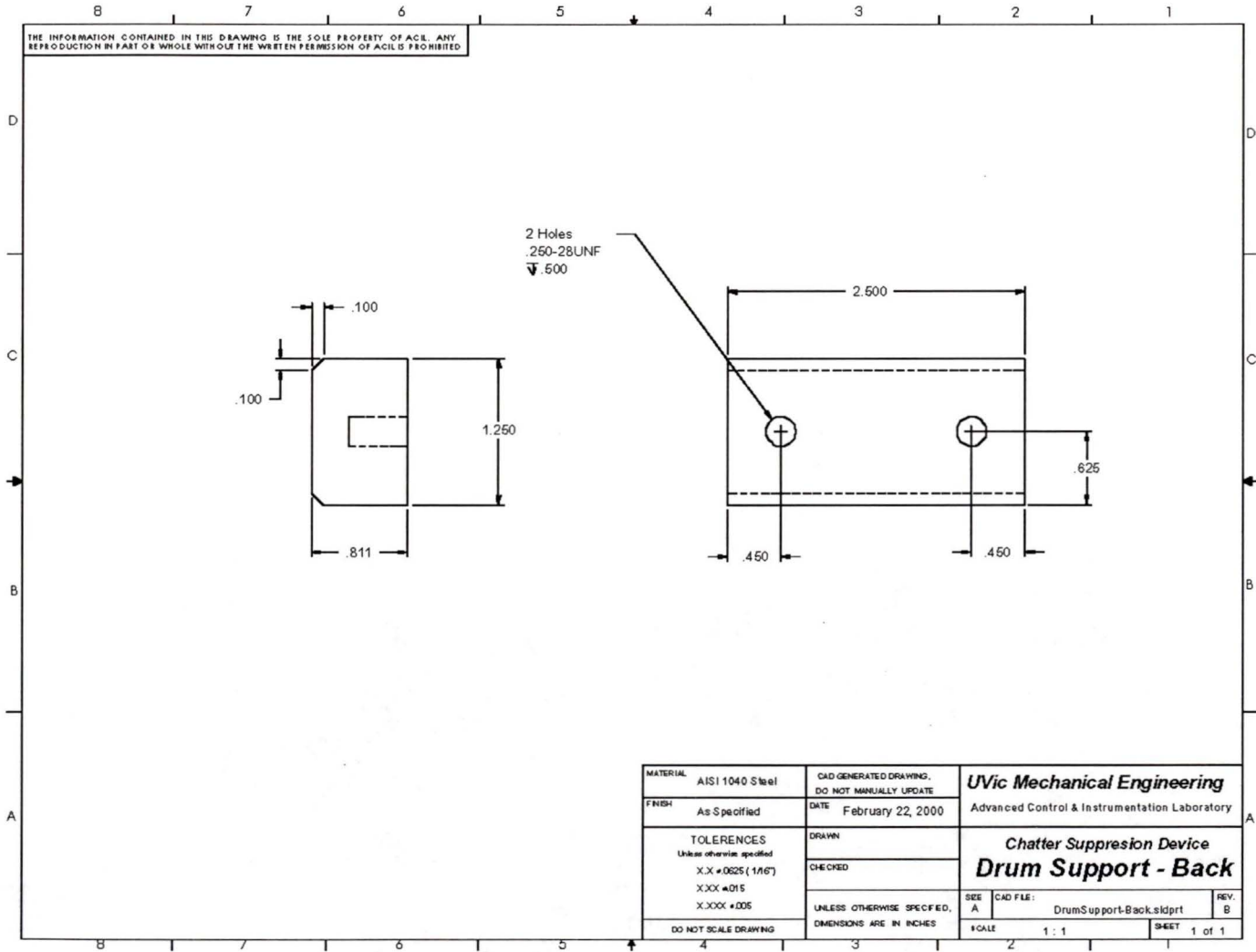


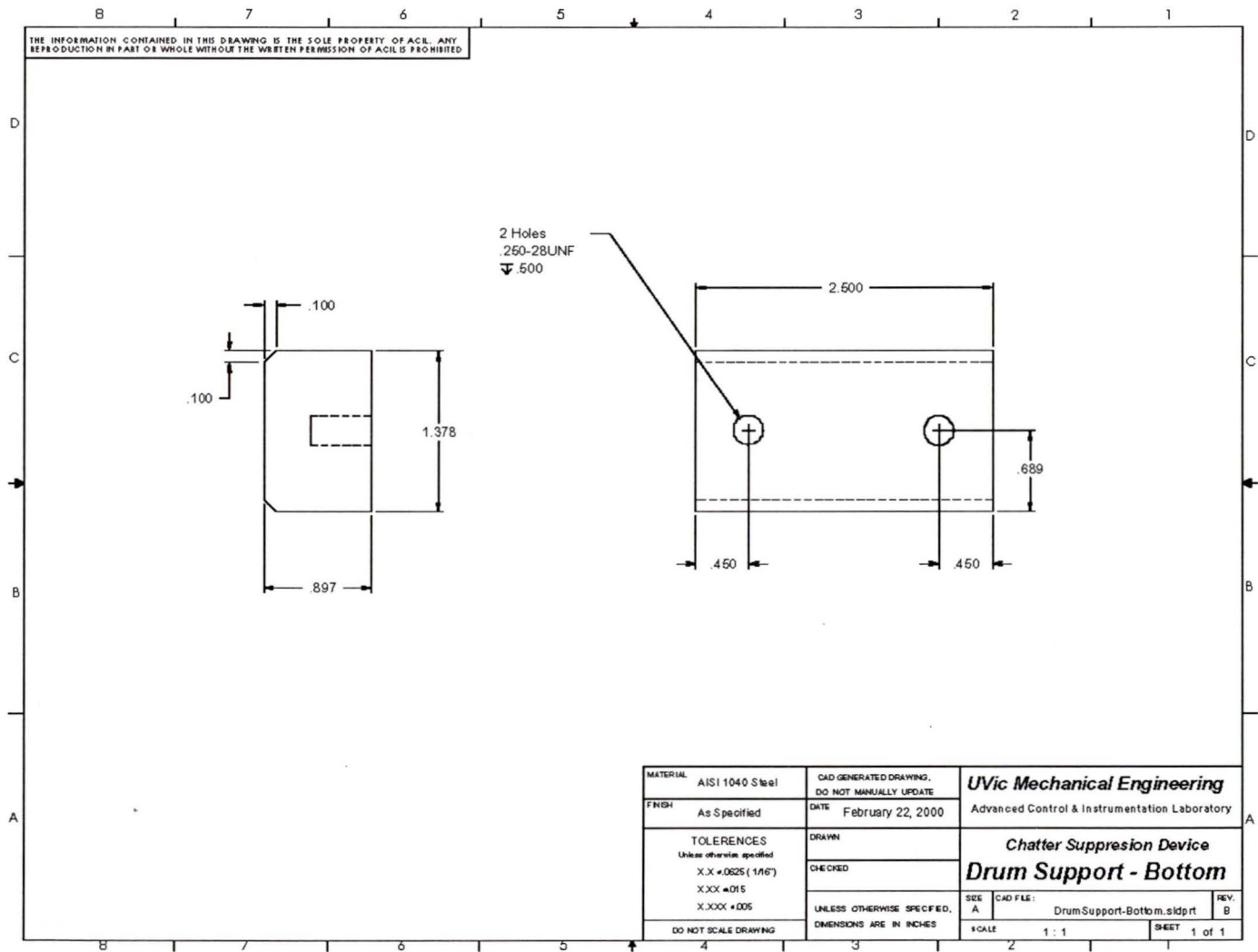


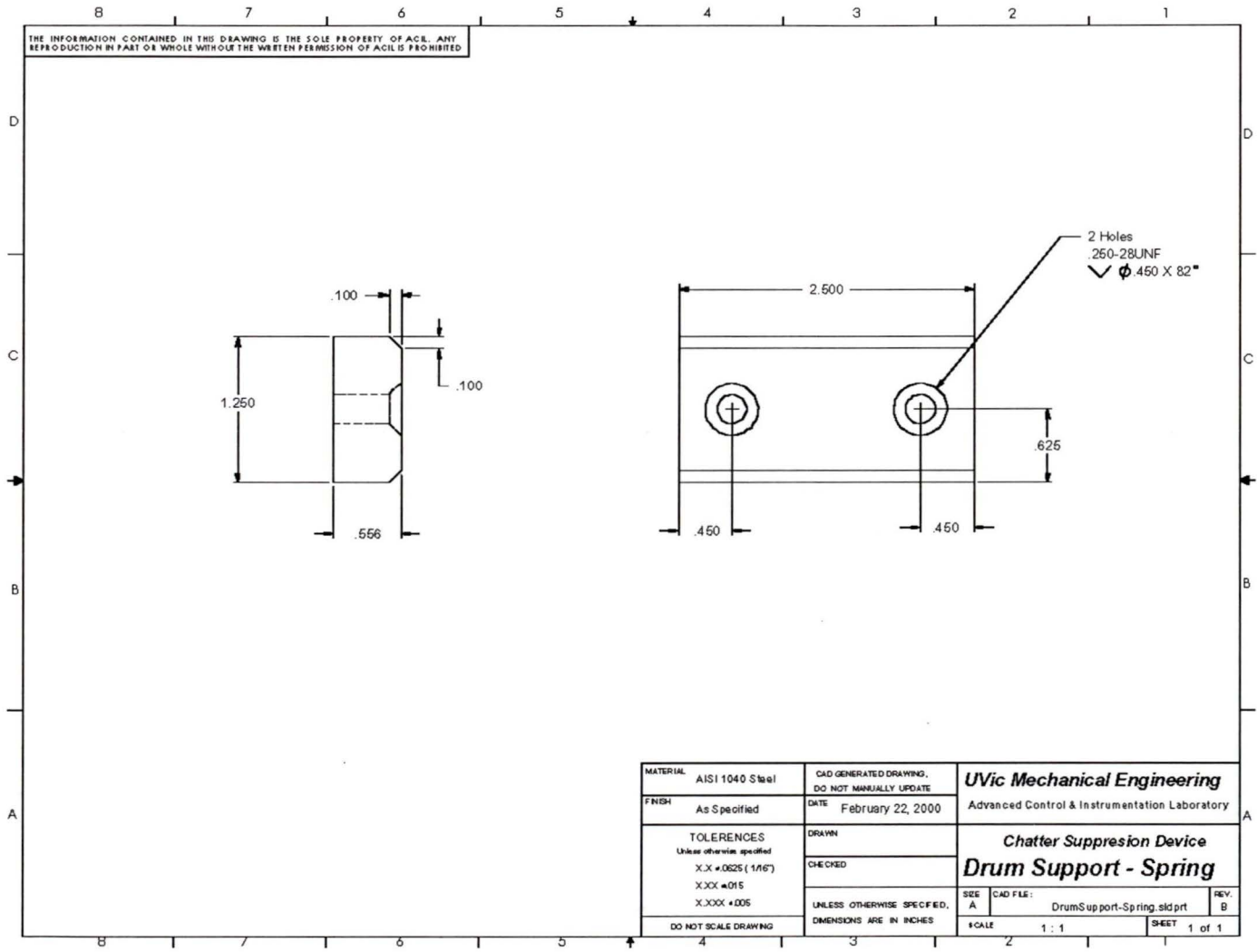


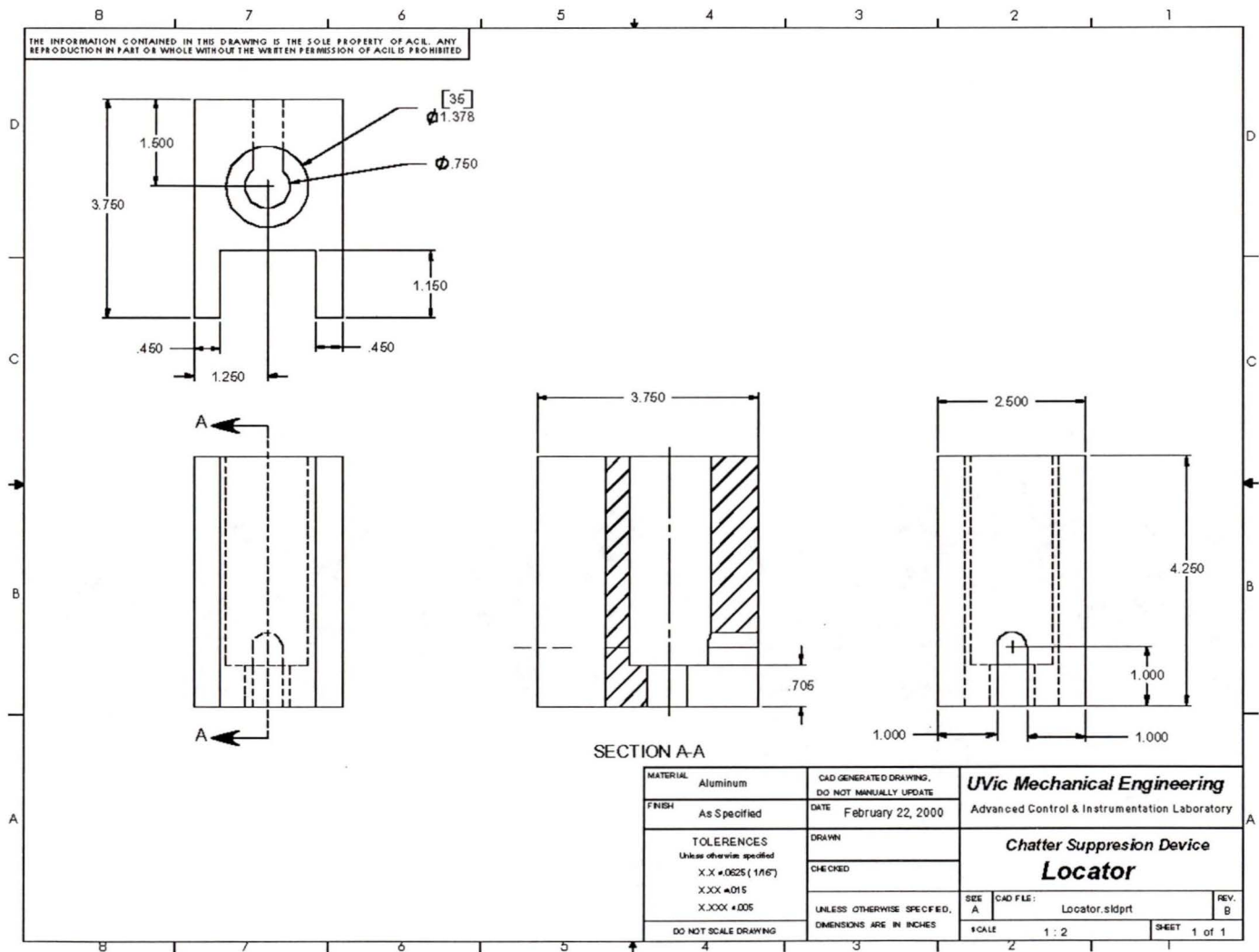


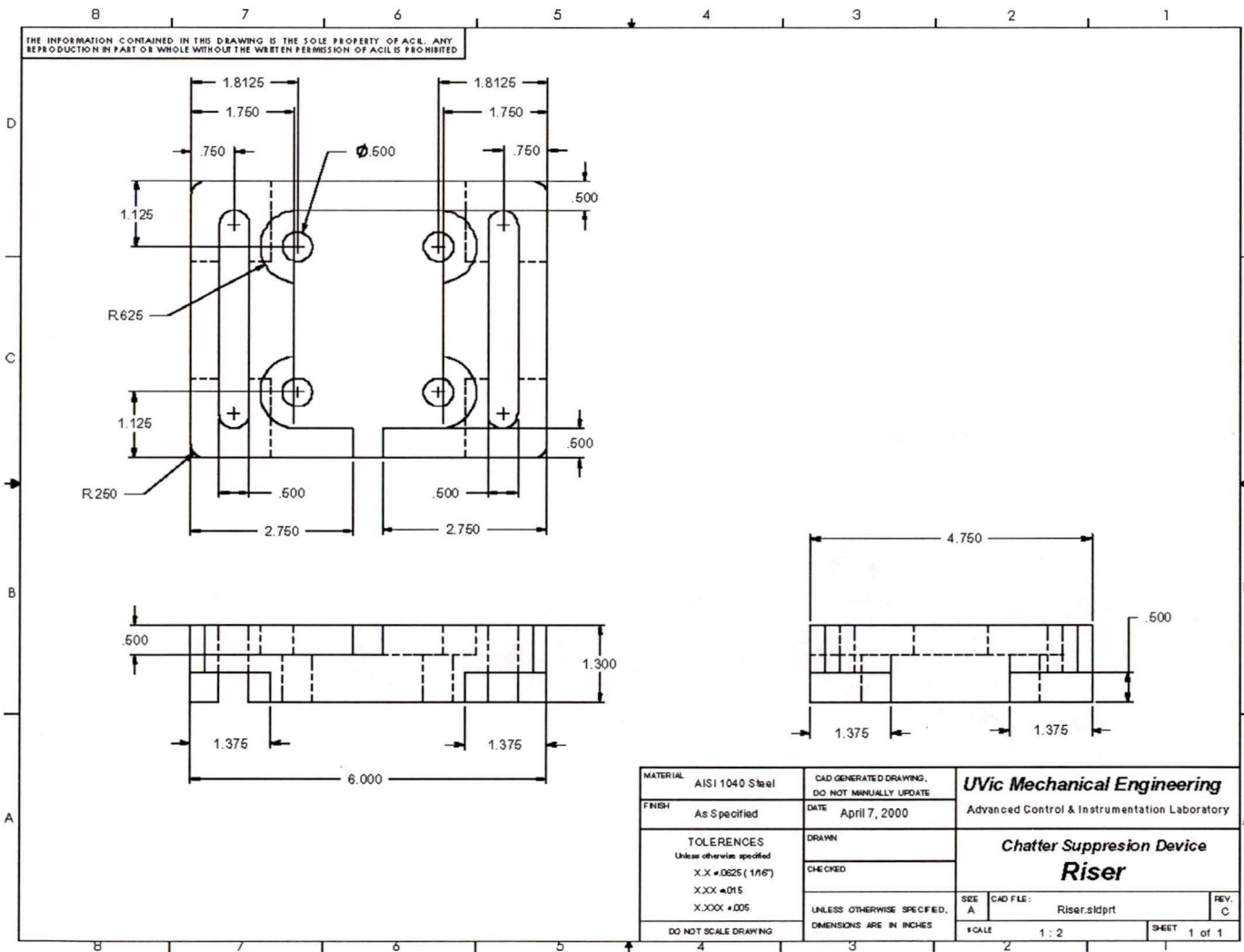


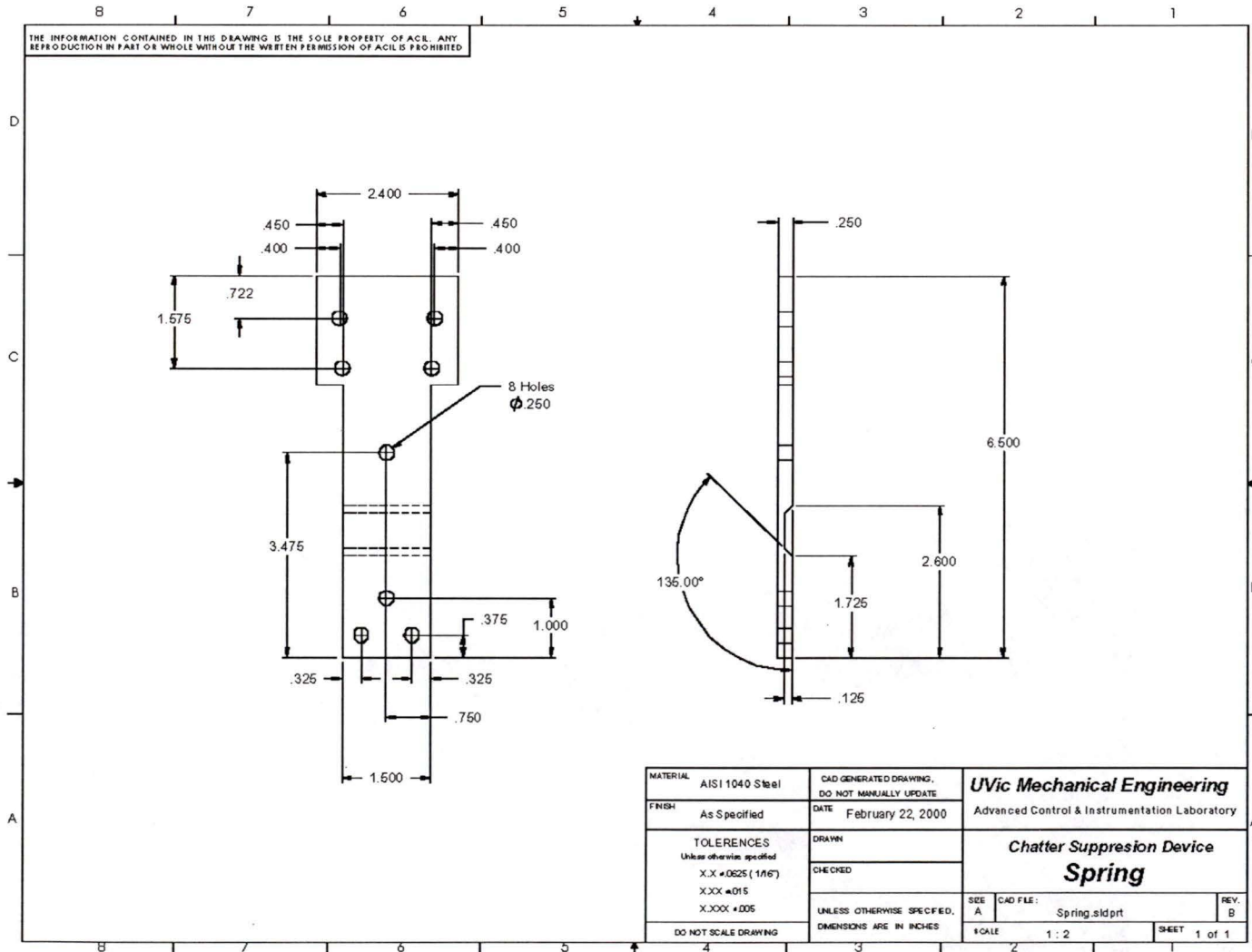


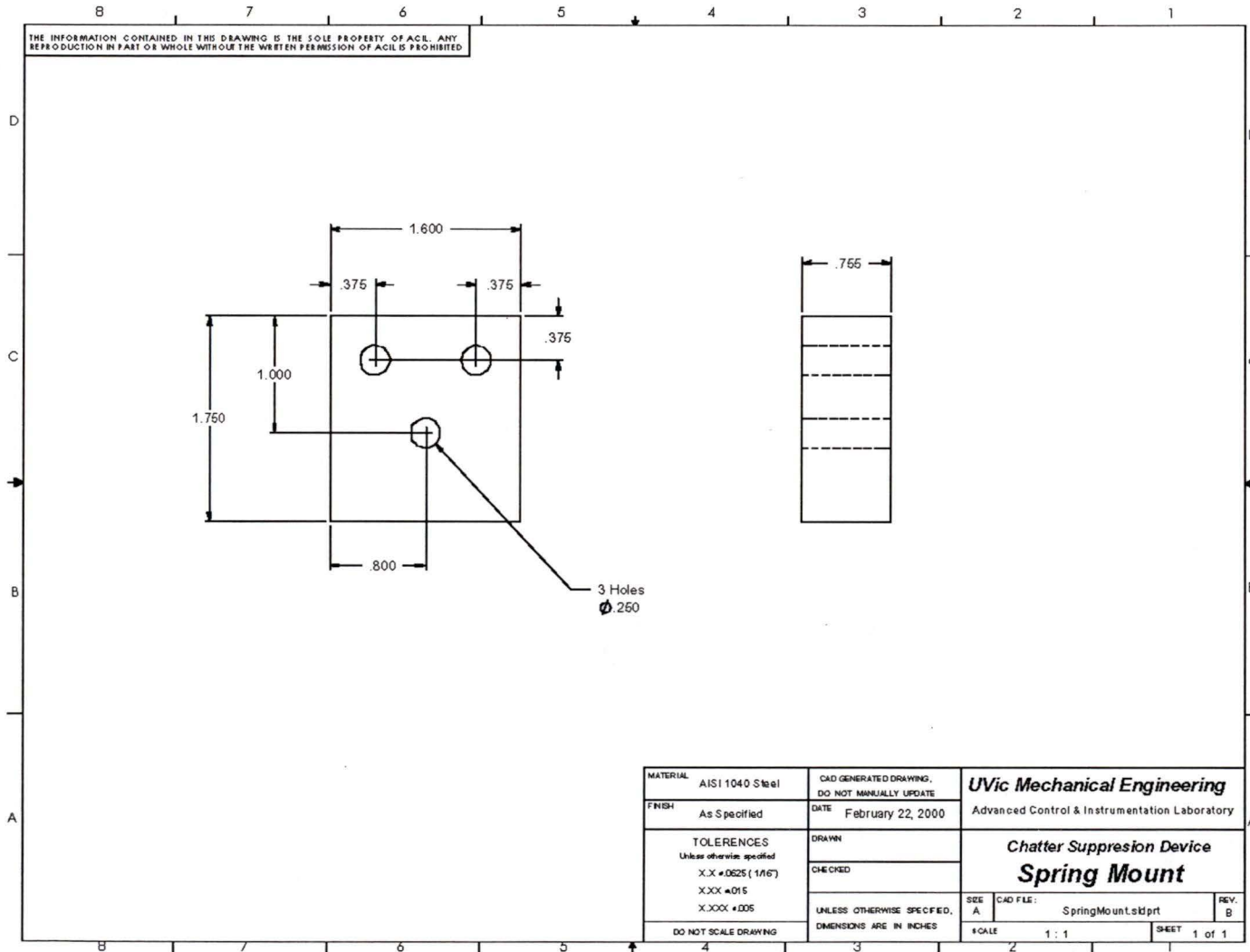


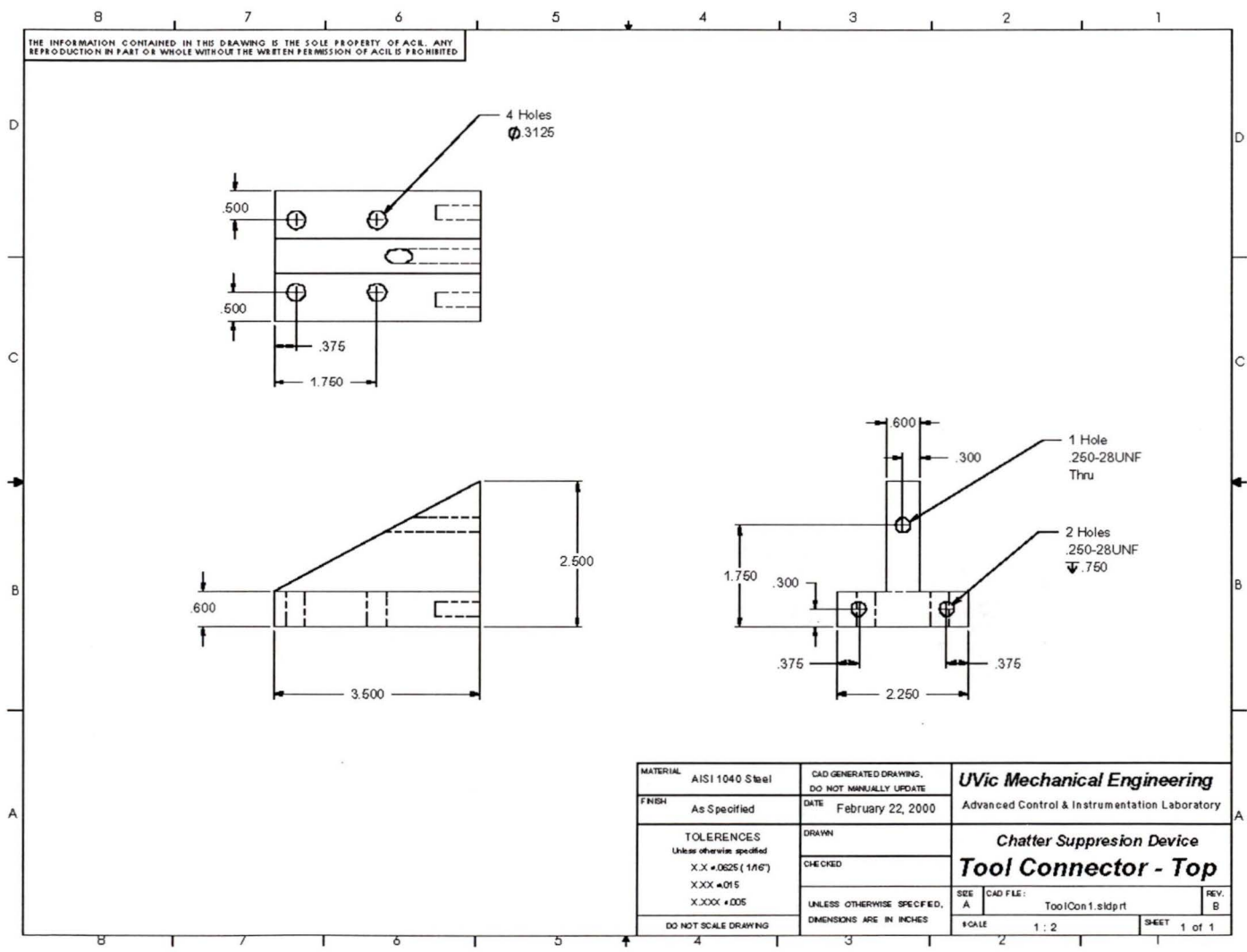


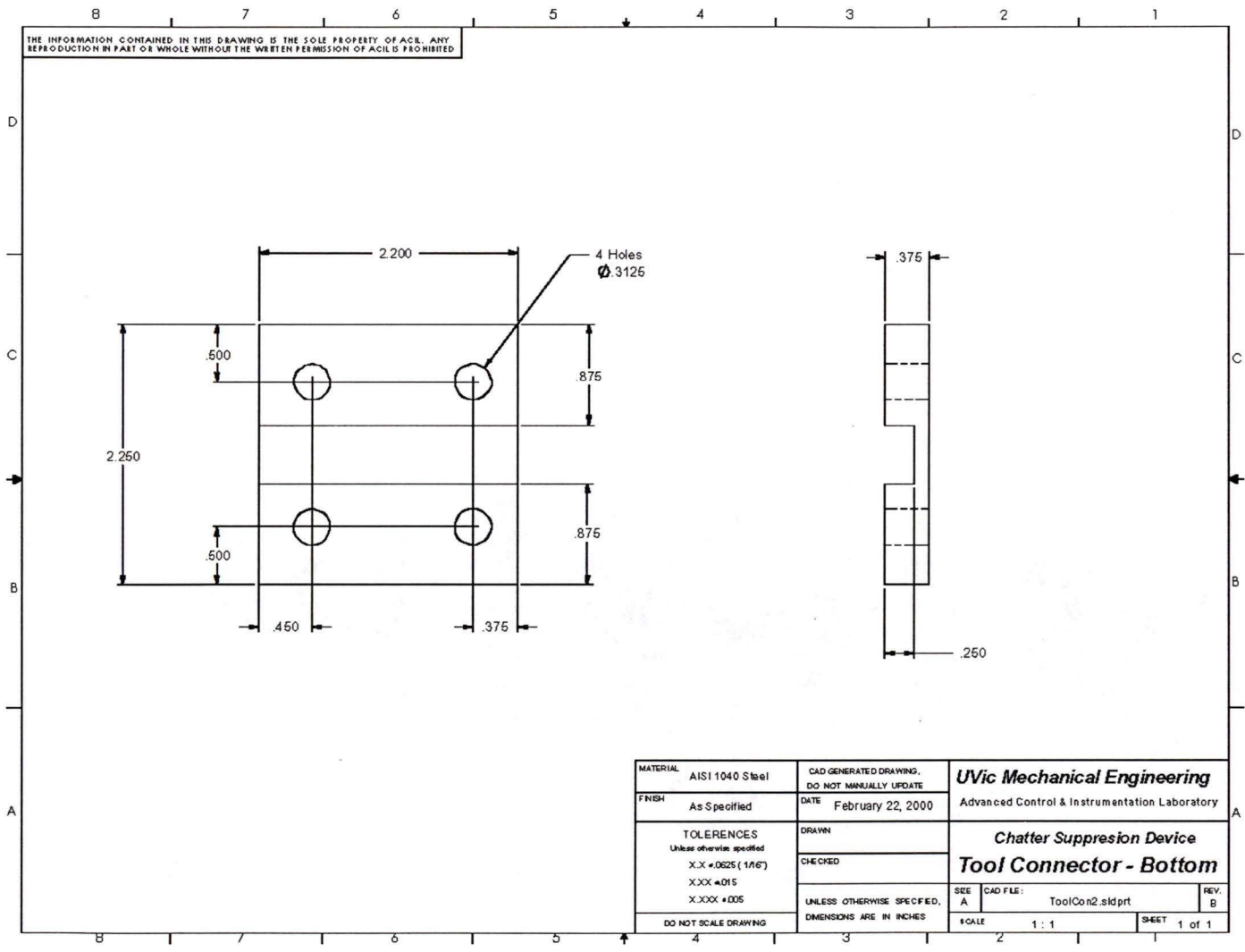












VITA

Surname: Tzonev

Given Names: Nikolay

Place of Birth: Rousse, Bulgaria

Date of Birth: April 23, 1971

Educational Institutions Attended:

University of Victoria

1992-2002

Technical University – Plovdiv

1990-1992

Degrees Awarded:

B.Eng. (Honours) University of Victoria

1997

Partial Copyright License

I hereby grant the right to lend my thesis to users of the University of Victoria Library, and to make single copies only for such users or in response to a request from the Library of any other university, or similar institution, on its behalf or for one of its users. I further agree that permission for extensive copying of this thesis for scholarly purposes may be granted by me or a member of the University designated by me. It is understood that copying or publication of this thesis for financial gain shall not be allowed without my written permission.

Title of thesis:

Design of a Piezoelectric Tool for Active Control of
Cutting Forces in Machining

Author:


Nikolay Tzonev

Date

March 20, 2002